University of Oxford

Queen's College

Department of Chemistry

Bayley Group

Development of 3D-printed droplet networks as a platform to build functional synthetic tissues

Alessandro Alcinesio

A thesis submitted for the degree of

Doctor of Philosophy

Supervisor: Hagan Bayley

Examiners: Jan C. M. van Hest

Alfonso Castrejón-Pita

Michaelmas 2019

Alessandro Alcinesio

Development of 3D-printed droplet networks as a platform to build functional synthetic tissues

DPhil Thesis, Michaelmas 2019

Supervisor: Prof. Hagan Bayley

Department of Chemistry
University of Oxford
12 Mansfield Road
Oxford OX1 3TA
United Kingdom

External Examiner:

Prof. Jan C. M. van Hest
Department of Bio-Organic Chemistry
Eindhoven University of Technology
Het Kranenveld 14
Eindhoven 5600 MB
The Netherlands

Internal Examiner:

Prof. Alfonso Castrejón-Pita
Department of Engineering Science
University of Oxford
Parks Road
Oxford OX1 3PJ
United Kingdom

Abstract

The development of synthetic multicellular systems that can mimic complex cooperative behaviour of living tissues represents a major challenge for bottom-up synthetic biology. Tissue-like systems would allow the design of devices and materials that can communicate with living tissues and monitor, control or complement their biological activity. Networks of 3D-printed aqueous droplets in oil joined by droplet interface bilayers (DIBs) represent a powerful platform from which soft-electronic devices and synthetic tissues have been developed. Precise control of droplet packing to produce constructs with predictable 3D architectures, assembly of functional constructs of dimensions relevant to biomedical applications, and transfer of functional constructs to aqueous environment will enable design of increasingly sophisticated systems. Here, we achieve highly regular droplet packing in 3D-printed synthetic tissues by controlling the equilibrium contact angle θ_{DIB} at the droplet-droplet interface. As a result, we fabricate synthetic tissues with single-droplet precision in three dimensions. We also build larger and modular synthetic tissues by assembling building blocks constructed independently. Lastly, we employ a novel strategy to transfer 3D-printed droplet networks to aqueous bulk phase, forming a functional lipid bilayer at the interface with the aqueous bulk while retaining the architecture and the functionality of the internal lipid bilayers. Using this method, we generate synthetic tissues that can communicate with their environment, as a fundamental step towards interface with living tissues in physiological conditions.

Acknowledgements

I would like to express my gratitude to all the people that contributed to my professional and personal life during my DPhil.

Firstly, my family, who through their sacrifices supported me in any step of my journey.

Prof. Hagan Bayley, whose experience and mentorship have greatly advanced my development as a scientist.
My special thanks go to Dr. Ravinash Krishna Kumar for his daily guidance and friendship, and for sharing with me the pain of staring at hexagons for months on end.

The Bayley Group, for the insightful discussions throughout the last three years. In particular, Dr. Florence Downs for the boogie sessions, İdil Cazımoğlu for the welfare teas, Sandra Ionescu for the bagels, Dr. Anne Wolfes, Dr. William Ramsey and Dr. Stuart Box for the movie nights, and the Bobs for the amazing BoBQs and our healthy obsession with Nicholas Cage. I would also like to thank Dr. Ravinash Krishna Kumar and İdil Cazımoğlu for taking the time to proofread this work and for their valuable suggestions.

The exceptional students that worked with me on some of the work in this thesis, Rebecca Allan and Gabriella Kimmerly. I hope what you could learn from me at least matches everything I learned from working with you.

Prof. Antonis Papachristodoulou, Prof. Robert Carlisle, and the Synthetic Biology Centre for Doctoral Training, for giving me the opportunity to study in this prestigious University. I would also like to thank the EPSRC, the BBSRC, the Clarendon Fund Scholarship and The Queen's College that enabled this work through their support.

Infine, vorrei ringraziare tutti i Cialtroni dall'Italia che mi accolgono sempre a braccia aperte ogni volta che torno a casa.

Sometimes, when I close my eyes,
I see hexagons...

— Dr. Ravinash Krishna Kumar

Contents

Abbreviations

αHL	α-hemolysin
DHB	Droplet hydrogel bilayer
DIB	Droplet interface bilayer
DNA	Deoxyribonucleic acid
DMSO	Dimethyl sulfoxide
DPhPC	1,2-diphytanoyl-sn-glycero-3-phosphocholine
EDTA	Ethylenediaminetetraacetic acid
φ_{SIL}	Volume fraction of silicone oil
γ_b	Surface tension of lipid bilayer
γ_m	Surface tension of lipid monolayer
GUV	Giant unilamellar vesicle
IPTG	Isopropyl β-d-1-thiogalactopyranoside
IVTT	In vitro transcription and translation
LUV	Large unilamellar vesicle
PBS	Phosphate-buffered saline
PEG	Poly(ethylene glycol)
PEGDA	Poly(ethylene glycol) diacrylate
PMMA	Poly(methyl methacrylate)
POPC	1-palmitoyl-2-oleoyl-sn-glycero-3-phosphocholine
θ_c	Critical equilibrium contact angle in a DIB
θ_{DIB}	Equilibrium contact angle in a DIB
Tris	Tris(hydroxymethyl)aminomethane
UV	Ultraviolet
x_{POPC}	Molar fraction of POPC

1

Introduction

Living tissues and organs are composed of spatially organised communities of specialised cells that interact and communicate with each other, and as a result manifest collective emergent properties.[1,2] The appearance of multicellular organisms is regarded as one of the major evolutionary transitions on Earth, which allowed the development of life forms with more sophisticated and complex capabilities compared to unicellular organisms.[2,3]

While several attempts at building single artificial cell-like systems from the bottom-up have been demonstrated,[4–7] the development of synthetic multicellular systems that can mimic the complex cooperative behaviour of living tissues still presents a major challenge in the field of bottom-up synthetic biology.[8] The development of such tissue-like systems would allow the design of devices and materials that can readily communicate with living tissues and monitor, control or complement their biological activity.

In this chapter, we outline the current achievements in the development of synthetic multicellular systems. Among these, we will particularly focus on systems composed of aqueous droplets in oil separated by droplet interface bilayers (DIBs), from which sophisticated soft-electronic devices and synthetic tissues have been successfully developed.[9]

1.1 Droplet interface bilayers

Droplet interface bilayers (DIBs) are lipid bilayer membranes that form at the interface between two lipid-stabilised aqueous droplets in oil[10] (Fig. 1.1a-b). When two aqueous droplets are dispensed in a lipid-containing oil, these amphiphilic molecules self-assemble into a monolayer at the interface between the aqueous and the oil phases. Upon contact of the two droplets, the two lipid monolayers join to form a stable bilayer that separates the two aqueous compartments ("lipid-out" method, Fig. 1.1a). Lipids can also be incorporated in the system by encapsulating vesicles and micelles within the aqueous droplets, which can burst at the water-oil interface and form a lipid monolayer ("lipid-in" method, Fig. 1.1b). The advantage of this strategy is that it allows the encapsulation of different lipid types within the two droplets forming a DIB, resulting in the formation of asymmetric bilayers.[11]

Early work on DIBs was driven by efforts towards miniaturisation of lipid bilayer systems to perform single-molecule electrical recordings using protein nanopores: once electrodes were inserted into each droplet, a single-channel ionic current flowing through a protein pore (e.g. α-hemolysin, αHL) inserted within the interface bilayer could be recorded[10] (Fig. 1.1c-d). Compared to conventional planar lipid bilayers, the DIB setup presents several advantages, such as robustness against hydrostatic pressure and mechanical stress, flexibility in the composition of the two leaflets of the lipid bilayer, ability to modulate the bilayer area over time, and importantly the use of greatly reduced quantities of expensive reagents and proteins.[12] In the last decade, DIBs have been used to investigate a wide variety of membrane proteins, such as porins, channels and transporters.[9]

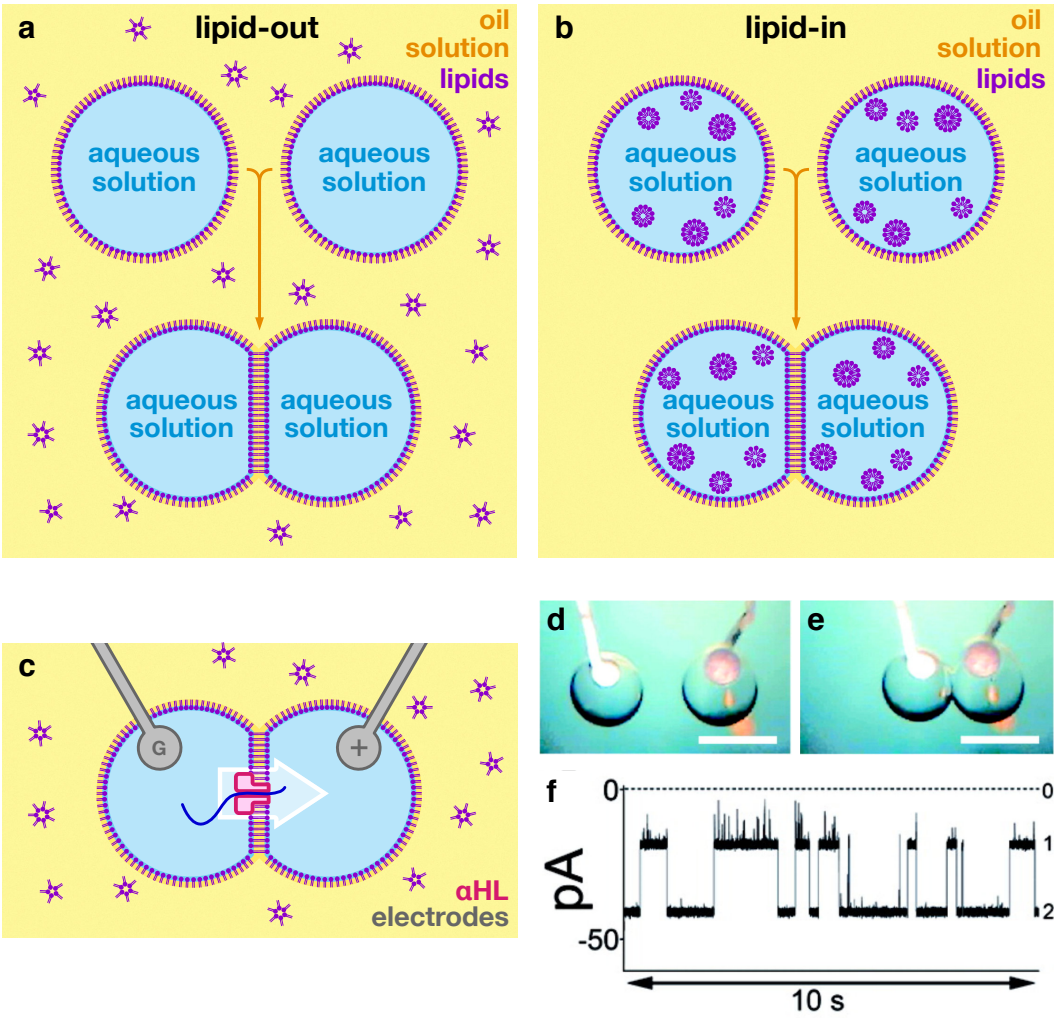

Fig. 1.1. Droplet interface bilayers. **a-b**, Formation of droplet interface bilayer (DIB) between a pair of droplets using the "lipid-out" (**a**) or "lipid-in" (**b**) methods. In the "lipid-out" method, a monolayer of lipids self-assembles at the interface of aqueous droplets formed in a lipid-containing oil (**a**). In the "lipid-in" method, the lipid monolayer is formed by fusion at the water-oil interface of lipid vesicles and micelles encapsulated within the water droplets (**b**). In both cases, when droplets are brought into contact with each other, a kinetically stable lipid bilayer forms at the interface between the two aqueous droplets. **c**, Diagram of single-channel electrical recording using protein nanopores inserted in DIBs. **d-f**, Pictures of a pair of droplets before (**d**) and after (**e**) formation of a interface bilayer, and current trace of an analyte (γ-cyclodextrin, γCD) reversibly binding to a single protein pore[10] (α-hemolysin, αHL). Scale bars: $700\,\mu$m.

1.2 Droplet interface bilayer networks

Among the interesting possibilities enabled by DIBs is the ability to assemble networks of multiple droplets interfaced by lipid bilayers in specific architectures in two and three dimensions.[9] In droplet networks, the composition of

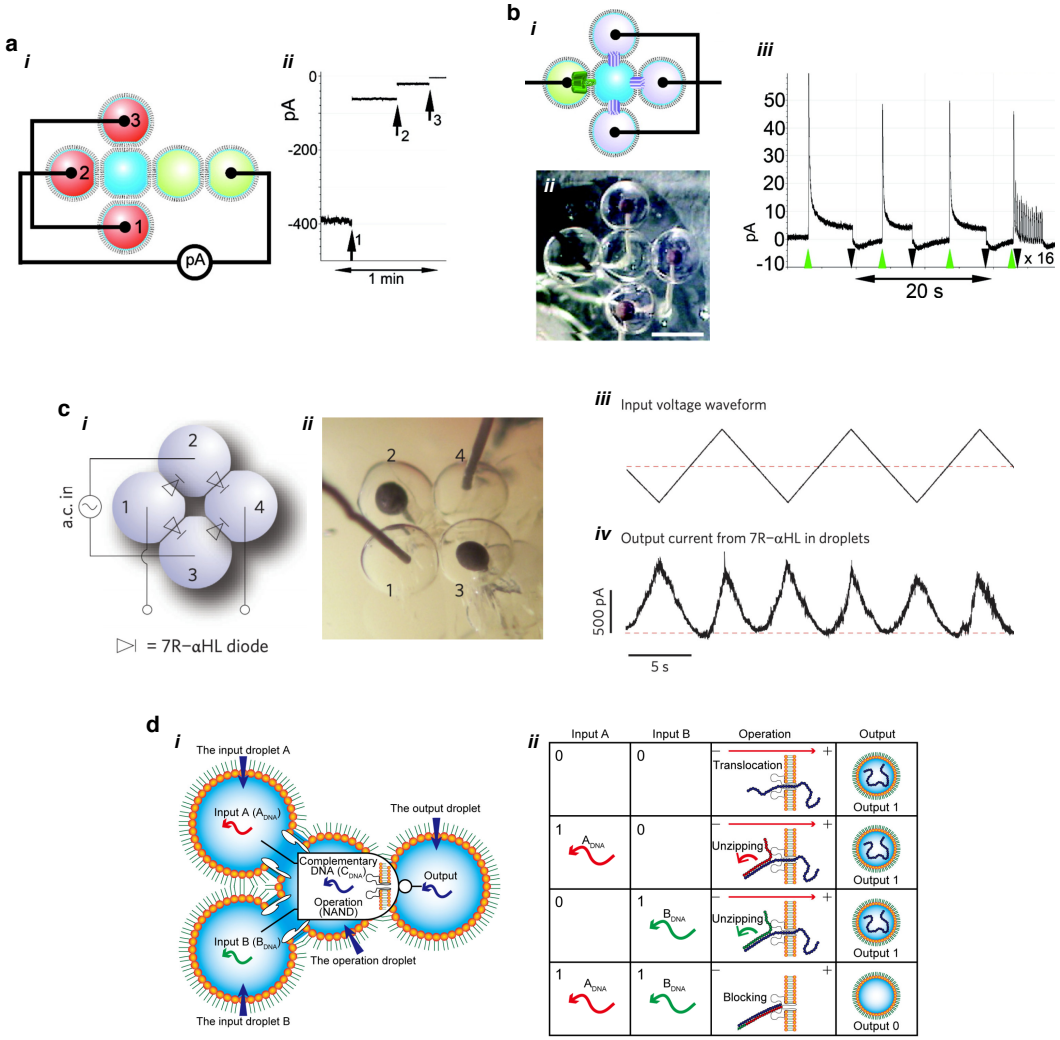

Fig. 1.2. Soft-electronic devices made from small droplet networks. **a**, DIB-based bio-battery.[10] Voltage is generated by joining droplets at low salt concentration (100 mM NaCl) containing the anion selective mutant N123R αHL (red droplets), and droplets at high salt concentration (1 M NaCl), containing wild-type αHL (green droplets) (*i*). A drop in ionic current is observed when each of the three red droplets are removed from the network (*ii*). **b**, DIB-based light detector[10] obtained by incorporating the light-driven proton pump bacteriorhodopsin (bR) in a small droplet network (*i*). Upon illumination with green light, an ionic current is generated (*ii*). Scale bar: 700 μm. **c**, A full-wave rectifier obtained by joining four droplets containing the 7R αHL mutant, which operates like a diode.[13] **d**, A NAND logic gate implemented in a droplet network[14] composed of two "input" droplets (encapsulating short single-stranded DNA molecules as input signals), an "operation" droplet (containing the complementary ssDNA strand for both the input strands), and an "output" droplet. When both input single strands are present, they will hybridise with the complementary strand in the "operation" droplet, forming a double-stranded DNA (dsDNA) that can not translocate to the output droplet.

each component can be changed to achieve collective properties that are not achievable by a simple droplet pair. By assembling simple architectures of droplets and by using a range of membrane proteins, several soft-electronic

devices have been demonstrated, such as bio-batteries[10] (Fig. 1.2a), light sensors[10] (Fig. 1.2b), rectifiers[13] (Fig. 1.2c) and logic gates[14] (Fig. 1.2d).

Of increasing interest is the use of droplet networks as micro-reactors to encapsulate series of reactions in separate compartments, while allowing the controlled flow of substrates and products through the interfacial bilayers and protein pores. Simple chemical reactions have been encapsulated within droplet pairs and chains, such as the oxidation of amplex red to resorufin, catalysed by the enzyme horseradish peroxidase (HRP) in the presence of hydrogen peroxide (H_2O_2),[15,16] (Fig. 1.3a). The oscillating Belousov–Zhabotinsky (BZ) reaction (Fig. 1.3b*i*) has also been shown in single droplets and in droplet chains[17,18] (Fig. 1.3b*ii-iv*). In order to generate increasingly responsive and "life-like" systems, genetic constructs and *in-vitro* transcription and translation (IVTT) systems can be incorporated in DIBs[19,20] (Fig. 1.3c) Using this strategy, it is possible to produce and record the activity of proteins,[19] as well as control transcription and translation with external triggers.[20]

1.3 Fabrication of droplet networks

As discussed in section 1.2, interesting properties can emerge by arranging clusters of droplets of different composition in specific architectures (Fig. 1.2). In order to explore increasingly complex functionalities of large assemblies of droplets, it is crucial to develop strategies to efficiently generate defined geometries of droplet clusters with controlled patterning of each droplet type.

In early work involving DIB pairs and networks, nanolitre-sized droplets were usually dispensed individually using a standard micro-pipette and manipulated manually using pipette tips or manual micro-manipulators,

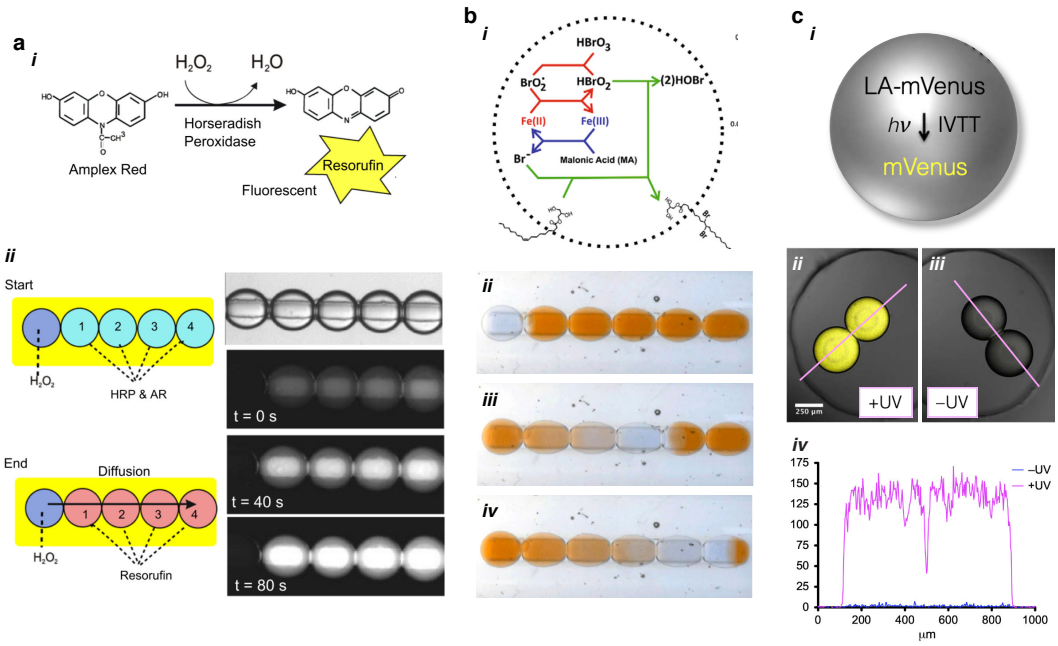

Fig. 1.3. Chemical and biochemical reactions in droplet networks. **a**, The oxidation of amplex red to resorufin catalysed by the enzyme horseradish peroxidase (HRP) in the presence of H_2O_2 (*i*). This reaction was performed in droplet chains by encapsulating H_2O_2 in one of the droplets, which spontaneously diffused to the remaining droplets in the chain, allowing the enzyme to catalyse the formation of the fluorescent compound resorufin[15,16] (*ii*). **b**, The oscillating Belousov–Zhabotinsky (BZ) reaction (*i*) was shown to travel through DIBs in a droplet chain, likely due to the permeability of the inhibitory and excitatory components of the reaction through lipid bilayers[17,18] (*ii*). **c**, Encapsulation of *in-vitro* transcription and translation (IVTT) systems inside droplets (*i*) allowed production of functional proteins *in-situ*[19] in response to external stimulation with UV light[20] (*ii-iv*).

when electrodes were inserted within them. Although low-throughput, this strategy still allows the reproducible construction of simple droplet networks, and highlights how DIBs and droplet networks allow for the fabrication of powerful and sensitive soft devices with minimal laboratory equipment.[10] The manual assembly of DIB networks can also be facilitated by using patterned surfaces and containers that can spatially confine the relative movement of droplets with respect to each other.[10,21,22]

Microfluidic systems have been widely used to generate large number of droplets and arrange them in small clusters.[23,27–29] While the number and speed of droplet generation by microfluidics is usually very high, the architectures achievable are usually limited to chains of droplets in 1D (Fig. 1.4a*i*), 2D (Fig. 1.4a*ii*), and 3D with only two droplet layers in the z direction[23]

(Fig. 1.4a*iii-iv*). Single-channel electrical recordings[30] and simple chemical reactions[16] have been demonstrated in microfluidically generated DIB systems.

Magnetic handling was also applied to the manipulation of droplets and assembly of three dimensional networks. Wauer and colleagues demonstrated that it is possible to encapsulate paramagnetic beads within droplets, which can consequently be moved within the oil bath using a magnetic probe[24] (Fig. 1.4b). Droplets that do not contain paramagnetic beads can be manipulated by formation of a temporary DIB with a "carrier" droplet containing the beads

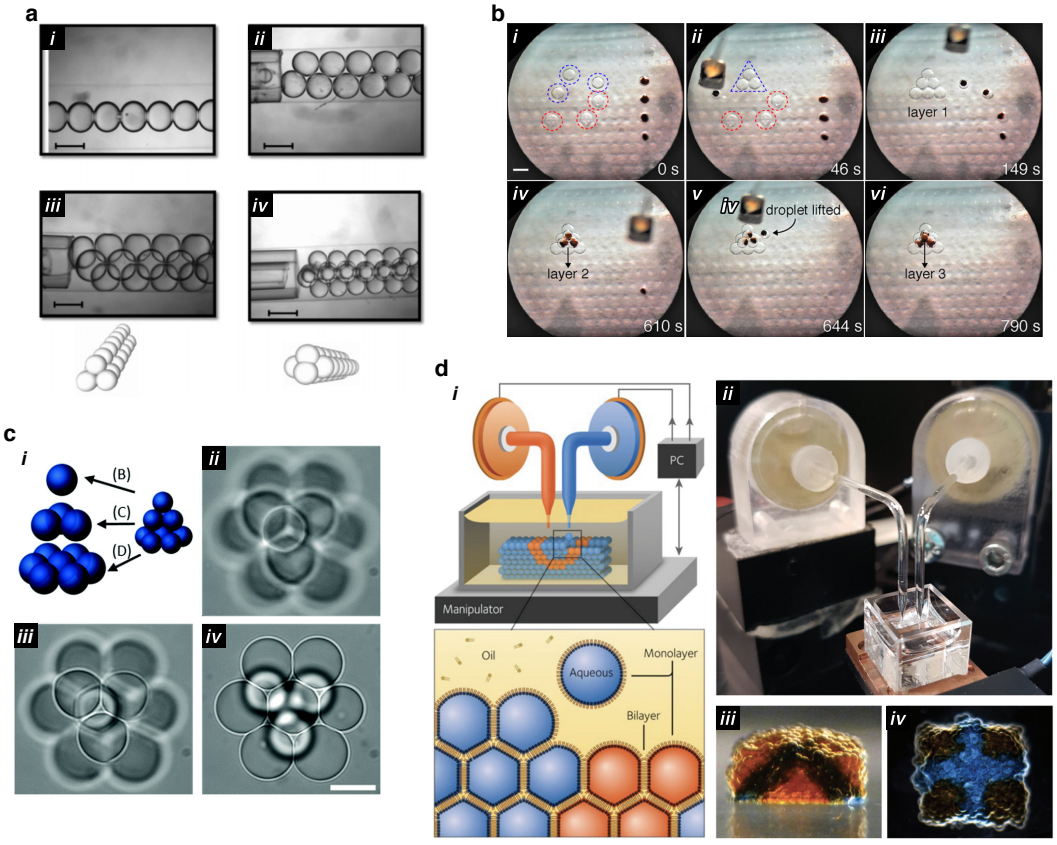

Fig. 1.4. Fabrication of droplet networks. **a**, Formation of 1D (*i*), 2D (*ii*) and 3D (*iii-iv*) droplet chains by microfluidics.[23] Scale bar: $400\,\mu\mathrm{m}$. **b**, Assembly of droplet networks through magnetic handling.[24] Droplets containing paramagnetic beads can be manipulated and positioned using a magnetic probe, and also used as "carriers" to manipulate droplets that do not contain beads (*i-iii*). **c**, Small droplet networks assembled using a single laser-beam optical trap.[25] **d**, Schematic (*i*) and picture (*ii*) of the droplet-based 3D-printer.[26] This system allows patterning of hundreds to thousands of picolitre-sized aqueous droplets by the synchronised motion of a motorised micro-manipulator and the piezo-ejection of droplets at the nozzle tips (*iii-iv*).

(Fig. 1.4b*i-iii*). With this method, 3D networks of up to nine droplets in three stacked layers were assembled. Similarly, optical tweezers have also been used to manipulate small droplets ($\simeq 14\,\mathrm{pL}$) and assemble them in small 3D DIB networks[25] (Fig. 1.4c).

1.3.1 The droplet-based 3D-printer

The droplet-based 3D-printer developed in the Bayley Group currently represents the most advanced system that allows the generation of 3D networks of hundreds to thousands of picolitre-sized aqueous droplets in oil with defined patterns[26] (Fig. 1.4d).

In our setup, aqueous droplets (typically $50-120\,\mu\mathrm{m}$ in diameter, corresponding to $65-900\ \mathrm{pL}$ in volume) are ejected on-demand at the tip of a glass nozzle by controlled generation of mechanical pressure waves imposed by a piezo-electric actuator (Fig. 1.4d*i-ii*). Patterning of droplets is achieved by the synchronised motion of a motorised micro-manipulator with the ejection of droplets at the nozzle tip. The current setup allows the simultaneous patterning of two aqueous solutions from two printing nozzles, however it is possible to generate networks composed of more than two types of aqueous droplets by sequentially washing and re-loading the subsequent aqueous "inks" within the nozzles. Droplet networks of hundreds to thousands of compartments can be automatically generated droplet-by-droplet, line-by-line, and layer-by-layer at a droplet ejection frequency of typically $0.5-2\ \mathrm{s}^{-1}$, according to a user-generated printing map.

The droplet-based 3D-printer is also able to print a range of different aqueous solutions, from simple buffer solutions,[26] to aqueous inks at high protein concentration[20] (IVTT mix), to hydrogels and cell-laden bio-inks.[31] Droplet

networks fabricated by 3D-printing also represent a versatile platform from which synthetic tissues are generated (see section 1.5).

1.4 Interfacing droplet networks with an aqueous environment

As discussed above, droplet networks represent a versatile and robust platform to build soft devices (Fig. 1.2), compartmentalise chemical and biochemical reactions (Fig. 1.3), and form compartmentalised tissue-like materials (Fig. 1.4d). One of the long-term goals in designing increasingly complex droplet networks is the development of soft biomedical devices that can be interfaced and interact with biological tissues.[9] However, DIB pairs and networks are formed within an oil environment, which severely limits their applicability in biologically relevant scenarios.

Several strategies have been developed to form droplet networks that can function in an aqueous environment. An early attempt towards this goal is the development of multisomes, which consist of aqueous droplet networks formed within a larger droplet of oil, which is immersed within a bulk aqueous phase[32] (Fig. 1.5a). In this system, the droplets forming the encapsulated droplet networks are separated both from each other and from the external aqueous bulk phase by a lipid bilayer. Consequently, movement of ions and molecules among the internal compartments and with the environment can be controlled by the insertion of protein pores within the lipid membranes. Controlled bursting of the internal compartments triggered by a change in pH or temperature in the external solution also allows the release of droplet content into the aqueous bulk.[32]

Multisomes can be manually assembled by dispensing nanolitre-sized aqueous droplets within an oil drop containing lipids, which is suspended on a silver-wire loop within an aqueous bath (Fig. 1.5a). Picolitre-sized aqueous droplets can be printed within multisomes using the droplet-based 3D-printer

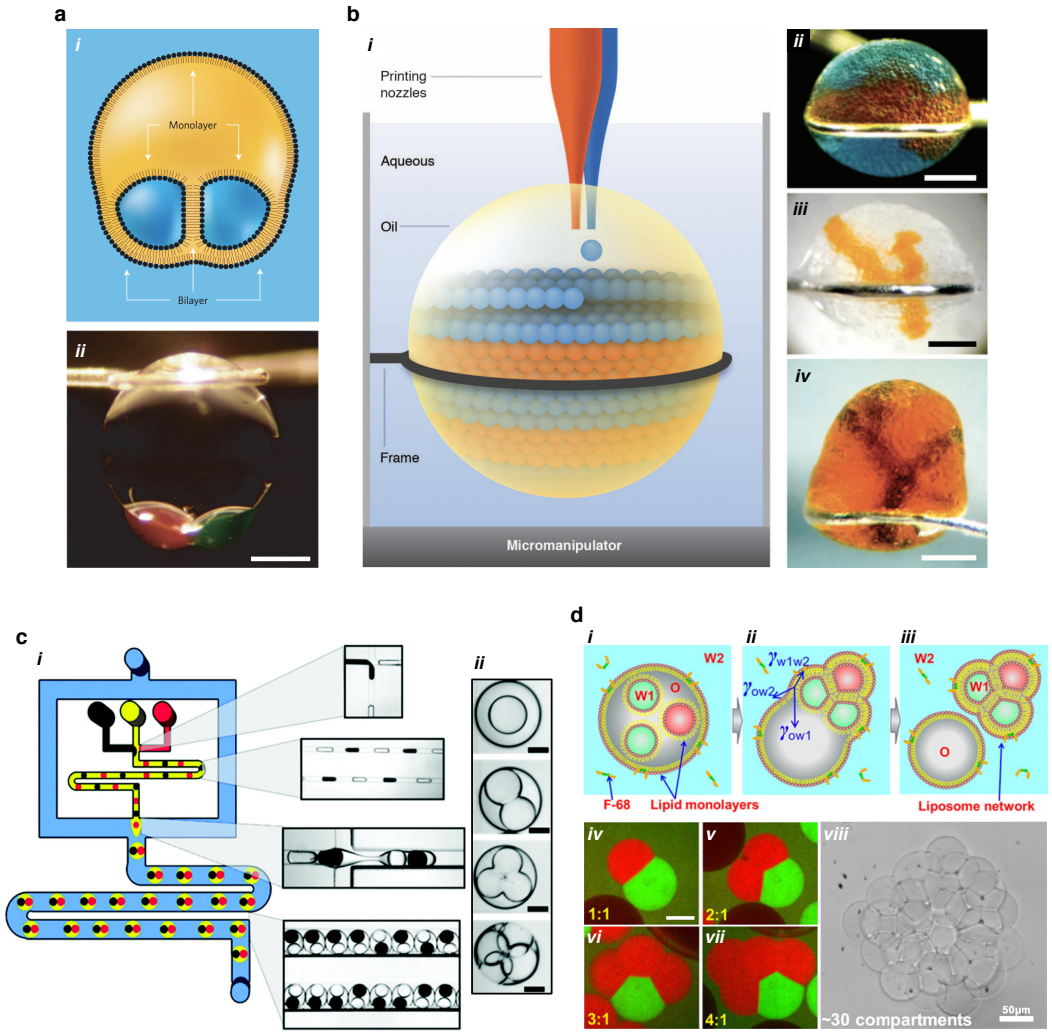

Fig. 1.5. Multisomes and multi-compartment liposomes. **a**, Diagram (*i*) and picture (*ii*) of a multisome composed of two aqueous droplets formed within a larger droplet of oil, which is immersed within a bulk aqueous phase.[32] **b**, Diagram (*i*) and pictures (*ii-iv*) of 3D-printed multisomes. Using this strategy, 3D patterns of picolitre-sized droplets were generated. However, these structures were bound to a supporting silver wire that holds the oil droplet within the aqueous bulk phase.[26] **c**, Diagram (*i*) and pictures (*i-ii*) of microfluidically-generated multisomes composed of up to four compartments. These constructs suffered from high instability, with an average lifetime of only 1 h.[33] **d**, Diagram (*i-iii*) and pictures (*iv-viii*) of multi-compartment liposomes produced by microfluidics. These were obtained from microfluidically-generated multisomes, from which the oil was removed (dewetting) by controlling the surface energies in the system.[34] Non-patterned structures of up to 30 compartments were generated using this method (*viii*). Scale bars: $400\,\mu$m (**a-b**), $50\,\mu$m (**c-d**).

described earlier (see section 1.3.1). Using this strategy, 3D patterns of droplets have been demonstrated.[26] (Fig. 1.5b) However, these structures were bound to the supporting silver wire, and no functionality has been demonstrated within them so far.

Multisomes have also been generated by microfluidics[33] (Fig. 1.5c). Using this method, up to four nanolitre-sized droplets were encapsulated within an oil droplet, which was free to float within a bulk aqueous environment. However, multisomes generated by microfluidics suffered from high instability, with an average lifetime of only $1\,\mathrm{h}$.[33] To improve their stability and longevity, multisomes have also been encapsulated within hydrogel shells[35] or blocks,[36] allowing them to be stable for days. However, in all cases of microfluidically-generated multisomes, the number of droplet types and the ability to precisely arrange their spatial positioning is limited.

Similarly to multisomes, multi-compartment liposomes are structures composed of various compartments separated from one another as well as from the external aqueous phase by lipid bilayers. In this system however, there is no oil phase encapsulating the structure (Fig. 1.5d*iii*). In early attempts, multi-compartment liposomes with up to six compartments have been obtained by transferring droplet networks through an oil-water interface under gravity, in the presence of lipids.[37] However, these structures were affected by low yield and short life-time, due to osmotic stress: in order to provide enough weight to overcome the tension of the oil-water interface, large quantities of sucrose ($0.5 - 1.75\,\mathrm{M}$) were encapsulated within the droplets, resulting in osmotic stress that would eventually rupture the constructs. Despite these issues, a range of functionalities have been demonstrated in multi-compartment liposomes produced using this method, such as bilayer permeabilisation and transport of molecules,[37] a series of reactions in a compartmentalised enzymatic pathway,[38] and translation of proteins through encapsulation of a cell-free expression system.[39]

More recently, multi-compartment liposomes have also been produced by microfluidics.[34] During this process, multisomes are first generated through a microfluidics-based approach. By controlling the interfacial energies in the system it was possible to drive the spontaneous dewetting of the oil phase from the surface of the droplet network. Specifically, this was achieved by the addition of a block copolymer surfactant (Pluronic F68) to the outer aqueous phase, which lowered the surface energy of the outer leaflet of the external lipid bilayer, allowing for the detachment of the oil from the surface (Fig. 1.5d*i-iii*). Using this method, multi-compartment liposomes composed of up to 30 identical compartments were generated[34] (Fig. 1.5d*viii*). However, control over the spatial positioning of each compartment with respect to each other was not achieved.

1.5 Synthetic tissues

Droplet networks are a powerful and versatile platform to build artificial multi-compartment systems in which collective properties can emerge from the interaction of hundreds of compartments with different functionalities. While several strategies to design synthetic cells from the bottom-up have been proposed and tested with promising results,[4–7] the engineering of synthetic multi-cellularity remains a largely unexplored field.[8]

In recent years, synthetic cell research has demonstrated the ability to recapitulate key "life-like" features within synthetic cell-like structures such as liposomes,[40] polymersomes[41] and coacervate droplets.[42] Several functions have been incorporated in these systems, including compartmentalisation of molecules and reactions,[41] DNA replication,[43] *in-vitro* transcription and translation of proteins,[44,45] division[46] and chemical communication.[47–49] More sophisticated synthetic cell designs, containing synthetic organelles obtained by encapsulation of vesicles[50] and coacervate droplets,[51,52] have

been demonstrated. Early attempts in the design of synthetic multi-cellular systems focused on consortia of synthetic cells[53,54] dispersed in solution and on the formation of multi-compartment tissue-like structures.[34,55] Among these, 3D-printed networks of droplets interfaced by lipid bilayers represent the most advanced technology to form tissue-like systems with defined architecture.[20,26]

To date, shared terminology in this field is still in development, and a clear classification in the spectrum of systems that range from compartmentalised tissue-like materials to multi-cellular "life-like" systems is still under debate. In this thesis, we define synthetic tissues as any large and organised network of interconnected cell-like compartments which manifests emergent collective properties that are unachievable by the individual synthetic components. This broad definition will allow us to appreciate the vast range of complexity that can be incorporated into, and that can emerge from these synthetic multi-cellular systems.

Following a minimalistic approach, Villar and collegues developed a synthetic tissue that can undergo macroscopic folding driven simply by osmosis[26] (Fig. 1.6a). When two droplets at different osmolarities are joined to form a DIB, water molecules flow through the lipid bilayer towards the compartment with high osmolarity to balance the mismatch in osmotic concentration: as a result of this process, the droplets at high and low osmolarity respectively swell and shrink until the osmotic concentrations at either side of the lipid bilayer have equilibrated[56] (Fig. 1.6a*i*). When layers of osmotically mismatched droplets are formed, the flow of water causes the resulting network to deform due to the change in volume of its constituent parts. Using this principle, programmed folding of 3D-printed synthetic tissues was achieved[26] (Fig. 1.6a*iii*).

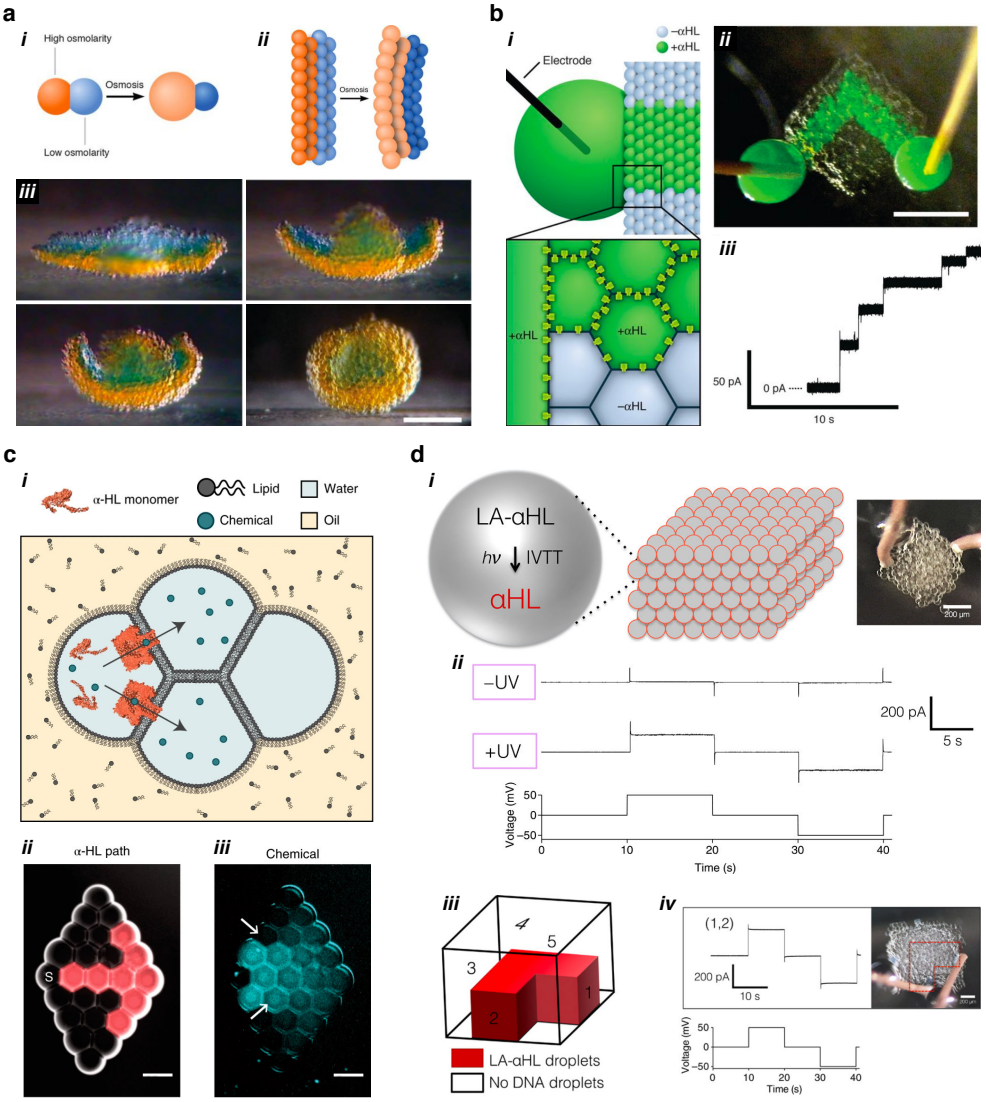

Fig. 1.6. Synthetic tissues. **a**, Shape change in 3D-printed synthetic tissues driven by osmosis. Osmotic flow of water across a DIB causes droplet at high and low osmotic concentration to swell or shrink, respectively (*i*). When layers of osmotically mismatched droplets are formed, the flow of water causes the resulting network to deform (*ii*). Using this principle, synthetic tissues undergo spontaneous folding driven by osmotic pressure[26] (*iii*, time interval between first and last picture: $8\,\mathrm{h}$). Scale bar: $200\,\mu\mathrm{m}$. **b**, Electrical signalling in synthetic tissues. When αHL-containing droplets are patterned within a 3D-printed synthetic tissue (*i*), an electrical signal is selectively transmitted through the conductive droplet pathway (*ii-iii*), while no ionic current is detected outside the pattern.[26] Scale bar: $500\,\mu\mathrm{m}$. **c**, Chemical communication in synthetic tissues. The formation of protein pores (αHL) allow for the controlled diffusion of small molecules within a synthetic tissue (*i*). In hand-made 2D constructs, patterns of αHL-containing droplets are formed (*ii*), and the diffusion of small molecule fluorophores is monitored over time[57] (*iii*). Scale bars: $200\,\mu\mathrm{m}$. **d**, Synthetic tissues that can respond to external stimuli. By encapsulating a light-activatable DNA construct and an IVTT system, functional αHL could be expressed *in-situ* within the synthetic tissue upon illumination with UV light (*i-ii*). When droplets containing the light-activatable DNA were patterned to form a pathway (*iii*), selective electrical signalling within this pathway is triggered by UV light[20] (*iv*). Scale bars: $200\,\mu\mathrm{m}$.

Electrical signalling was also demonstrated in 3D-printed synthetic tissues by incorporating protein pores in the lipid bilayers within the constructs. When droplets containing αHL were patterned within a synthetic tissue to form an interconnected pathway, an ionic current flowing through the conductive pathway was detected, upon application of a local potential at its ends (Fig. 1.6b). Conversely, no current was detected outside the patterned pathway,[26] demonstrating that fast electrical signals can be selectively transmitted through conductive droplet pathways patterned within synthetic tissues.

Using a similar strategy, controlled diffusion of small molecules through αHL pores was also demonstrated[57] (Fig. 1.6c). Specifically, a 2D synthetic tissue was manually assembled featuring a pathway of αHL-containing droplets (Fig. 1.6c): when a "sender" droplet was added at one end of the construct, diffusion of a small molecule fluorophore was tracked over time, demonstrating that it could only travel through bilayers permeabilised by αHL (Fig. 1.6c*iii*).

Lastly, more complex synthetic tissues capable of responding to external stimuli by *in-vitro* transcription and translation (IVTT) of functional proteins were also demonstrated[20,58] (Fig. 1.6d). By designing a light-activatable T7 promoter, protein expression in a synthetic tissue could be triggered upon illumination with ultraviolet light (UV). Fluorescent proteins and functional αHL pores could be expressed *in-situ* within the synthetic tissue upon illumination with UV light (Fig. 1.6d*i-ii*). Using the droplet-based 3D-printer, droplets containing the light-activatable DNA construct were patterned within a synthetic tissue: localised IVTT expression of αHL was triggered by UV light, and selective electrical signalling within the pathway was observed.[20] (Fig. 1.6d*iii-iv*). Alternatively, localised UV light was also used to generate patterns within a synthetic tissue composed of a homogeneous population of compartments containing the light-activatable DNA and the IVTT system.[58]

1.6 Scope and summary of this thesis

The work presented in this thesis represents a fundamental study of the properties of 3D-printed droplet networks and synthetic tissues, aimed at improving their fabrication and expanding their applicability.

In particular, in **Chapter 2**, we dissect the parameters that impact the geometry and surface energy of droplet interface bilayers, and demonstrate highly regular droplet packing in 3D-printed synthetic tissues by controlling the equilibrium contact angle θ_{DIB} at the droplet-droplet interface. As a result, we demonstrate the fabrication of synthetic tissues with single-droplet precision in three dimensions.

In **Chapter 3**, we investigate the assembly of 3D-printed networks and synthetic tissues to build large functional constructs. We use 3D-printed synthetic tissues fabricated individually as modular building blocks that can be combined in different ways to achieve different overall outputs. Furthermore, we show that assembled constructs are able to recover their functionalities, or "heal", after mechanical damage.

In **Chapter 4**, we outline a novel strategy to transfer 3D-printed droplet interface bilayer networks to aqueous phase, by retaining the architecture and the functionality of the internal lipid bilayers, and by forming a functional lipid bilayer at the interface with the aqueous bulk. As a result, we build synthetic tissues that can communicate with their surrounding aqueous environment, which represents a fundamental step towards functional constructs that can be directly interfaced with living tissues in physiological conditions.

Lastly, in **Chapter 5**, we discuss the overall outcomes of the presented work and outline possible avenues for future research, such as manufacturing

of synthetic tissues composed of cell-sized compartments, and engineered communication between synthetic constructs and living cells.

2

Controlled packing of droplets in 3D-printed networks

The complex functions seen in biological systems such as tissues, organs and organisms, derive not only from the activity of the individual cells, but also from their spatial arrangement and interactions with one another. In these systems, complex functionalities emerge from the coordinated interaction of the simpler functions performed by the individual components.[1] For example, if we consider the liver, the ability to filter nutrients perfusing from the portal triad and to discard waste products into the central vein emerges from the structural cooperation of hepatic, endothelial, and other cell types within the tissue, and from the formation of the specific architecture of the lobules.[59]

One aim of synthetic tissues is to mimic the complex and cooperative behaviour of biological tissues by patterning hundreds of droplets in large 3D-printed networks. While each droplet type carries out a simple function, collective functionalities can emerge from the structural interaction between them, such as chemical signalling,[57] electrical conductivity and shape change.[26] Since the final function of the synthetic tissues will depend on the precise positioning of each component within the 3D-printed network,

it is crucial to understand the parameters that direct packing of droplet interface bilayer networks in three dimensions.

In this chapter, we investigate the parameters dictating the arrangement of hundreds of picolitre-sized droplets within droplet networks. We find that the equilibrium contact angle between pairs of droplets within the networks (θ_{DIB}, Fig. 2.1) is a key geometrical constraint that dictates the packing arrangements of droplets within the networks. We demonstrate that, by controlling θ_{DIB}, we form extended regular lattices of droplets arranged in a hexagonally close-packed (hcp) fashion. Moreover, we observe that regular arrangements in the first layer of droplets, at the bottom of the networks, propagate upwards into the upper layers of the printed networks, generating regular lattices in three dimensions. Lastly, we apply our improved control over the packing and positioning of droplets within 3D-printed networks to the fabrication of synthetic tissues with functional features patterned at single-droplet resolution.

2.1 The equilibrium contact angle in droplet interface bilayers

When forming networks, aqueous droplets behave as deformable adhesive spheres that pack in three dimensions and assume space-filling polyhedral geometries. The extent to which a droplet deforms and its final geometry depend on the interaction with the neighbouring droplets and their arrangement in space. Consequently, understanding the parameters that direct packing of deformable spheres in three dimensions is key to achieving improved control over the fabrication of 3D-printed droplet networks.

We first considered geometrical constraints that would drive the packing of droplets in three dimensions. We based our initial investigations on Princen's seminal work on adhesive monodisperse oil-in-water emulsions, where they observed that the contact angle between a pair of droplets affected the packing of small assemblies.[60–62] In particular, from purely geometrical considerations, they identified a critical contact angle $\theta_c = 35.3°$ (approximated to 3 significant figures) above which the continuous phase trapped at the centre of four droplets arranged as a regular tetrahedron is excluded: they defined this as the *collapsed plateau border* condition.[60–62]

In our system, we can define the equilibrium contact angle in a DIB pair (θ_{DIB}) as half of the macroscopic angle measured at the meeting point of the two spherical oil-droplet interfaces and the flat droplet-droplet interface (Fig. 2.1a). This can be calculated from the radii (R_1 and R_2) and centre-to-centre distance (L) of the two droplets composing the DIB (see Chapter 6.3.7 for propagation of error), as:

$$\theta_{DIB} = \frac{1}{2} cos^{-1}\left(\frac{L^2 - R_1^2 - R_2^2}{2R_1R_2}\right) \tag{2.1}$$

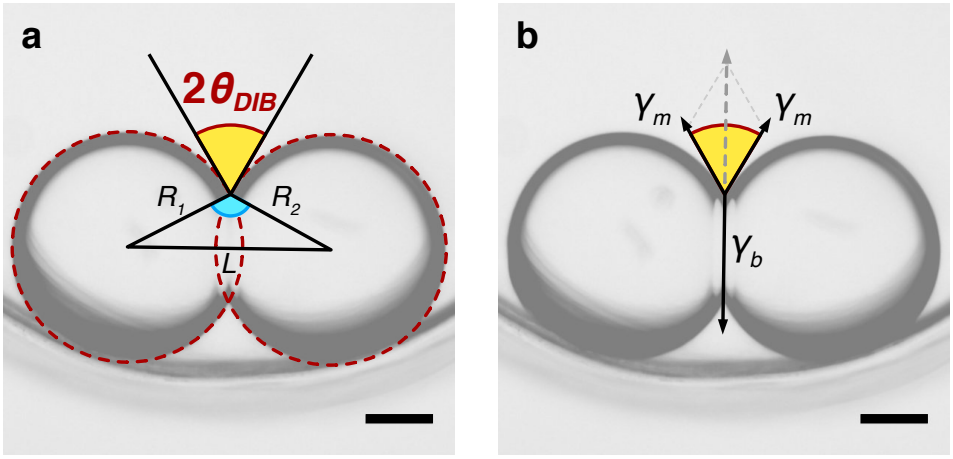

Fig. 2.1. The contact angle in DIB pairs. **a**, The equilibrium contact angle in a droplet pair forming a DIB (θ_{DIB}) can be defined as half of the macroscopic angle measured at the meeting point of the two spherical oil-droplet interfaces and the flat droplet-droplet interface. **b**, θ_{DIB} is a thermodynamic variable that reflects the balance of the surface tensions of the lipid monolayers (γ_m) and the lipid bilayer (γ_b) at the droplet-droplet interface. Scale bars: $150\,\mu$m.

The equilibrium contact angle θ_{DIB} is also a thermodynamic variable that reflects the balance of the surface tensions of the lipid monolayers (γ_m) and the lipid bilayer (γ_b) at the droplet-droplet interface (Fig. 2.1b).[32,63] Specifically, the surface tension of the lipid bilayer γ_b is linked to the surface tensions of the lipid monolayers γ_m by the relation:[64]

$$\gamma_b = 2\gamma_m + \Delta F \tag{2.2}$$

in which ΔF is the energy of adhesion in the system, or the work required to form the lipid bilayer per unit area. The formation of a lipid bilayer between the two droplets will spontaneously occur if $\Delta F < 0$, or in other words when the tension of the bilayer γ_b is lower than $2\gamma_m$. As shown in Fig. 2.1b, γ_b and γ_m are also linked by the Young equation:[65]

$$\gamma_b = 2\gamma_m cos(\theta_{DIB}) \tag{2.3}$$

By combining Eq. 2.2 and Eq. 2.3, we obtain the Young-Dupré equation:[63,64]

$$-\Delta F = 2\gamma_m(1 - cos(\theta_{DIB})) \tag{2.4}$$

which directly links the geometrical parameter θ_{DIB} to the adhesive energy ΔF. As a consequence, any factor that affects the surface energies in the system, such as the composition of the aqueous, lipid[66] and oil[56,67] phases, would be reflected in a change of θ_{DIB}.

We consequently investigated what parameters affected the equilibrium contact angle in our system by systematically measuring θ_{DIB} in hand-made droplet pairs composed of phosphate-buffered saline (PBS), formed in various lipid-oil mixtures (Fig. 2.2). By keeping the total lipid concentration constant at $1\,\mathrm{mM}$, we found that we could change θ_{DIB} in droplet pairs by simply varying the volume fraction of silicone oil (φ_{SIL}) in the oil mixture (composed of undecane and silicone oil, see chapter 6.3.3) and the

molar ratio of POPC (x_{POPC}) in the DPhPC/POPC lipid mixture used (Fig. 2.2b-e).

Specifically, we observed that θ_{DIB} increased linearly with increasing φ_{SIL} (at constant lipid composition of $1\,\mathrm{mM}$ DPhPC, Fig. 2.2f, $R^2 = 0.99$, Tab. 7.1), as well as with increasing x_{POPC} (at constant oil composition of $\varphi_{SIL} = 0.65$, Fig. 2.2g, $R^2 = 0.99$, Tab. 7.2). By sampling several combinations of oil and lipid compositions, we could identify a planar regression that describes the relationship of θ_{DIB} with respect to both φ_{SIL} and x_{POPC} ($R^2 = 0.99$, Fig. 2.2h, Tab. 7.9):

$$\theta_{DIB} = \frac{0.930\varphi_{SIL} + 0.368x_{POPC} - 0.238}{0.009} \tag{2.5}$$

This gave us a simple mathematical model from which we could predict θ_{DIB} from any given combination of φ_{SIL} and x_{POPC}.

Moreover, we investigated a range of other parameters that could affect θ_{DIB} in our system, such as temperature, droplet volume and lipid concentration (Fig. 7.2). We observed that temperature (range $4 - 60\,^{\circ}\mathrm{C}$, Fig. 7.2g) and droplet volume (range $0.52 - 200\mathrm{nL}$, Fig. 7.2h) had no significant effect on θ_{DIB} (see Tab. 7.3, 7.4 and 7.6). When the total concentration of lipids was varied in the oil solution (DPhPC lipids at constant $\varphi_{SIL} = 0.65$), there was no significant effect on θ_{DIB} above $1\,\mathrm{mM}$ lipids (up to $4\,\mathrm{mM}$), while we observed a rapid decrease in θ_{DIB} below this concentration (Fig. 7.2g). This behaviour indicated that, above a certain threshold concentration of lipids (calculated as $0.91\,\mathrm{mM}$ from the non-linear regression in Fig. 7.2g and Tab. 7.5), the oil solution was saturated with lipids, and an increase in lipid concentration had no effect on θ_{DIB}.

In summary, by screening lipid and oil compositions in a DIB system, we developed a simple mathematical model that allowed prediction of the contact angle in a droplet pair given a combination of φ_{SIL} and x_{POPC}. For

this example, we kept the internal aqueous composition constant as PBS. However, as we will show in sections 2.7 and 2.8, as well as in chapters 3 and 4, we can apply this method to a range of aqueous solutions to obtain similar predictive models.

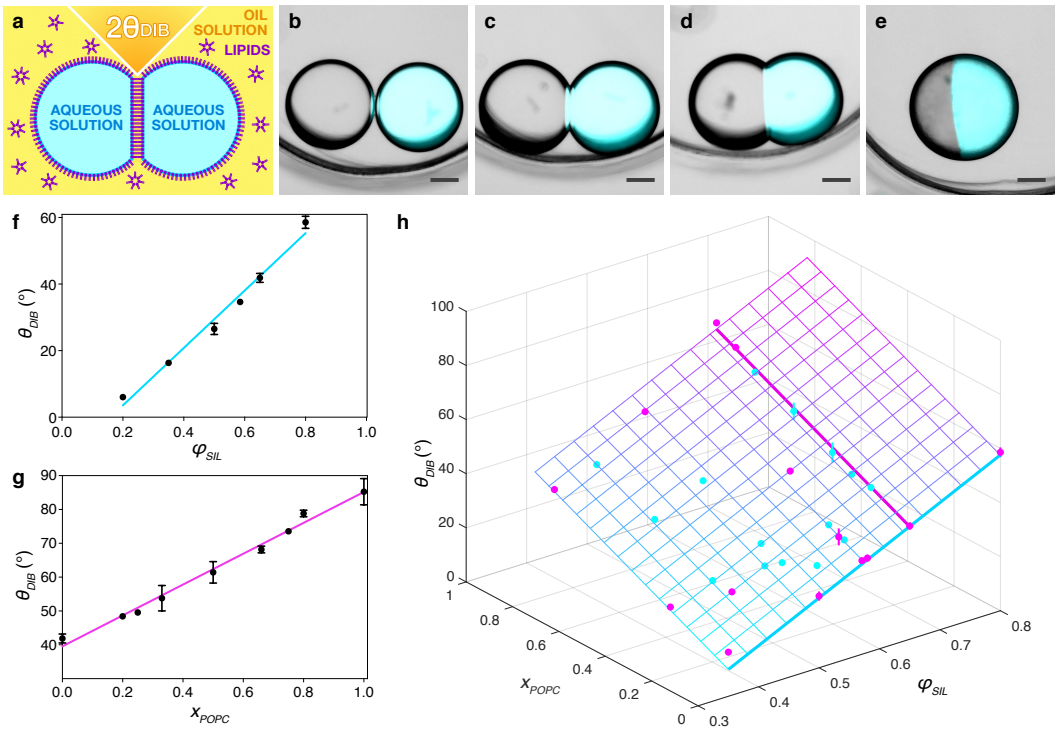

Fig. 2.2. The equilibrium contact angle θ_{DIB} depends on the lipid and oil compositions. **a**, Diagram of a droplet pair forming a DIB and definition of θ_{DIB}. **b-e**, Overlaid brightfield and fluorescence microscopy images of DIBs formed at various conditions. The membrane-impermeable fluorophore (Atto488, $10\,\mu$M) in the droplet on the right in each pair highlights the presence of a lipid bilayer compartmentalising the two aqueous compartments. Specific conditions: **b)** $\varphi_{SIL} = 0.20$, $x_{POPC} = 0$, $\theta_{DIB} = (6.0 \pm 0.7)°$; **c)** $\varphi_{SIL} = 0.50$, $x_{POPC} = 0$, $\theta_{DIB} = (26.5 \pm 1.7)°$; **d)** $\varphi_{SIL} = 0.80$, $x_{POPC} = 0$, $\theta_{DIB} = (53.4 \pm 0.9)°$; **e)** $\varphi_{SIL} = 0.65$, $x_{POPC} = 1$, $\theta_{DIB} = (85.3 \pm 3.8)°$. Scale bars: $150\,\mu$m. **f-g**, Plots showing the linear dependence of θ_{DIB} on φ_{SIL} **(f)** (at constant $x_{POPC} = 0$, $R^2 = 0.99$, Tab. 7.1) and on x_{POPC} **(g)** (at constant $\varphi_{SIL} = 0.65$, $R^2 = 0.99$, Tab. 7.2). **h**, Plot of the planar relationship of θ_{DIB} with both φ_{SIL} and x_{POPC} ($R^2 = 0.99$, Tab. 7.9). The linear regressions in **f** and **g** are highlighted, and points are colour coded in magenta or cyan depending on whether they lie above or below the regression plane, respectively. See Tab. 7.34 for n values.

2.2 The packing of deformable spheres

As discussed in Princen's seminal work, the value of the equilibrium contact angle in adhesive deformable droplet pairs affects their interaction and their assembly in small clusters.[60–62] In particular, they observed that for θ_{DIB} greater than the critical contact angle $\theta_c = 35.3°$, the continuous phase trapped in the middle of four droplets arranged as a regular tetrahedron is excluded. In the following sections, we will present the geometrical considerations that lead to the definition of the critical contact angle θ_c.[60–62]

2.2.1 Droplet triplets

Before analysing the geometry of clusters of four droplets arranged in 3D architectures, it is useful to focus first on the simpler case of three adhesive droplets of equal radius R on a plane (Fig. 2.3). Let us consider the case $\theta_{DIB} < 30°$ (Fig. 2.3a). In this case, the conformation that minimises the free energy of the system is when the droplet centres (P_1, P_2 and P_3) arrange at the vertices of an equilateral triangle. Upon contact, the droplets deform, forming a flat circular surface of radius r at each droplet-droplet interface. The droplets' centre-to-centre distances $\overline{P_iP_j}$, as well as the bilayer radius r, will depend on θ_{DIB}:

$$\overline{P_1P_2} = \overline{P_2P_3} = \overline{P_1P_3} = 2Rcos(\theta_{DIB}) \tag{2.6}$$

$$r = Rsin(\theta_{DIB}) \tag{2.7}$$

The distance between the centre of a droplet and the centre of the circular interface bilayer separating the remaining two droplets (e.g. P_1C_{23}) will be equal to:

$$\begin{aligned}\overline{P_1C_{23}} &= 2R\,[sin(60°)]\,cos(\theta_{DIB}) = \\ &= 2R\left[\frac{\sqrt{3}}{2}\right]cos(\theta_{DIB}) = \\ &= \sqrt{3}Rcos(\theta_{DIB})\end{aligned} \tag{2.8}$$

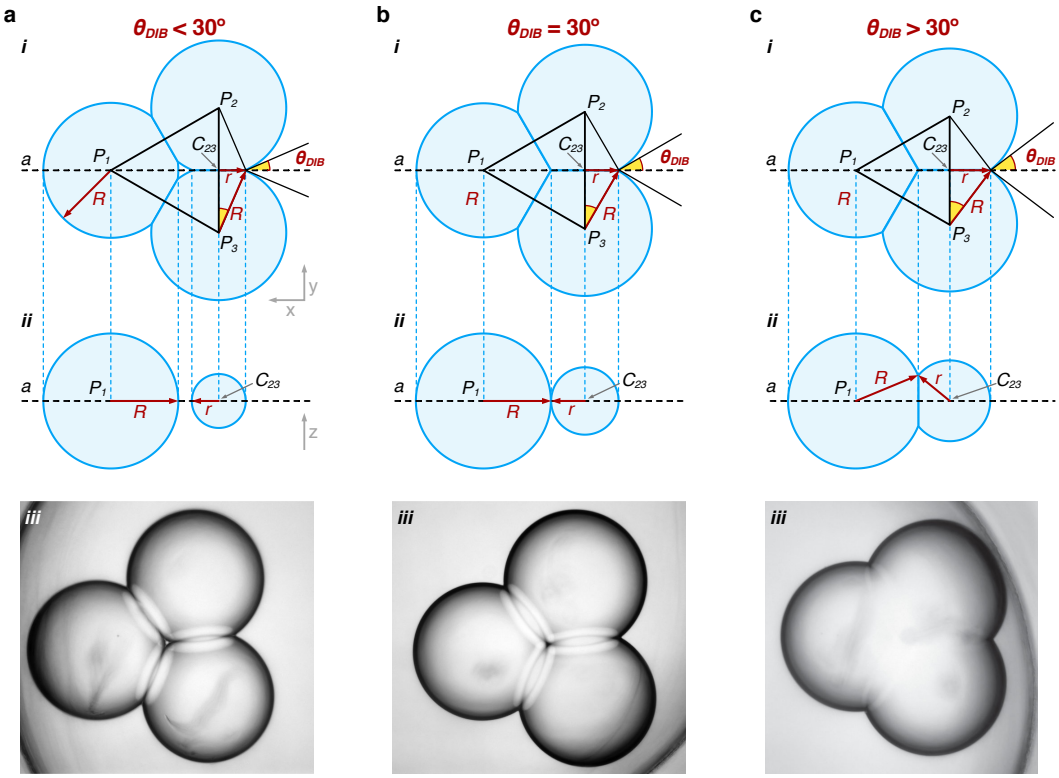

Fig. 2.3. Geometry of droplet triplets interfaced by lipid bilayers. **a**, A droplet triplet formed at $\theta_{DIB} < 30°$: graphical representation of a view from the top (*i*) and its cross-section on a vertical plane passing through the line *a* (*ii*). Brightfield image of a droplet triplet formed at $\theta_{DIB} = 25.8°$ (*iii*). At this condition, a small volume of continuous oil phase is present in the middle of the three droplets. **b**, A droplet triplet formed at $\theta_{DIB} = 30°$: at this critical condition, the lipid bilayers separating the three droplets touch in the middle point of the triplet (top view in *i*, and cross-section in *ii*). Brightfield image of a triplet formed at $\theta_{DIB} = 30°$ (*iii*). **c**, A droplet triplet formed at $\theta_{DIB} > 30°$: at this condition, the continuous oil phase is excluded from the middle of the droplet triplet (*i*). However, due to the large θ_{DIB}, the droplet triplet contracts towards the middle and the lipid bilayers meet in a vertical line (*ii*). Brightfield image of a triplet formed at $\theta_{DIB} = 57.5°$ (*iii*).

Now, let us find the minimum critical contact angle θ^*_{DIB} at which the three circular bilayer areas meet in the middle of the droplet triplet, or in other words, the minimum contact angle for which the oil in the middle of the three droplets is excluded. As shown in Fig. 2.3b*ii*, this condition is:

$$\overline{P_1C_{23}} = R + r \tag{2.9}$$

By substituting Eq. 2.7 and 2.8, we obtain:

$$\begin{aligned} R\sqrt{3}cos(\theta^*_{DIB}) &= R + Rsin(\theta^*_{DIB}) \\ \sqrt{3}cos(\theta^*_{DIB}) &= 1 + sin(\theta^*_{DIB}) \\ \sqrt{3} &= \frac{1}{cos(\theta^*_{DIB})} + \frac{sin(\theta^*_{DIB})}{cos(\theta^*_{DIB})} \\ \sqrt{3} &= sec(\theta^*_{DIB}) + tan(\theta^*_{DIB}) \\ sec^2(\theta^*_{DIB}) &= (\sqrt{3} - tan(\theta^*_{DIB}))^2 \end{aligned} \tag{2.10}$$

Since $sec^2(\theta^*_{DIB}) = 1 + tan^2(\theta^*_{DIB})$, we obtain:

$$\begin{aligned} 1 + tan^2(\theta^*_{DIB}) &= 3 + tan^2(\theta^*_{DIB}) - 2\sqrt{3}tan(\theta^*_{DIB}) \\ 2\sqrt{3}tan(\theta^*_{DIB}) &= 2 \\ tan(\theta^*_{DIB}) &= \frac{1}{\sqrt{3}} \\ \theta^*_{DIB} = tan^{-1}\left(\frac{1}{\sqrt{3}}\right) &= 30° \qquad (Q.E.D.) \end{aligned} \tag{2.11}$$

Hence we have proven that, at the critical contact angle $\theta^*_{DIB} = 30°$, the three bilayers meet at the centre of a droplet triplet, consequently excluding the continuous oil phase. To observe this experimentally, we formed small clusters of three droplets at conditions leading to θ_{DIB} below (Fig. 2.3a*iii*), equal to (Fig. 2.3b*iii*), and above (Fig. 2.3c*iii*) $30°$. At $\theta_{DIB} < 30°$ ($\varphi_{SIL} = 0.50$, $x_{POPC} = 0$, $\theta_{DIB} = 25.8°$), we observed an oil gap in the middle of the droplet cluster (Fig. 2.3a*iii*). At $\theta_{DIB} = 30°$ ($\varphi_{SIL} = 0.54$, $x_{POPC} = 0$), we observed that the three lipid bilayers, separating the droplets from each other, met at

the central point of the droplet, excluding (macroscopically) the oil phase. Above $30°$, the continuous oil phase was still excluded, however the droplets' centre-to-centre distances reduced, leading to a contraction of the droplet triplet (Fig. 2.3c*iii*).

2.2.2 Droplet quartets

Let us now consider the case of four droplets of equal radius R, arranged in a way that their four centres (P_1, P_2, P_3, and P_4) are positioned at the vertices of a regular tetrahedron (Fig. 2.4a*i*). Similarly to the case of a droplet triplet, the droplets will deform upon contact to form flat surfaces at the droplet-droplet interfaces. For low values of θ_{DIB}, these interfaces will consist in circles of radius r, and a small volume of continuous oil phase will be present at the tetrahedral pocket in the middle of the droplet quartet.

We aim to find the critical contact angle θ_c at which the four lipid bilayers meet at the tetrahedral point in the middle of the quartet, excluding the continuous oil phase. Let us consider the triangle defined by the centres of two droplets (e.g. P_1 and P_2), and the centre of the circular bilayer separating the remaining two droplets in the quartet (in this case C_{34}) (Fig. 2.4a*i*). If we isolate this plane (Fig. 2.4a*ii*), we can observe a cross-section of the tetrahedral pocket in the middle of the four droplets. In order for this pocket to collapse into a point, the two flat lipid bilayers separating droplets 1 and 2 (centred in C_{12}) and the one separating droplets 3 and 4 (centred in C_{34}) have to meet. Consequently, at the critical contact angle $\theta_{DIB} = \theta_c$ we will have:

$$\overline{C_{12}C_{34}} = 2r \tag{2.12}$$

We can then consider the Pythagoras Theorem for the triangle of vertices P_2, C_{12} and C_{34}:

$$\overline{P_2C_{34}}^2 = \overline{C_{12}C_{34}}^2 + \overline{P_2C_{12}}^2 \tag{2.13}$$

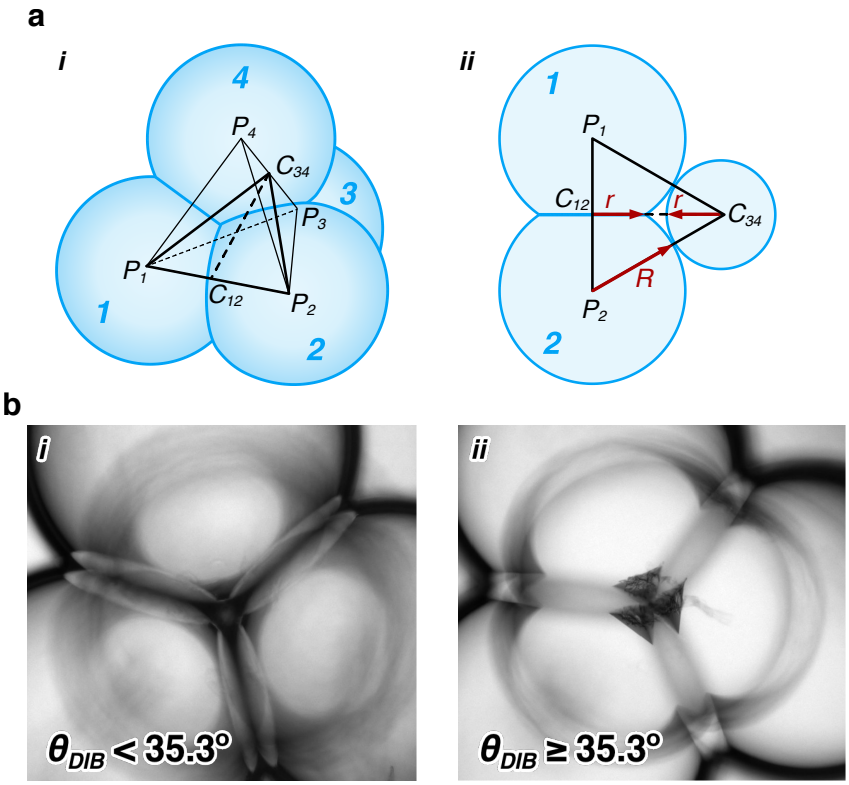

Fig. 2.4. Geometry of droplet quartets interfaced by lipid bilayers. **a**, Geometrical representation of a cluster of four droplets arranged so that their centres (P_1-P_4) lie at the vertices of a regular tetrahedron (*i*). C_{12} and C_{34} represent the centres of the flat bilayer interfaces separating droplets 1 to 2 and 3 to 4, respectively. Cross-section of the cluster on the plane passing through the points P_1, P_2 and C_{34} (*ii*). **b**, Brightfield images of droplet quartets formed at θ_{DIB} =25.8° (*i*) and at (θ_{DIB} =36.3°).

Substituting $\overline{C_{12}C_{34}} = 2r$ (Eq. 2.12), $\overline{P_2C_{12}} = Rcos(\theta_c)$ (Eq. 2.6), $\overline{P_2C_{34}} = \sqrt{3}Rcos(\theta_c)$ (Eq. 2.8), and $r = Rsin(\theta_c)$ (Eq. 2.7), we obtain:

$$\overbrace{3R^2cos^2(\theta_c)}^{\overline{P_2C_{34}}^2} = \overbrace{4r^2}^{\overline{C_{12}C_{34}}^2} + \overbrace{R^2cos^2(\theta_c)}^{\overline{P_2C_{12}}^2}$$

$$3R^2cos^2(\theta_c) = 4R^2sin^2(\theta_c) + R^2cos^2(\theta_c)$$

$$3cos^2(\theta_c) = 4sin^2(\theta_c) + cos^2(\theta_c)$$

$$2cos^2(\theta_c) = 4sin^2(\theta_c)$$

$$tan^2(\theta_c) = \frac{1}{2}$$

$$tan(\theta_c) = \frac{1}{\sqrt{2}}$$

$$\theta_c = tan^{-1}\left(\frac{1}{\sqrt{2}}\right) = 35.3° \quad (3s.f.) \qquad (Q.E.D.) \tag{2.14}$$

Therefore, $\theta_c = 35.3°$ (calculated to 3 s.f.) represents the critical contact angle above which the continuous oil phase is excluded from the tetrahedral pocket in the middle of the four droplets.

We observed this experimentally by forming clusters of four droplets, arranged as a regular tetrahedron, at different θ_{DIB} (Fig. 2.4b). At $\theta_{DIB} < \theta_c$ ($\varphi_{SIL} = 0.50$, $x_{POPC} = 0$, $\theta_{DIB} = 25.8°$), we could observe a tetrahedral oil pocket in the middle of the droplet cluster by optical imaging (Fig. 2.4b*i*). When we imaged a droplet cluster formed at conditions leading to $\theta_{DIB} \geq \theta_c$ ($\varphi_{SIL} = 0.60$, $x_{POPC} = 0$, $\theta_{DIB} = 36.6°$), we could observe a characteristic diffraction pattern with 3-fold symmetry. This pattern was likely due to the diffraction of light encountering interfaces at different refractive indices ($\eta_{PBS} = 1.33$ and $\eta_{oil} = 1.42$ for PBS buffer and undecane-silicone oil mixture, respectively). We will discuss the optical properties of DIB systems and the resulting imaging issues in chapter 2.7. However, we assumed that the presence of the diffraction pattern shown in Fig. 2.4b*ii* and the absence of a visible gap were indication that the tetrahedral pocket at the middle of the four droplets had collapsed (macroscopically) to a point.

2.3 Packing structures in 3D-printed networks

In section 2.1 we discussed the modulation of the contact angle θ_{DIB} in a droplet pair, and that this can be also predicted from Eq. 2.5. In Section 2.2, we formalised the geometry of small clusters of droplets and demonstrated that, from geometrical considerations, we can identify a critical contact angle $\theta_c = 35.3°$ at which the continuous oil phase can be excluded from the middle of clusters of 4 droplets arranged in 3D as a regular tetrahedron (Eq. 2.14).

From this, we were interested in investigating the impact of θ_{DIB} on the packing of hundreds of droplets within 3D-printed networks.

Similarly to sections 2.1 and 2.2, we varied the composition of the oil-lipid solution (in terms of φ_{SIL} and x_{POPC}) to obtain networks of hundreds of picolitre droplets printed at a wide range of θ_{DIB} conditions. We used our laboratory-built 3D-printer[26] to fabricate networks composed of $7 \times 8 \times 4$ (in x, y and z directions) picolitre-sized aqueous droplets (PBS, $100\,\mu\mathrm{m}$ diameter, $\sim 524\,\mathrm{pL}$ volume, droplet ejection frequency $f_{drop} = 0.5\,\mathrm{s}^{-1}$), positioned line-by-line and layer-by-layer according to a hexagonally close-packed (hcp) design (Fig. 2.5a and 7.3a-c, see chapter 6.3.4). To image lipid monolayers and bilayers, we added a water-soluble fluorescent dye with high affinity to lipid membranes[68] (Atto550M, at a final concentration of $3\,\mu\mathrm{M}$, Fig. 7.3d-e) to the aqueous buffer. As shown in Fig. 2.5b, we could clearly resolve the lipid bilayers and monolayers in the first layer of droplets in printed networks using fluorescent confocal microscopy (Fig. 2.5b*i*). However, due to optical aberrations generated by the different refractive indices of the aqueous and oil phases, the upper layers of the networks were increasingly difficult to resolve, and only incomplete or distorted images could be acquired (Fig. 2.5b*ii-iv*, see chapter 2.7 for further discussion about the optical properties of droplet networks).

We developed a script in MATLAB® (Mathworks) to extract quantitative information on the arrangement of droplets within printed networks based on the fluorescent confocal images of the first layers. This script could identify the lipid bilayers and monolayers by application of a ridge detection algorithm.[69] Based on this information, the software segmented the images and classified regions of the picture as either droplets or oil inclusions (i.e. oil pockets trapped by aqueous droplets in the middle of the networks) (Fig. 2.5c). This classification was performed based on the morphology of the segmented areas of the image: only regions that exhibited mostly convex

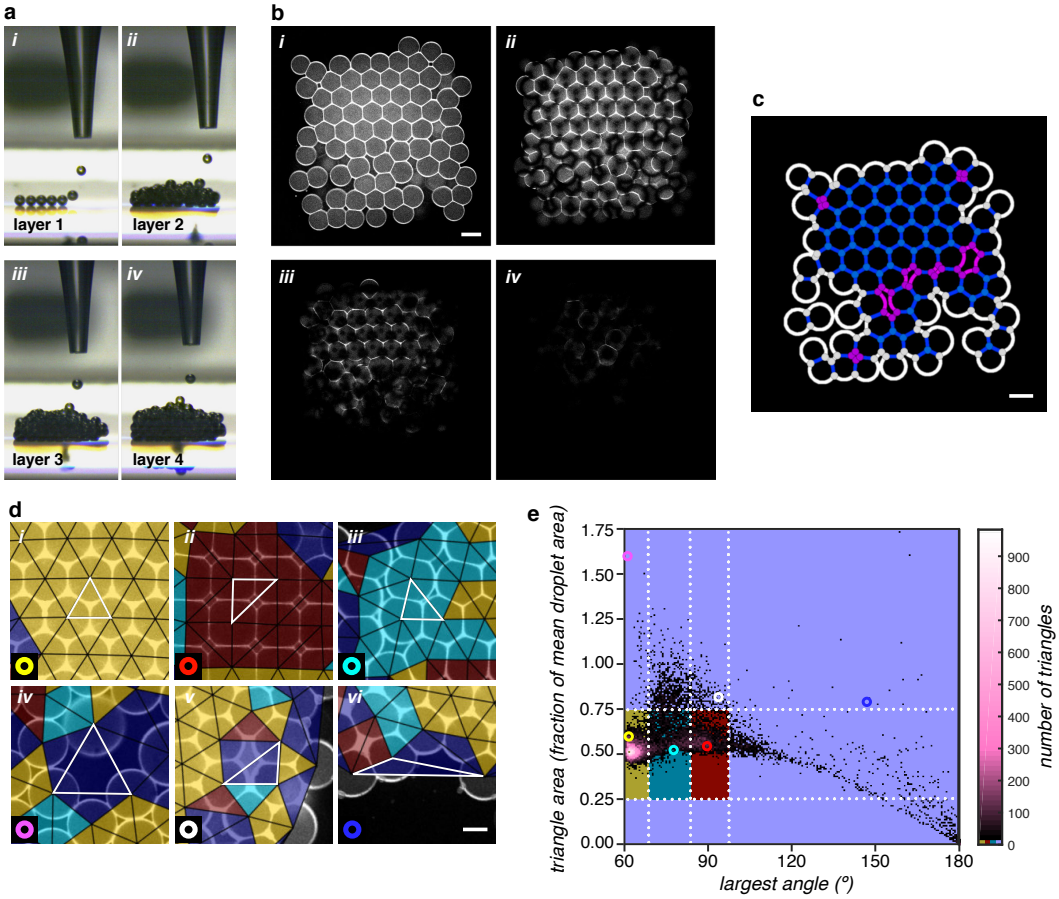

Fig. 2.5. Classification of droplet packing arrangements based on Delaunay triangulation. **a**, Images of a droplet network fabricated by 3D-printing. Picolitre-sized droplets are positioned line-by-line and layer-by-layer to form constructs composed of $7 \times 8 \times 4$ droplets (in x, y and z direction). **b**, Confocal fluorescent images of the first (*i*), second (*ii*), third (*iii*) and fourth (*iv*) layers of droplets within a printed network, tagged with Atto550M fluorescent dye. Due to optical aberrations, only the packing structure of the first droplet layer can be clearly resolved. **c**, Segmented image of **a**, showing the correct classification of lipid bilayers (blue), monolayers (white) and oil inclusions (magenta). **d**, Classification of droplet packing arrangements based on Delaunay triangulation. By joining the centres of neighbouring droplets, we can classify the packing arrangement of each triplet of droplets as *hexagonal* (indicated with yellow equilateral triangles, *i*), *square* (red right-angled triangles, *ii*), *amorphous* (cyan triangles, *iii*), and *not packed* (blue triangles, *iv*). **e**, Bivariate distribution of the largest angle in each triangle versus the triangle area. Two prevalent clusters corresponding to the hexagonally-packed (yellow area) and square-packed (red area) were identified.

surfaces were counted as droplets, while the other regions were classified as oil inclusions. By comparing Fig. 2.5b*i* and Fig. 2.5c, it is possible to see that the segmentation algorithm was able to correctly identify areas of the picture occupied by droplets, or oil inclusions, or external to the network.

To analyse the packing structure of droplet networks, we assigned packing types to triplets of droplets in the first layer of the networks based on Delaunay triangulation[70] (Fig. 2.5d). Specifically, the triangulation was generated by joining the centres of neighbouring triplets of droplets in the bottom layer of the network: the geometry of the resulting triangle reflected the relative arrangements of the three droplets with respect to each other. For instance, triplets of droplets arranged in a regular hexagonal lattice (honeycomb) described equilateral triangles (Fig. 2.5d*i*), while droplets arranged as a regular square lattice described right-angled triangles (Fig. 2.5d*ii*). These 2D lattices corresponded to 'hexagonally close-packed' (hcp) and 'body-centred cubic' (bcc) 3D lattices, respectively (see section 2.6 for further discussion on the propagation of regular lattices in printed networks).

By analysing confocal images of 129 droplet networks printed at a wide range of different conditions, we observed that the *hexagonal* and *square* arrangements of droplets represented the two most prevalent regular motifs (Fig 2.5e). We also observed a range of irregular arrangements that we classified as *amorphous* (Fig 2.5d*iii* and cyan area in Fig. 2.5e) or *not packed* (Fig 2.5d*iv-vi* and blue area in Fig. 2.5e) depending on weather the droplets in the triplet were in contact or not.

In summary, this analysis served as a powerful tool to automatically assess, quantify and compare topological features of printed networks fabricated at various θ_{DIB}. In addition to packing arrangements, the script quantified the fraction of network area occupied by oil inclusions (Fig. 2.5c), the number of droplets that had fallen from the upper layers to the bottom layer (Fig. 7.3), and the variation in droplet size (see chapter 6.3.8).

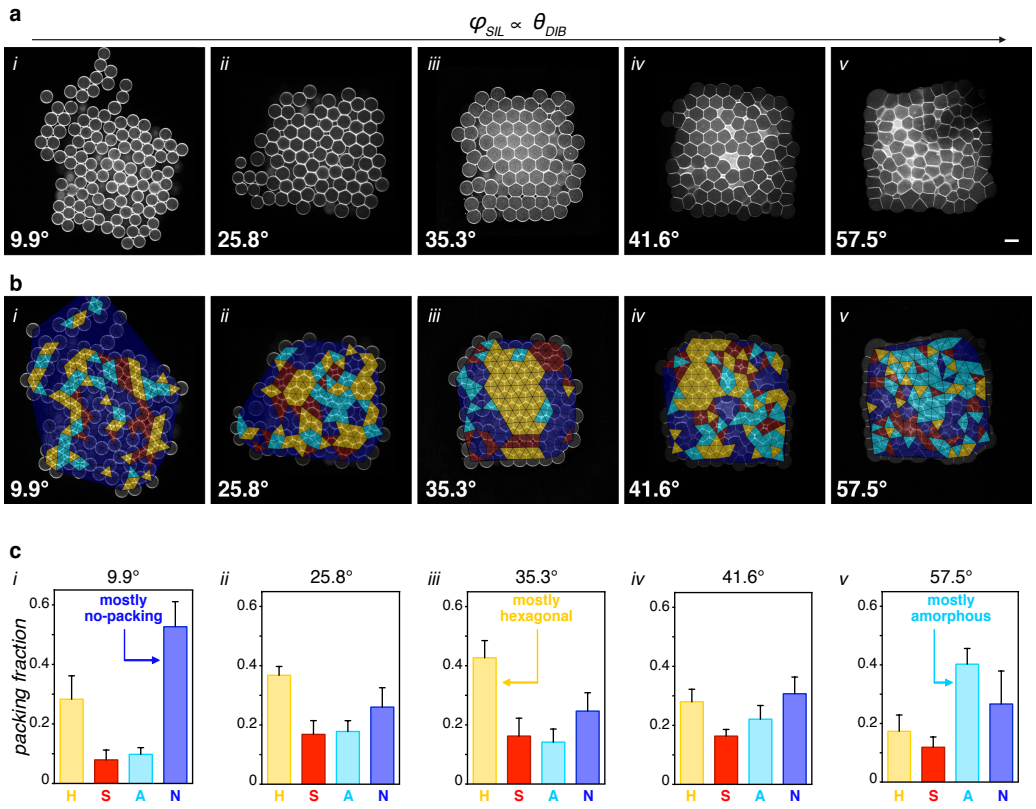

Fig. 2.6. The effect of θ_{DIB} on the packing of droplets in 3D-printed networks. **a-b**, Confocal images of the first layer of droplets in 3D-printed networks (**a**) and overlays of the packing analysis based on Delaunay triangulation (**b**). **c**, Quantification of the area fractions of the four packing arrangements: hexagonal (H, yellow), square (S, red), amorphous (A, cyan), and no packing (N, blue). Depending on θ_{DIB}, obtained by varying φ_{SIL} at constant $x_{POPC} = 0$, the networks showed a different prevalent packing structure: from mostly not packed at $\theta_{DIB} = 9.9°$, to mostly hexagonal at $\theta_{DIB} = \theta_c = 35.3°$, to mostly amorphous at $\theta_{DIB} = 57.5°$. Scale bars: $100\,\mu$m.

2.4 Quantification of packing types in droplet networks

We wanted to study the dependency of the droplet packing in 3D-printed networks on the equilibrium contact angle θ_{DIB}. As discussed in section 2.1, we can modulate θ_{DIB} by varying both the oil mixture (φ_{SIL}) and the lipid composition (x_{POPC}) (Fig. 2.2f-h). We first compared printed networks formed at various θ_{DIB} obtained by varying φ_{SIL} at a constant lipid composition of $1\,\mathrm{mM}$ DPhPC (i.e. $x_{POPC} = 0$).

When we 3D-printed networks at low θ_{DIB} (9.9°, obtained at $\varphi_{SIL} = 0.35$), the droplets were mostly not packed (0.53 ± 0.08 area fraction, Fig. 2.6a*i*, b*i* and c*i*), and networks showed high amounts of defects, such as oil inclusions (0.18 ± 0.01 area fraction, Fig. 2.7a) and droplets falling from the upper layers (65 ± 18 % droplet excess, Fig. 2.7b). Conversely, at high θ_{DIB} (57.5°, obtained at $\varphi_{SIL} = 0.80$), droplets in printed networks mostly arranged in an amorphous fashion (0.40 ± 0.05 area fraction, Fig. 2.6a*v*, b*v* and c*v*), together with abundant falling of droplets from the upper layers (61 ± 24 %, Fig. 2.7b) and droplet size variation (27.9 ± 8.4 coefficient of variation, Fig. 2.7c).

Interestingly, when θ_{DIB} was equal to the critical contact angle $\theta_c = 35.3°$, we observed the largest fraction of hexagonal packing (0.43 ± 0.06 area fraction, Fig. 2.6a*iii*, b*iii* and c*iii*), with low extents of oil inclusions (0.06 ± 0.01 area fraction, Fig. 2.7a), droplet excess (13 ± 6 %, Fig. 2.7b) and droplet size variation (8.2 ± 1.5 coefficient of variation, Fig. 2.7c).

In summary, our analysis highlighted three different scenarios: 1) $\theta_{DIB} \ll \theta_c$: printed droplets interact weakly, due to the low θ_{DIB}, and resulting networks are mostly not packed; 2) $\theta_{DIB} \gg \theta_c$: droplets interact strongly, due to the high θ_{DIB}, and networks show large amounts of amorphous packing; 3)

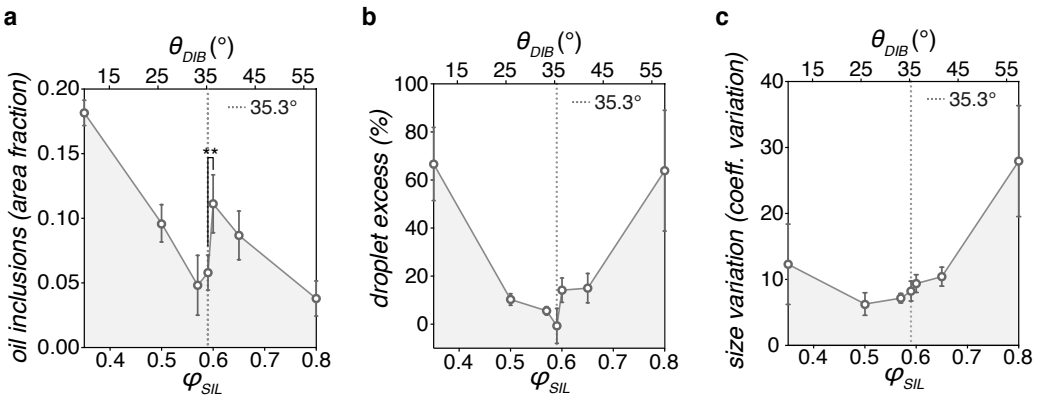

Fig. 2.7. Quantification of printing defects. **a**-**c**, Plots showing the area fraction occupied by oil inclusions (**a**), excess of droplets in the first layer (**b**), and droplet size variation (**c**) with respect to changes in φ_{SIL}, and consequently of θ_{DIB} (see chapter 6.3.8 for details on the analysis, and Tab. 7.18 and 7.19 for statistical analysis). Dashed lines represent θ_c.

$\theta_{DIB} \simeq \theta_c$: droplet networks show extended regions of regular hexagonal packing, with minimal defects.

We reason that at the critical contact angle the tetrahedral arrangements of droplets imposed during printing are maintained with minimal displacement. Specifically, to achieve regular hcp packing in a printed network, each droplet needs to maintain a position as close as possible to the one imposed by the printing nozzle. However, droplets also need to deform to form a lipid bilayer between each other, which provides the cohesive energy necessary for the network to support itself. Both the displacement of droplets caused by the formation of the lipid bilayer and the area of the lipid bilayer depend on θ_{DIB}. If we consider two droplets of equal radius R forming a DIB (as in Fig. 2.1), we can define their centre-to-centre distance $L = 2Rcos(\theta_{DIB})$. Consequently, when forming a lipid bilayer, the two droplets will move towards each other of a displacement distance d equal to $2R - L$, which depends on θ_{DIB} as:

$$\begin{aligned} d &= 2R - L = \\ &= 2R - 2Rcos(\theta_{DIB}) = \\ &= 2R(1 - cos(\theta_{DIB})) \end{aligned} \tag{2.15}$$

The lipid bilayer area also depends on θ_{DIB}: the bilayer area in a droplet pair consists of a circle of radius $r = Rsin(\theta_{DIB})$, from Eq. 2.7. Consequently, for a droplet pair, the bilayer area A_b will increase with θ_{DIB} following the equation:

$$\begin{aligned} A_b &= \pi r^2 = \\ &= \pi R^2 sin^2(\theta_{DIB}) \end{aligned} \tag{2.16}$$

However, in a printed network, where each droplet is surrounded by several other droplets (12 for hcp), Eq. 2.16 is only true below the critical contact angle θ_c: above this critical contact angle droplets cannot freely form new

bilayer area because they already have used all the available surface to form bilayers with their neighbours.

To visualise this scenario, let us consider the simplified 2D case of seven deformable disks of radius R arranged as a *flower*, i.e. one disk surrounded by six others as shown in Fig. 2.8. In this model, the seven disks have no height, and therefore can only deform on the xy plane, but not in the z direction. As discussed in section 2.2, when considering 2D clusters, the critical contact angle at which the continuous phase is excluded is $\theta^*_{DIB} = 30°$ (Eq. 2.11, see section 2.2.1). For $\theta_{DIB} < \theta^*_{DIB}$ (Fig. 2.8a), the displacement distance d will follow Eq. 2.15. In this simplified model, the adhesive interaction between the central disk and the six surrounding disks is proportional to the 1D bilayer interface A_b, equal to the sum of the six flat segments of length $2r$ that separate the central disk with each of the six surrounding disks. For $\theta_{DIB} < \theta^*_{DIB}$, A_b will depend on θ_{DIB} according to the equation:

$$\begin{aligned} A_b &= 6 \times 2r = \\ &= 12Rsin(\theta_{DIB}) \end{aligned} \tag{2.17}$$

However, A_b can increase with θ_{DIB} only until $\theta_{DIB} = \theta^*_{DIB}$ (Fig. 2.8b), at which A_b would reach its maximum value (Fig. 2.8b):

$$A_b(max) = 12Rsin(30°) = 6R \tag{2.18}$$

Above the critical contact angle θ^*_{DIB}, A_b cannot freely increase with θ_{DIB} because all the available interface with the surrounding disks has already been used to form a bilayer. Consequently, while increasing θ_{DIB} will lead to increases in the displacement distance d (the surrounding droplets can still reduce the centre-to-centre distances among each other), this will not lead to increases in bilayer interface above its maximum value $A_b(max)$ (Fig. 2.8c). In a real physical system, for $\theta_{DIB} > \theta^*_{DIB}$, the droplets in the cluster would rearrange into different conformations to accommodate their reduced centre-

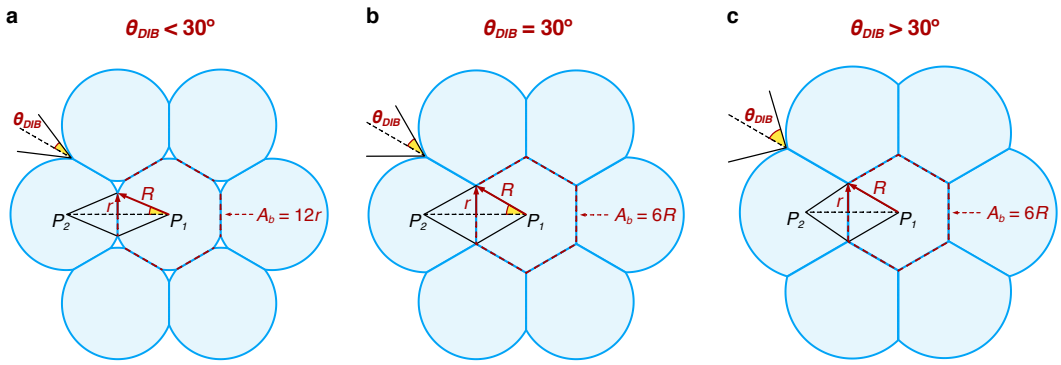

Fig. 2.8. The effect of increasing θ_{DIB} in droplet networks. **a-c**, Simplified 2D case of seven deformable disks of radius R arranged as a *flower*, i.e. with one of the disks surrounded by the remaining six others in an hexagonal fashion. When $\theta_{DIB} < 30°$ (**a**), the lipid bilayer interface A_b of the central disk with the surrounding disks depends on θ_{DIB}, as $A_b = 6 \times 2r = 12Rsin(\theta_{DIB})$ (Eq. 2.17). When θ_{DIB} reaches $30°$ (the critical angle for 2D clusters, see Eq. 2.11, section 2.2.1) (**b**), A_b reaches its maximum value $A_b(max) = 6R$. Further increases in θ_{DIB} (**c**) do not lead to the formation of more bilayer area A_b, while still reducing the centre-to-centre distances between droplets and therefore causing distortions of the droplet lattice.

to-centre distances, leading to non-hexagonal arrangements. This simple example illustrates how above the critical contact angle, increasing θ_{DIB} leads only to increasing droplet displacement towards irregular arrangements, while not providing significant increases in bilayer area (Fig. 2.8c).

Similarly, we suggest that in large 3D-printed networks, an increase in θ_{DIB} above the critical contact angle θ_c does not lead to a significant increase in lipid bilayer area. However, the consequent increase in droplet displacement d from the initial position imposed by the nozzle leads to distortion of the printed lattice and accumulation of defects.

Our observations supported our reasoning. In particular, when $\theta_{DIB} \ll \theta_c$, we observed loosely packed networks, with prevalent no packing droplet arrangements (Fig. 2.6a*i*, b*i* and c*i*), and large amounts of oil inclusions (Fig. 2.7a) and droplet falling from the upper layers of the networks (Fig. 2.7b). These observations suggested that, at low θ_{DIB}, the adhesive energy provided by the small bilayer areas was not sufficient to ensure the cohesion of the droplets within the networks, causing the observed defects.

Conversely, when $\theta_{DIB} \gg \theta_c$, we observed highly cohesive networks, characterised by large areas of amorphous packing (Fig. 2.6a*v*, b*v* and c*v*), together with a small fraction of oil inclusions (Fig. 2.7a), large amounts of droplet excess (Fig. 2.7b) and of droplet size variability (Fig. 2.7c). These effects resulted from the high adhesive energy at this condition, which caused the droplets to decrease their centre-to-centre distances, leading to the formation of a distorted lattice. Interestingly, in this case the observed droplet excess in the first layer (Fig. 2.7b) was most likely not caused by the "rolling" of droplets from the upper layers, but by the formation of large gaps between small clusters of tightly packed droplets, which droplets from the top layers could occupy.

At $\theta_{DIB} \simeq \theta_c$, we found highly regular networks, with extended regions of hexagonal droplet arrangement (Fig. 2.6a*iii*, b*iii* and c*iii*), together with minimal amounts of defects, such as oil inclusions (Fig. 2.7a), droplet rolling (Fig. 2.7b) and size variation (Fig. 2.7c). This finding confirmed that, at this critical condition, the adhesive energy among the droplets was sufficient to ensure the cohesion of the printed structure, with minimal displacement of droplets from their initial position imposed by the printing nozzle.

2.5 The kinetics of DIB formation affect the hexagonal packing of droplets

The fabrication of droplet networks and synthetic tissues by 3D-printing is a dynamic process, in which picolitre-sized droplets are sequentially generated and deposited droplet-by-droplet, line-by-line and layer-by-layer to form 3D structures. Consequently, we hypothesised that the kinetics of DIB formation, i.e. the rate of increase in the non-equilibrium contact angle θ from $0°$ to

θ_{DIB}, would also have an impact on the final packing arrangement of droplets in printed networks.

As discussed in section 2.1, we can modulate θ_{DIB} in droplet pairs by varying the volume fraction of silicone oil (φ_{SIL}) or the molar fraction of POPC (x_{POPC}) in the lipid mixture (Fig. 2.2f-h). By using the planar regression that describes the variation of θ_{DIB} with respect to both φ_{SIL} and x_{POPC} (Eq. 2.5), we can identify multiple combinations of φ_{SIL} and x_{POPC} that lead to the same equilibrium θ_{DIB}.

We were consequently interested in understanding the effect of the lipid composition, at fixed final θ_{DIB}, on the kinetics through which the thermodynamic equilibrium is reached in a DIB system, and therefore on the packing of hundreds of droplets in printed networks. To this end, we tested several conditions with θ_{DIB} ranging from $35.3°$ to $37.2°$ and x_{POPC} ranging from 0.00 to 0.22 (Fig. 7.6 and Tab. 7.10). For simplicity, we limit our discussion here to the comparison of the kinetics of bilayer formation in droplet pairs formed in three different lipid-oil solutions with the same final $\theta_{DIB} = 36.3°$ (from Eq. 2.5). Specifically, we measured the evolution of the contact angle θ over time (Fig. 2.9a, b) and compared the different bilayer formation kinetics of the following lipid-oil (LO) conditions:

	φ_{SIL}	x_{POPC}	θ_{DIB}
LO_1	0.60	0.00	36.3°
LO_2	0.55	0.13	36.3°
LO_3	0.52	0.20	36.3°

Tab. 2.1. List of lipid-oil (LO) compositions used to investigate the effect of lipid bilayer formation kinetics on the packing of droplets in 3D-printed networks.

When POPC was added to the lipid mixture, we observed a biphasic behaviour in the kinetics of DIB formation: an initial fast increase in θ was followed by a slow equilibration to reach the final value θ_{DIB} (Fig. 2.9b). For instance, for

the intermediate condition LO_2 ($\varphi_{SIL} = 0.55$ and $x_{POPC} = 0.13$), θ rapidly increased to a non-equilibrium value of $30°$ within $2\,\mathrm{s}$ after initial contact, but required more than $15\,\mathrm{min}$ to reach $\theta_{DIB} = 36.3°$ (Fig. 2.9b, purple line). At high POPC concentration (LO_3, $\varphi_{SIL} = 0.52$ and $x_{POPC} = 0.20$), we observed a similar biphasic behaviour, however the final contact angle θ_{DIB} was reached with an even slower kinetics (after $15\,\mathrm{min}$, θ only reached $30°$, and θ_{DIB} was reached after approximately $30\,\mathrm{min}$) (Fig. 2.9b, magenta line). By comparison, when the bilayers were composed of only DPhPC (LO_1, $\varphi_{SIL} = 0.60$ and $x_{POPC} = 0.00$), the initial increase in θ was much slower (e.g. $\theta = 30°$ was reached after approximately $6\,\mathrm{s}$), however the final equilibrium value θ_{DIB} was reached in only $\sim 500\,\mathrm{s}$ (Fig. 2.9b, cyan line).

We then 3D-printed networks using the lipid-oil compositions LO_{1-3} and compared the resulting droplet packing using our custom-made analysis script (section 2.3). Even though these conditions had the same θ_{DIB} of $36.3°$ (Table 2.1), we observed that networks printed at the LO_2 condition showed a significantly larger fraction of hexagonal packing (0.50 ± 0.07 area fraction), compared to both the conditions at higher x_{POPC} (LO_3, 0.28 ± 0.08 hexagonal area fraction) and no POPC (LO_1, 0.31 ± 0.05 hexagonal area fraction) (Fig. 2.9c, see Table 7.20 and 7.21 for statistical test).

Since the three conditions we compared were characterised by the same equilibrium $\theta_{DIB} = 36.3°$, we reasoned that the differences in hexagonal packing were caused by the differences in bilayer formation kinetics as observed in our droplet pair experiments (Fig. 2.9b), and in particular by the interaction between the kinetics of DIB formation and the frequency of droplet ejection in our 3D-printing process. As specified in section 2.3, for our study on the packing of droplets in droplet networks we 3D-printed constructs composed of $7 \times 8 \times 4$ droplets, generated at a standard droplet ejection frequency $t_{drop}^{-1} = 0.5\,\mathrm{s}^{-1}$. At this printing frequency, each new droplet is generated after a time interval $t_{drop} = 2\,\mathrm{s}$ from the previous droplet, while a

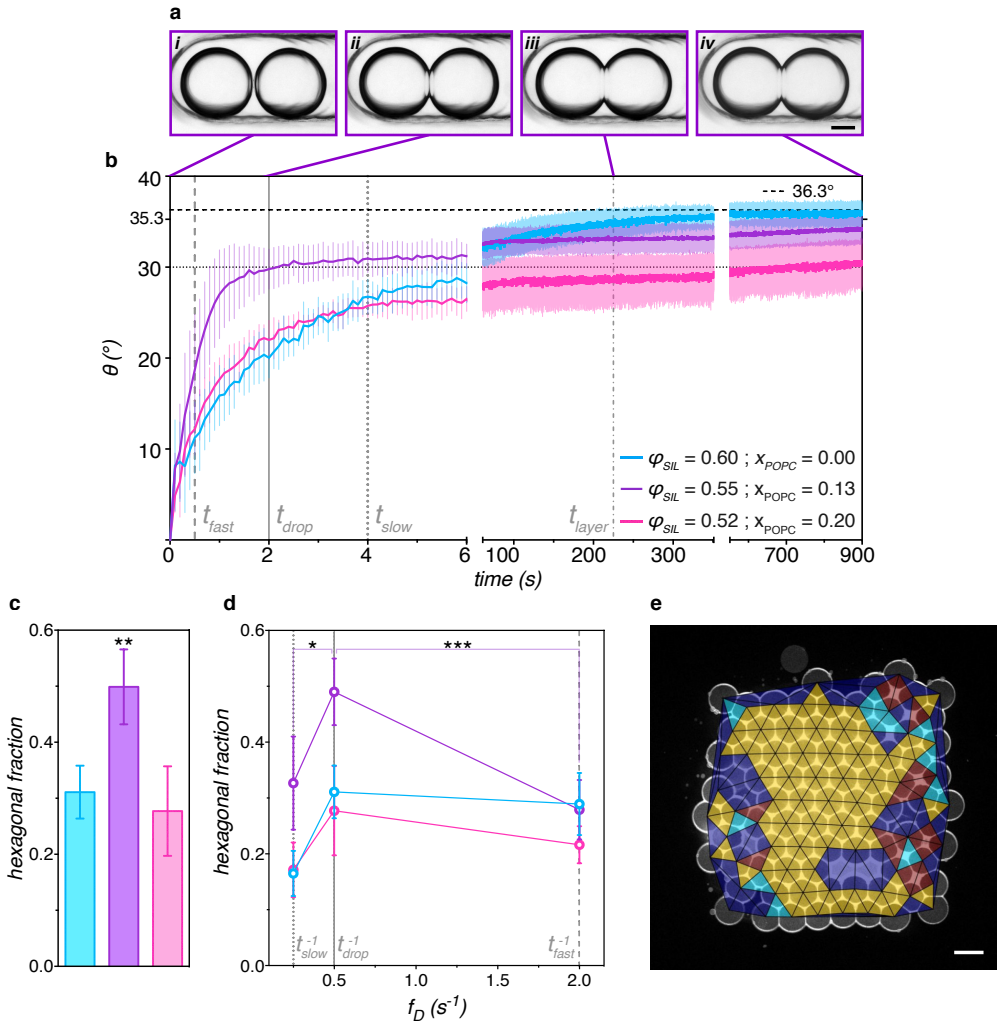

Fig. 2.9. Effect of the kinetics of DIB formation on the packing of droplets in 3D-printed networks. For all panels in this figure the lipid-oil conditions used are colour coded as follows: cyan — $\varphi_{SIL} = 0.60$ and $x_{POPC} = 0.00$, $\theta_{DIB} = 36.3°$ (LO_1); purple — $\varphi_{SIL} = 0.55$ and $x_{POPC} = 0.13$, $\theta_{DIB} = 36.3°$ (LO_2); magenta — $\varphi_{SIL} = 0.52$ and $x_{POPC} = 0.20$, $\theta_{DIB} = 36.3°$ (LO_3). Vertical dashed lines in **b** and **d** indicate characteristic times in our 3D-printing process: t_{fast} (0.5 s), t_{drop} (2 s), and t_{slow} (4 s) indicate time intervals between subsequent droplets when printing at a fast ($t^{-1}_{fast} = 2\,\mathrm{s}^{-1}$), standard ($t^{-1}_{drop} = 0.5\,\mathrm{s}^{-1}$), or slow ($t^{-1}_{slow} = 0.25\,\mathrm{s}^{-1}$) printing rates. t_{layer} indicates the time taken to print one layer composed of 7×8 droplets. **a**, Time-lapse brightfield imaging of DIB formation in a droplet pair (LO_2 condition). Snapshots taken at $t = 0$ s (*i*), $t = 2$ s (*ii*), $t = 225$ s (*iii*), and $t = 900$ s (*iv*). Scale bar: $150\,\mu$m. **b**, Plots of the non-equilibrium contact angle θ over time in droplet pairs formed at LO_{1-3} conditions. **c**, Hexagonal packing fractions in networks formed at LO_{1-3} conditions, printed at a droplet ejection frequency of $0.5\,\mathrm{s}^{-1}$. **d**, Comparison of the hexagonal packing fractions in networks (LO_{1-3} conditions) printed at fast ($t^{-1}_{fast} = 2\,\mathrm{s}^{-1}$), standard ($t^{-1}_{drop} = 0.5\,\mathrm{s}^{-1}$), and slow ($t^{-1}_{slow} = 0.25\,\mathrm{s}^{-1}$) printing rates. **e**, Fluorescent confocal image and overlay of the packing classification using Delaunay triangulation for a network printed at the LO_2 condition, showing large areas of regular hexagonal packing (yellow triangles). Scale bar: $100\,\mu$m.

7×8 droplet layer and a $7 \times 8 \times 4$ network are formed after approximately $225\,\mathrm{s}$ (t_{layer}) and $900\,\mathrm{s}$ (t_{print}), respectively. Interestingly, the time interval t_{drop} also corresponds to the time with which the non-equilibrium contact angle θ in droplet pairs reached $30°$ at the LO_2 condition (Fig. 2.9b), which exhibited a significantly larger fraction of hexagonal packing in printed networks, as shown in Fig. 2.9c.

We suggest that matching the DIB formation kinetics with the droplet ejection frequency during printing improved hexagonal packing, as observed from LO_2 (Fig. 2.9c). At this condition, by the time a new droplet was generated ($t_{drop} = 2\,\mathrm{s}$), the DIB at the previous droplet-droplet interface had reached a non-equilibrium $\theta \simeq 30°$, which would then slowly increase to reach the equilibrium value $\theta_{DIB} = 36.3°$ in a time interval longer than $t_{print} = 900\,\mathrm{s}$. During the formation of the first 7×8 droplet layer ($t < t_{layer} = 225\,\mathrm{s}$), each droplet-droplet interface would manifest a non-equilibrium contact angle θ between $30°$ and $33°$ (depending on the droplet positioning). Since a contact angle of $30°$ is optimal to form 2D hexagonal lattices of droplets (as discussed in section 2.2.1), we reason that this condition would maximise the lattice regularity of the first layer. The formation of an extended 2D hexagonal lattice in the first layer would then template the regular packing of droplets in the second and subsequent layers, promoting the formation of a regular hcp lattice throughout the 3D-printed network.

We confirmed that the matching of DIB formation kinetics and printing frequency lead to improved hexagonal packing by comparing the packing structures of 3D-printed networks generated at different droplet ejection frequencies (Fig. 2.9d). When printing within the same lipid-oil composition LO_2 at both faster ($t_{fast}^{-1} = 2\,\mathrm{s}^{-1}$) and slower ($t_{fast}^{-1} = 0.25\,\mathrm{s}^{-1}$) ejection rates, we observed significantly lower hexagonal packing fractions in 3D-printed networks (Fig. 2.9d, see Table 7.22 and 7.23).

Our experiments confirmed that we can 3D-print droplet networks with extended areas of regular hexagonal packing when 1) the equilibrium contact angle θ_{DIB} approximated the geometrically-derived critical angle $\theta_c = 35.3°$, and 2) the droplet ejection frequency was matched to the kinetics of DIB formation to allow the fast formation of a 2D hexagonal lattice in the first layer, from which an extended hcp lattice could develop.

2.6 Localisation and propagation of packing structures in droplet networks

The analysis method introduced in section 2.3 allowed to quantitatively compare the packing structures of droplet networks printed at a range of different conditions, and revealed the parameters that affect packing in 3D-printed constructs (see sections 2.4 and 2.5). Following on from our analysis, we were interested in investigating the localisation and propagation of packing structures in 3D-printed droplet networks.

We first studied whether the regular and irregular packing arrangements identified in section 2.3 localised in specific regions of the networks. We overlaid the fluorescent confocal images of the first layer of droplet networks printed at $\varphi_{SIL} = 0.55$ and $x_{POPC} = 0.13$ (LO_2, $n = 5$, Fig. 2.10a) and mapped the frequency of occurrence of the different packing motifs on an idealised map of the network (Fig. 2.10b, see chapter 6.3.9). Using this analysis, we could observe that regular hexagonal arrangements of droplets primarily localised at the centre of the networks (Fig. 2.10b*i*), while irregular arrangements were confined at the edges (Fig. 2.10b*iii-iv*). This effect could arise from the number of neighbours that droplets were able to coordinate to in different regions of the networks. Specifically, droplets located at the edge of the networks, coordinated to fewer than six other droplets (in the

first layer, Fig. 2.10c), were more likely to exhibit irregular arrangements (amorphous or no packing, Fig. 2.10b*iii-iv*). Conversely, droplets coordinated to six neighbouring droplets in the first layer were more likely to arrange in regular hexagonal lattices (Fig. 2.10b*i*).

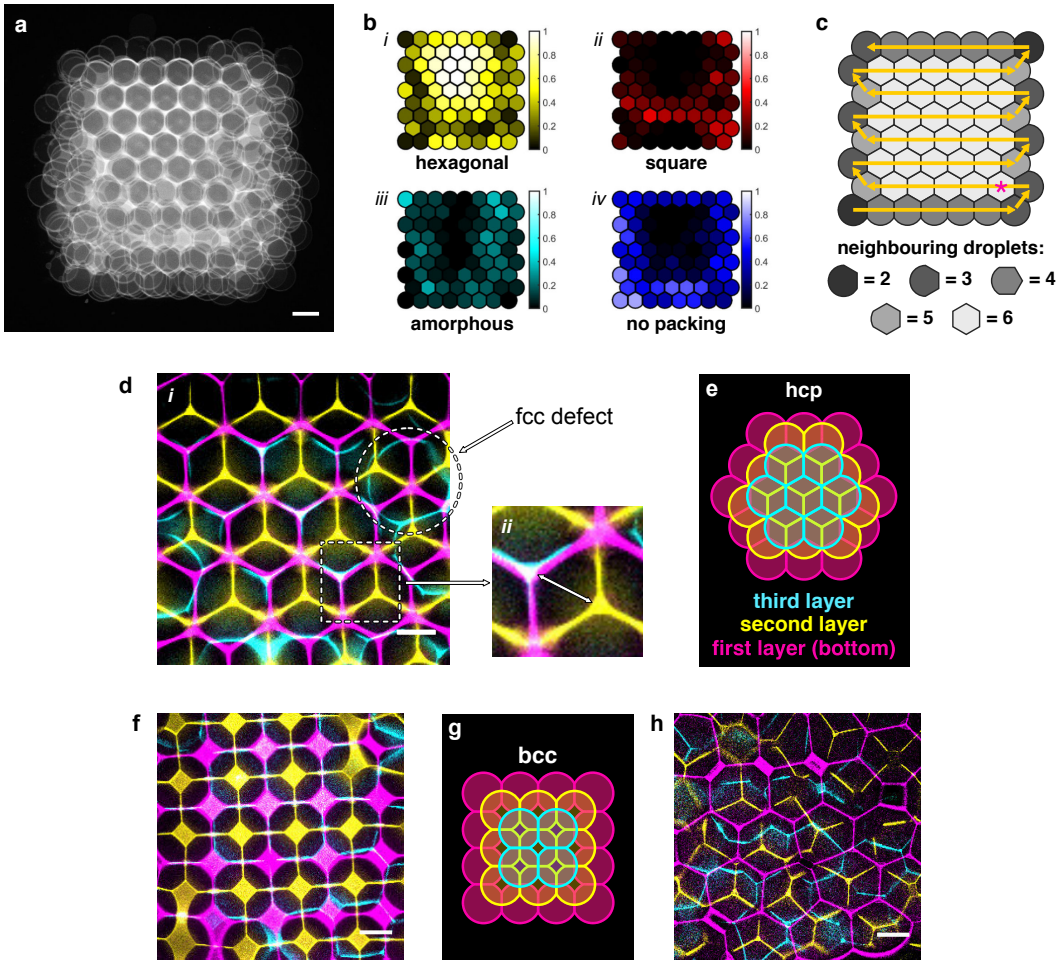

Fig. 2.10. Droplet packing arrangements localise in specific regions of the networks and propagate to the upper droplet layers. **a**, Overlaid fluorescent confocal images of the first layer of droplets in printed networks formed at $\varphi_{SIL} = 0.55$ and $x_{POPC} = 0.13$ (LO_2, $n = 5$). **b**, Heatmaps of the frequency of occurrence of hexagonal (*i*), square (*ii*), amorphous (*iii*) and no packing (*iv*) arrangements in different areas of the networks. **c**, Diagram of the droplet printing path of the first layer of a printed network (yellow arrow). Droplets are colour-coded based on the number of neighbours. Magenta star indicates the first droplet in the printing path coordinated to 6 neighbours. **d**, Overlaid confocal images of the bilayer network at the first (magenta), second (yellow) and third (cyan) layer of a droplet network packed in an hcp arrangement (*i*). Detail shows offset of layer 2 with respect to layer 1 and 3 (*ii*). **e**, Diagram of an hcp arrangement of droplets. **f**, Overlaid confocal microscopy images of the first (magenta), second (yellow) and third (cyan) layer of a droplet network packed in a bcc arrangement. **g**, Diagram of a bcc arrangement of droplets. **h**, Overlaid confocal microscopy images of the first (magenta), second (yellow) and third (cyan) layer of a droplet network packed in an amorphous arrangement.

Next, we investigated how packing arrangements of droplets in the first (bottom) layer of droplets affected the upper layers in 3D-printed networks. As discussed in section 2.3, we were able to acquire clear and complete images of the lipid bilayer networks of only the first layer of droplets, while the upper layers presented optical aberrations and distortions (Fig. 2.5b). Consequently, we based our systematic analysis of the droplet packing in 3D-printed networks on the confocal images of the first layer only. However, understanding how the packing of droplets in the first layer affects the upper layers is key to assessing the significance of our study.

We overlaid fluorescent confocal images of the first three droplet layers and observed that packing arrangements in the first (bottom) layer propagated to the upper layers of printed networks (Fig. 2.10d-h). Specifically, we found that when droplets in the bottom layer packed as a regular 2D hexagonal lattice, the droplets in the second and third layers also arranged hexagonally, forming a regular hcp lattice (Fig. 2.10d-e). As expected for hcp, the hexagonal droplet lattices in the first and third layers were aligned with respect to each other, while the hexagonal lattice at the second layer was offset by a centre-to-centre distance equal to the circumradius of a unit hexagon (see Fig. 2.10d*ii*). Rarely, we could also find droplets in the third layer that would be offset to both layer 1 and 2 (face-centred cubic arrangement, fcc, indicated in Fig. 2.10d*i*). Other packing arrangements also propagated to the upper layers of the networks. Square arrangements of droplets in the first layer propagated to the upper layers to form body-centred cubic lattices (Fig. 2.10f-g), and irregular arrangements also propagated to the upper layers to form amorphous 3D structures (Fig. 2.10h).

Our observations highlight the importance of the packing arrangement of droplets in the first layer of printed networks, which templates the three dimensional packing lattice of droplets throughout the structure. The propagation of droplet arrangements also reinforces our systematic packing analysis

of printed networks based on images of the first layer, confirming that the packing structure of the bottom layer of droplets provides a good representation of the 3D architecture of the network.

2.7 The polyhedral shape of tessellated droplets

When droplets pack in a 3D network, they deform and assume polyhedral shapes with faces that reflect the position of the lipid bilayers that interface them with their neighbours. Their final geometry depends on the equilibrium contact angle θ_{DIB}, the number of surrounding droplets and their positioning. For hcp, each droplet is surrounded by 12 neighbouring droplets and assumes the space-filling polyhedral geometry of a trapezo-rhombic dodecahedron[71] (D_{3h}, Fig. 2.11b*i*). In order to understand the local architecture of droplets in different regions of networks, and to further confirm the tessellation of droplets in regular hcp lattices, we aimed to resolve the polyhedral shape of droplets within printed networks.

2.7.1 Direct imaging of fluorescent droplets in a network and optical aberrations

We 3D-printed droplet networks composed of $10 \times 12 \times 4$ (x, y and z directions) aqueous droplets (PBS), with 3 fluorescent droplets within each layer (containing Atto488 water soluble fluorophore, Fig. 2.11a). We acquired horizontal cross-sections of each fluorescent droplet (z-stacks acquired by confocal microscopy) and reconstructed their 3D geometry[72] (using Imaris imaging software, Oxford Instruments, see chapter 6.3.6). As shown in Fig. 2.11b*ii-vi*, the reconstructed droplets suffered from optical aberrations,

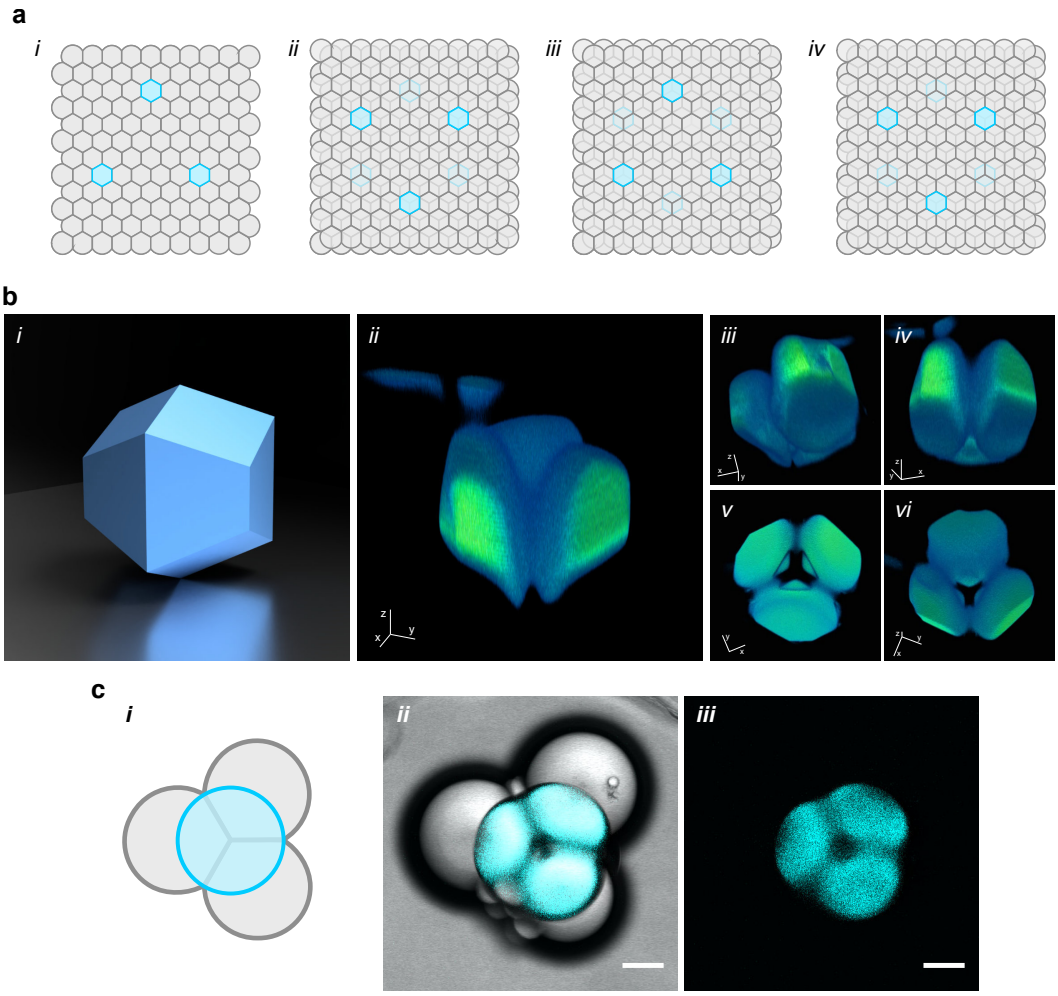

Fig. 2.11. Optical aberrations prevent the reconstruction of droplet geometry. **a**, Diagrams of the first (*i*), second (*ii*), third (*iii*) and fourth (*iv*) layers of a droplet network containing 3 fluorescent droplets ($10\,\mu$M Atto488) within each layer. **b**, Computer-generated model of a trapezo-rhombic dodecahedron (*i*, generated using Autodesk Fusion 360), the space-filling polyhedron of hcp lattices, and 3D reconstructions (from z-stack confocal images) of a fluorescent droplet at the second layer of a printed network (*ii-vi*). Imaging aberrations prevent the reconstruction of the polyhedral shape. **c**, Diagram (*i*), overlaid brightfield and epifluorescent microscopy images (*ii*), and epifluorescent microscopy image (*iii*) of a droplet containing a fluorophore ($10\,\mu$M Atto488) on top of a triplet of droplets, arranged as a tetrahedron. Similar artefacts are visible at the droplet-droplet interfaces and at the meeting point of the droplets positioned at the bottom layer. Scale bar: $150\,\mu$m.

which prevented us from resolving their 3D geometry. We reasoned that the observed optical aberrations were caused by the difference in refractive index of the aqueous ($\eta_{PBS} = 1.33$) and the oil ($\eta_{oil} = 1.42$) phases.

To confirm this, we imaged a fluorescent droplet (containing $10\,\mu$M Atto488) on top of a triplet of droplets, arranged in a tetrahedral arrangement (Fig.

2.11c). As shown in Fig. 2.11c*iii*, we observed imaging artefacts comparable to those found when imaging droplets embedded within networks. Therefore, we confirmed that the artefacts were caused by the diffraction of light at the bilayer interfaces, in particular at the meeting point in the middle of the three droplets in the bottom layer.

2.7.2 3D replicas of droplets confirm dodecahedral shape

In order to resolve the 3D geometry of tessellated droplets, we generated fluorescent poly(ethylene glycol) hydrogel replicas and dispersed them in aqueous solution (PBS) to minimise differences in refractive indices, and therefore minimising optical aberrations. This process allowed us to image and reconstruct their polyhedral shape (Fig. 2.12).

To generate the hydrogel replicas, we used a photo-crosslinkable pre-hydrogel solution consisting of poly(ethylene glycol) diacrylate monomer (PEGDA, mw 700, $20\,\mathrm{wt}\,\%$ in PBS), photo-initiator ($0.5\,\mathrm{wt}\,\%$ Irgacure 2959) and a photo-crosslinkable fluorophore ($100\,\mu\mathrm{M}$ ethidium bromide-*N,N'*-bisacrylamide). By applying the contact angle screening method described in section 2.1, we identified the lipid-oil condition that would allow us to maximise hcp packing of droplets composed of this pre-hydrogel solution ($\theta_{DIB} = 36.4°$, obtained at $\varphi_{SIL} = 0.59$ and $x_{POPC} = 0$, see Fig. 7.5 and Tab. 7.11 for linear regression and statistics).

We 3D-printed networks composed of the fluorescent pre-hydrogel solution (Fig. 2.12a*i*) and photo-crosslinked the PEGDA monomers within the droplets by UV radiation, forming networks of polyhedral hydrogel replicas that maintained the 3D geometry of the tessellated aqueous droplets[73] (Fig. 2.12a*ii*). We then dispersed the networks in PBS: during this process the networks

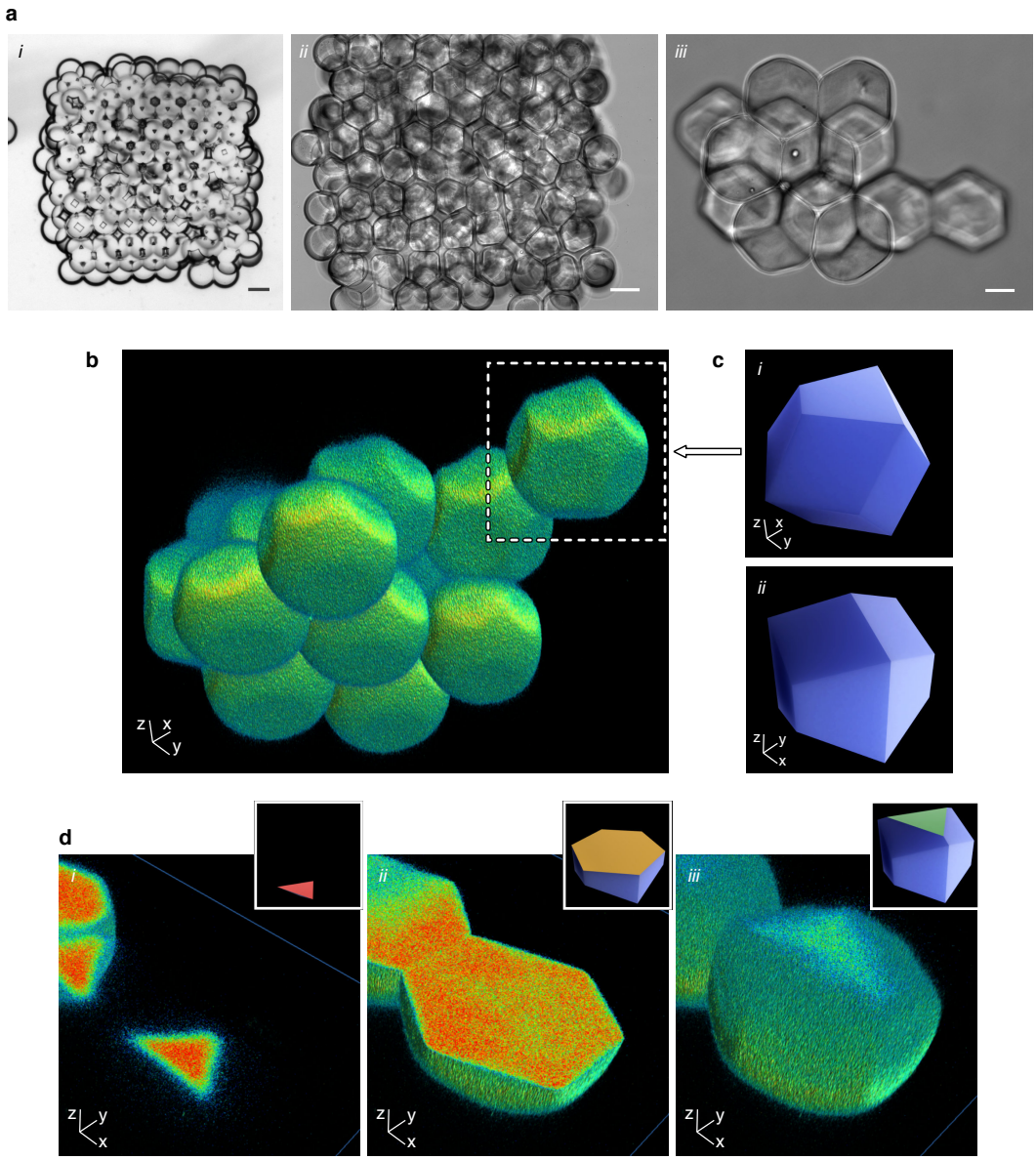

Fig. 2.12. Space-filling polyhedral geometry of tessellated droplets in printed networks. **a**, Brightfield microscopy images of a droplet network composed of a fluorescent photo-cross-linkable pre-hydrogel solution before (*i*) and after (*ii*) polymerisation with UV light. After transfer to aqueous buffer, the network breaks up in small clusters of hydrogel replicas, retaining the 3D geometry of tessellated droplets (*iii*). **b**, 3D reconstruction of the droplet cluster in **a***iii*, obtained by processing confocal slices (z-stacks) of the fluorescent hydrogel replica cluster using Imaris software (Oxford Instruments). **c**, Computer model of the space-filling polyhedron of hcp lattices, a trapezo-rhombic dodecahedron: view from below (*i*) and above (*ii*, generated with Autodesk Fusion 360). **d**, Digital cross-section of the highlighted droplet replica in **b**, demonstrating the same geometry as a trapezo-rhombic dodecahedron (insets are computer-generated models as reference).

broke apart into individual or small clusters of polyhedral hydrogel replicas (Fig. 2.12a*iii*).

We imaged the hydrogel replica clusters using confocal fluorescent microscopy (z-stack) and reconstructed their 3D geometry[72] (using Imaris imaging software, Oxford Instruments), obtaining a representation of the local architecture of tessellated droplets within printed networks (Fig. 2.12b and 7.8). We confirmed that droplets positioned in the second and third layer of hcp regions were surrounded by 12 neighbours, and assumed the space-filling polyhedral geometry of a trapezo-rhombic dodecahedron (D_{3h} symmetry) as expected for an hcp lattice (Fig. 2.12b-c). Horizontal cross-sections of the hydrogel replicas revealed a regular hexagon at their equator (Fig. 2.12d*ii*) and two aligned equilateral triangles at both the bottom and top (Fig. 2.12d*i* and *iii*, respectively). By comparison, the space-filling polyhedron of an fcc lattice — a rhombic dodecahedron[71] (O_h) — would show the same hexagonal cross-section at the equator, however its cross-sections at the top and

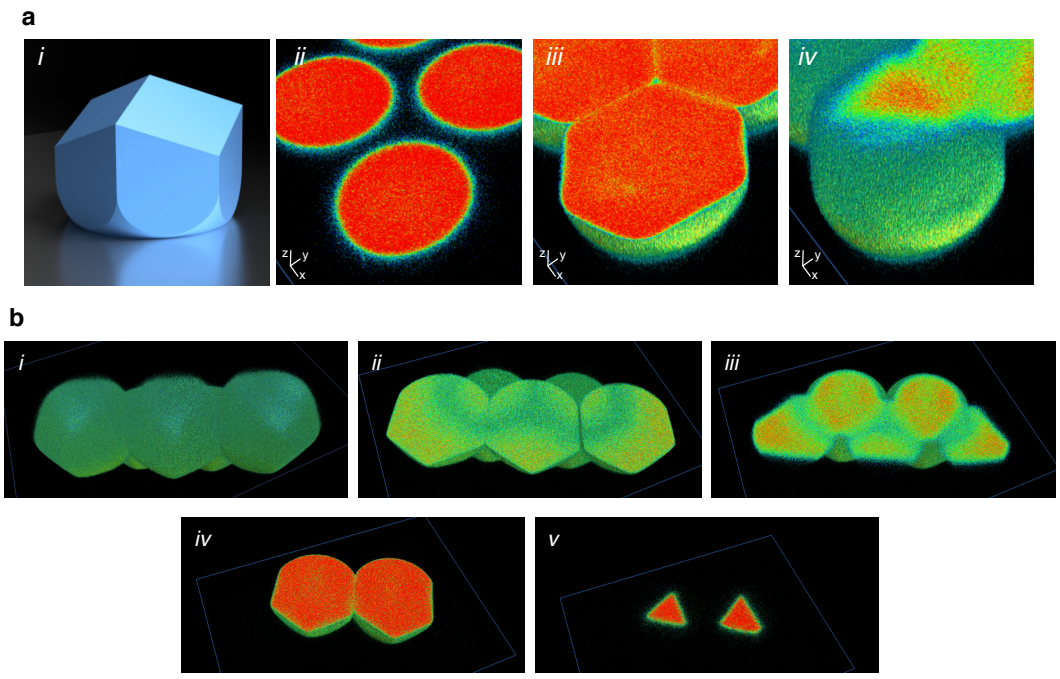

Fig. 2.13. Reconstruction of the 3D geometry of droplets at the bottom and top of networks. **a**, Computer model (*i*, generated using Autodesk Fusion 360) and horizontal cross-sections of a hydrogel replica positioned at the bottom of the networks (*ii-iv*), shaped as a 10-faced polyhedron with a flat circular face at the interface with the glass. **b**, Horizontal cross-sections at various heights of a hydrogel replica cluster highlighting the geometry of droplets positioned at the top and sides of a printed network, characterised by a curved face corresponding to the oil-water interface (*i-v*). 3D reconstructions of hydrogel replicas was performed with Imaris imaging software (Oxford Instruments) from confocal z-stack images.

bottom would describe equilateral triangles rotated by $60°$ with respect to each other.

With these experiments, we confirmed that tessellated droplets in printed network pack as regular hcp lattices, and assume the space-filling polyhedral geometry of a trapezo-rhombic dodecahedron. We could also resolve the 3D geometry of droplets positioned at the bottom and top of the networks. Hydrogel replicas of droplets positioned in contact with the printing substrate (quartz glass) were shaped as 10-faced polyhedra (C_{3v}), obtained as a truncated dodecahedron with a flat circular face at the interface with the glass (Fig. 2.13a). In contrast, droplets positioned on the top and sides of the networks formed incomplete dodecahedra with 10 or fewer faces, and presented curved surfaces corresponding to the water-oil interfaces (Fig. 2.13b).

2.8 Fabrication of synthetic tissues with single-droplet-wide features

Our study on the parameters that affect droplet packing allowed us to achieve highly regular 3D-printed droplet networks. We applied our findings to the fabrication of functional synthetic tissues with features patterned with single-droplet precision (Fig. 2.14).

As discussed at the beginning of this chapter, the complex functions performed by biological tissues derive not only by the cell types that populate the tissue, but most importantly by the specific architecture in which cells are positioned within the tissue. To mimic the structural cooperation of cells in biological tissues, we designed a synthetic tissue whose correct functionality would directly emerge from the precise positioning of droplets within it. Specifically,

we designed a 3D-printed network of dimensions $11 \times 11 \times 5$ droplets (x, y and z directions), featuring two single-droplet-wide pathways, which spanned the construct at different heights: one at the bottom of the network (within layer 1, Fig. 2.14a*i*), connecting A to C (Fig. 2.14b), and one at the top (within layer 5, Fig. 2.14a*v*), connecting B to D (Fig. 2.14b). The two single-droplet-wide conductive pathways were electrically conductive, due to permeabilisation of the lipid bilayers with the protein pore α-hemolysin[10,26] (αHL), and they were electrically isolated from each other by only three insulating droplet layers.

Consequently, the correct functionality of this synthetic tissue would directly emerge from the regular packing of droplets forming both the single-droplet-wide pathways and the insulating layers: imperfections in the lattice would lead to either interruption of the electrical communication along one of the two conductive pathways, or cross-talk between the two pathways designed as distinct (see equivalent electric circuit in Fig. 2.14c*ii*).

To fabricate the proposed synthetic tissue, we used an aqueous solution containing a high concentration of sodium chloride ($1\,\mathrm{M}$ NaCl in $25\,\mathrm{mM}$ Tris-HCl, pH 7.6). This choice was made to ensure sufficient charged species in solution to carry a detectable ionic current through the droplet pathways. Using the method described in section 2.1, we determined the composition of the lipid-oil solution to achieve optimal packing ($\varphi_{SIL} = 0.43$ and $x_{POPC} = 0$, $\theta_{DIB} = 35.4° > \theta_c$, Fig. 7.5, Tab. 7.35 for linear regression) of droplets of this aqueous composition. The droplets forming the conductive pathways consisted of the same aqueous solution, with the addition of αHL (at a concentration of $60\,\mu\mathrm{g\,mL^{-1}}$), together with a water soluble fluorophore for visualisation ($10\,\mu\mathrm{M}$ Atto488).

As shown in Fig. 2.14d, we fabricated the proposed synthetic tissue and visually assessed the integrity of the single-droplet-wide droplet pathway

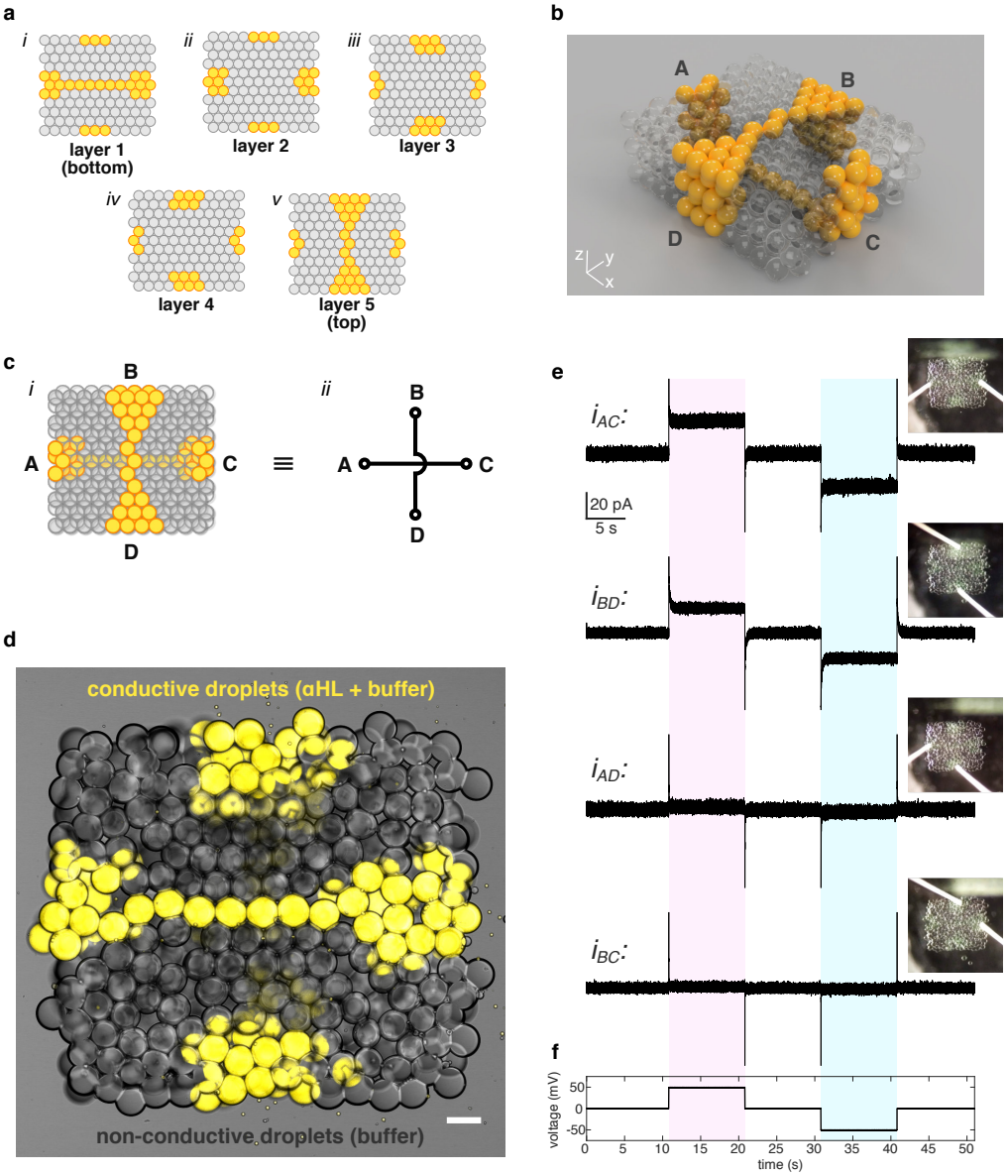

Fig. 2.14. Functional features with single-droplet resolution in synthetic tissues. **a**, Printing maps of the first (*i*), second (*ii*), third (*iii*), fourth (*iv*) and fifth (*v*) layer of a 3D-printed synthetic tissue with single-droplet-wide conductive pathways (in yellow). **b**, Computer 3D model displaying the architecture of the designed synthetic tissue: two single-droplet-wide conductive pathways span the network at different layers of the printed construct, one through the bottom layer, connecting A to C, and one through the top layer, connecting B to D. **c**, Simplified diagram of the synthetic tissue (*i*) and equivalent circuit model (*ii*). **d**, Overlaid brightfield and fluorescent confocal microscopy image of the synthetic tissue with single-droplet-wide conductive pathways. Lipid bilayers separating the droplets in the conductive pathway are permeabilised by addition of the protein pore α-hemolysin (αHL, $60\,\mu\mathrm{g\,mL^{-1}}$), allowing the flow of an ionic current upon application of a local potential. **e-f**, Electrical recordings of the ionic currents selectively flowing through the synthetic tissue. Upon application of the same potential protocol (**f**), we could detect ionic currents flowing from A to C (i_{AC}) and from B to D (i_{BD}), while no current was detected between A and D (i_{AD}) or B and C (i_{BC}) (**e**).

positioned at the bottom of the construct by confocal microscopy. Due to the imaging limitations discussed earlier (section 2.7.1), we could not resolve the geometry of the conductive droplet pathway positioned at the top of the construct. Interestingly, droplets containing αHL displayed a smaller contact angle θ_{DIB} compared to the surrounding insulating droplets. This decrease in θ_{DIB} was likely due to changes in surface tension of the lipid bilayers and monolayers upon interaction with the protein αHL. However, the regular packing of neighbouring droplets (at the centre of the construct in Fig. 2.14d), for which $\theta_{DIB} \simeq \theta_c$, constrained the single line of αHL-containing droplets to an hcp lattice, resulting in the precise positioning and continuity of the single-droplet-wide pathway.

We confirmed the correct functionality of the designed synthetic tissue through electrical recordings. Upon application of a potential protocol of $\pm 50\,\mathrm{mV}$ (Fig. 2.14f), we could record ionic currents flowing through the single-droplet-wide pathways connecting A to C (i_{AC}) and B to D (i_{BD}) (Fig. 2.14e). Conversely, no ionic current could be detected when we applied the same potential protocol between A and D (i_{AD}) or between B and C (i_{BC}) (Fig. 2.14e).

These results confirm the integrity of both single-droplet-wide conductive pathways positioned at the bottom and the top of the construct, as well as their structural and functional separation, in accordance with our design. Irregularities in the packing due to either low adhesive energy among the droplets (when $\theta_{DIB} \ll \theta_c$, Fig. 2.6a*i* and b*i*) or lattice distortions (when $\theta_{DIB} \gg \theta_c$, Fig. 2.6a*v* and b*v*) would result in either interruption of the electrical signal in one or both the conductive pathways, or cross-talk between the two pathways designed as distinct. By applying our improved control over the packing of droplets in 3D-printed networks ($\theta_{DIB} \simeq \theta_c$), we demonstrated that we can now fabricate synthetic tissues with single-droplet resolution

($100\,\mu\mathrm{m}$ diameter, $\sim 524\,\mathrm{pL}$ voxel volume) in three dimensions using our droplet-based 3D-printer.

2.9 Conclusions

In summary, we demonstrated how we can easily modulate the equilibrium contact angle θ_{DIB} in a DIB pair, how θ_{DIB} controls the packing of hundreds of droplets in 3D-printed droplet networks, and how controlled packing of droplets allows us to fabricate synthetic tissues with single-droplet resolution.

Specifically, we showed that θ_{DIB} is a key geometrical parameter in DIB pairs, which results from the balance of forces and surface energies in the system. We demonstrated that we can easily tune and predict θ_{DIB} by varying the oil (φ_{SIL}) and lipid (x_{POPC}) composition (Fig. 2.2). This represents a crucial finding not only for printed networks, but for any DIB-based system in which control over the bilayer area (e.g. to precisely control membrane protein concentration or diffusion of molecules between the compartments) or over the geometry of small droplet clusters is desirable.

We then demonstrated how θ_{DIB} directs the packing structure of hundreds of droplets in 3D-printed networks. To this end, we developed an image analysis software that allowed us to automatically classify and quantify packing arrangements and defects in 3D-printed droplet networks (Fig. 2.5). Through this analysis, we experimentally proved that, when θ_{DIB} approximated the geometrically-derived critical contact angle $\theta_c = 35.3°$ (section 2.2.2), droplets in printed networks packed highly regularly according to an hcp lattice (Fig. 2.6).

Due to the dynamic nature of the printing process, which ejects and positions droplets one-by-one, line-by-line and layer-by-layer, we also observed that the kinetics of DIB formation impacted the final packing arrangements in droplet networks. We obtained the largest fraction of hcp when the droplet ejection frequency was matched to the kinetics of DIB formation to allow the fast formation of a 2D hexagonal lattice in the first layer, from which an extended hcp lattice could develop (Fig. 2.9).

In addition, we observed that packing arrangements tended to localise in specific areas of the networks: regular hexagonal packing localised at the centre of the printed constructs, while irregular droplet arrangements were confined at the edges (Fig. 2.10a-b). We also found that regular droplet arrangements in the bottom layer of the networks propagated to the upper layers to form regular 3D lattices (Fig. 2.10d-h). This observation stressed the importance of achieving regular arrangement of droplets in the bottom layer, because this templated the three dimensional packing of droplets throughout the printed network.

By generating hydrogel replicas of droplets, we could inspect the local 3D architecture of small clusters of tessellated droplets within printed networks. We resolved the polyhedral geometry of tessellated droplets, and confirmed that they assumed the shape of trapezo-rhombic dodecahedra, the space-filling polyhedra corresponding to an hcp lattice (Fig. 2.12).

Lastly, we applied our improved control over the packing of droplets in 3D-printed networks to the fabrication of a high-resolution synthetic tissue. We printed a synthetic tissue in which two single-droplet-wide conductive pathways ($\sim 100\,\mu\mathrm{m}$ in diameter) were patterned in 3D with a minimal separation of three insulating droplet layers ($\sim 300\,\mu\mathrm{m}$ separation), with no cross-talk between the conductive pathways (Fig. 2.14).

The results presented in this chapter demonstrate that we can now build synthetic tissues with features patterned at single-droplet resolution using an automated and readily scalable fabrication technology. Our findings, based on geometric and thermodynamic variables such as θ_{DIB}, are also applicable to any other system in which adhesive deformable spheres are patterned to form 3D-printed structures.

3

Hierarchical assembly of 3D-printed droplet networks

3D-printed droplet networks are a powerful platform to build tissue-like materials, synthetic tissues and biological tissue models at high resolution.[20,26,31] However, similarly to other additive manufacturing technologies, one of the main limitations of fabricating synthetic tissues by 3D-printing is the slow build rates of the process.[74] In our printing, we typically build sub-mm-sized constructs by depositing hundreds of droplets with diameter between $50\,\mu\mathrm{m}$ and $150\,\mu\mathrm{m}$, at a droplet ejection frequency of $0.5\,\mathrm{s}^{-1}$ (equivalent to 1 droplet every $2\,\mathrm{s}$). As discussed in chapter 2.5, at this printing rate we can build droplet networks composed of $7 \times 8 \times 4$ droplets (x, y and z directions) in approximately 15 minutes, generating constructs of linear dimensions of approximately $600 \times 600 \times 300\ \mu\mathrm{m}$. Although the current fabrication technique allows us to build small biomimetic devices and tissue models at high resolution and with high reproducibility, the fabrication of large, cm-sized synthetic tissues is still limited.

A possible strategy to improve the build rates is to increase the droplet ejection rate during the printing process. However, as discussed in chapter 2.5, in our 3D-printing process the best results are achieved when the droplet

ejection rate and the kinetics of DIB formation are matched. An increase in droplet ejection frequency is usually associated with increased printing defects and loss of printing resolution and fidelity (Fig. 2.9). An alternative strategy to increase the fabrication speed while retaining the high resolution and fidelity of the printed constructs is to parallelise the printing process, by individually printing sub-mm- or mm-sized constructs and assembling them to form higher order constructs.

In this chapter, we explore the ability to build large functional synthetic tissues by assembling 3D-printed constructs fabricated individually. This assembly method opens the way for designing synthetic tissues with modular components that can be fabricated in parallel – potentially in series – and combined in different ways to achieve different overall outputs, in a similar fashion to discrete components in electronic systems. Additionally, we also explore the "healing" properties of assembled synthetic tissues, such as the ability of a functional construct to regain functionality after being severed and re-assembled.

3.1 Assembly of functional 3D-printed constructs

We first tested the ability to obtain simple functional constructs by assembling 3D-printed building blocks fabricated independently. As in chapter 2.8, we limited our preliminary investigations to synthetic tissues that were able to conduct an ionic current through a specific droplet pathway within them. This was obtained by patterning two types of aqueous solutions, one containing α-hemolysin (αHL, final protein concentration $60\,\mu\mathrm{g\,mL^{-1}}$, plus $10\,\mu\mathrm{M}$ Atto488 fluorescent dye for visualisation, in an aqueous solution composed of $25\,\mathrm{mM}$ Tris-HCl buffer pH 7.6 and $1\,\mathrm{M}$ NaCl) and one composed of buffer solution

only ($25\,\mathrm{mM}$ Tris-HCl buffer pH 7.6 and $1\,\mathrm{M}$ NaCl). The building blocks consisted of simple 3D-printed constructs (of dimensions $8 \times 9 \times 4$ droplets in x, y and z directions) containing a 3-droplet-wide conductive pathway spanning the network (Fig. 3.1a,b).

In order to assemble building blocks into higher order structures, we needed to optimise the manipulation and assembly method. We assessed various means of manual manipulation, for example by using plastic pipette tips, glass rods, gravity (i.e. tilting the printing container) and flat metal spatulas. In accordance to what discussed in chapter 6.3.4, we observed that networks printed on hydrophilic quartz glass (O_2 plasma treatment) presented a strong interaction with the substrate, which made them more difficult to move without deforming or fracturing. As a consequence, we fabricated all the networks presented in this chapter on untreated glass surfaces: on this substrate, the networks readily detached from the surface under the application of a gentle mechanical force, with minimal deformation or rupture.

To demonstrate the feasibility of the proposed method to obtain large droplet networks, we manually manipulated and assembled all the presented constructs using a flat metal spatula. However, we also investigated more readily scalable and automatable techniques. For instance, we explored the possibility of encapsulating paramagnetic particles (MagneHis™ Ni paramagnetic particles, Promega) in the buffer droplets and moving the printed networks using a magnetic field, as shown before for large nanolitre-sized droplets.[24] When dispersed into bulk aqueous solution, the particles quickly sedimented at the bottom of the tube, resulting in an uneven distribution between hand-made droplets made from the same bulk solution (Fig. 7.9). This was further enhanced when we attempted to print the aqueous buffer loaded with the particles: they sedimented to the nozzle tip and their concentration within subsequently ejected droplets dropped significantly (not shown). Furthermore, when we attempted to move DIBs formed with a pair of hand-made

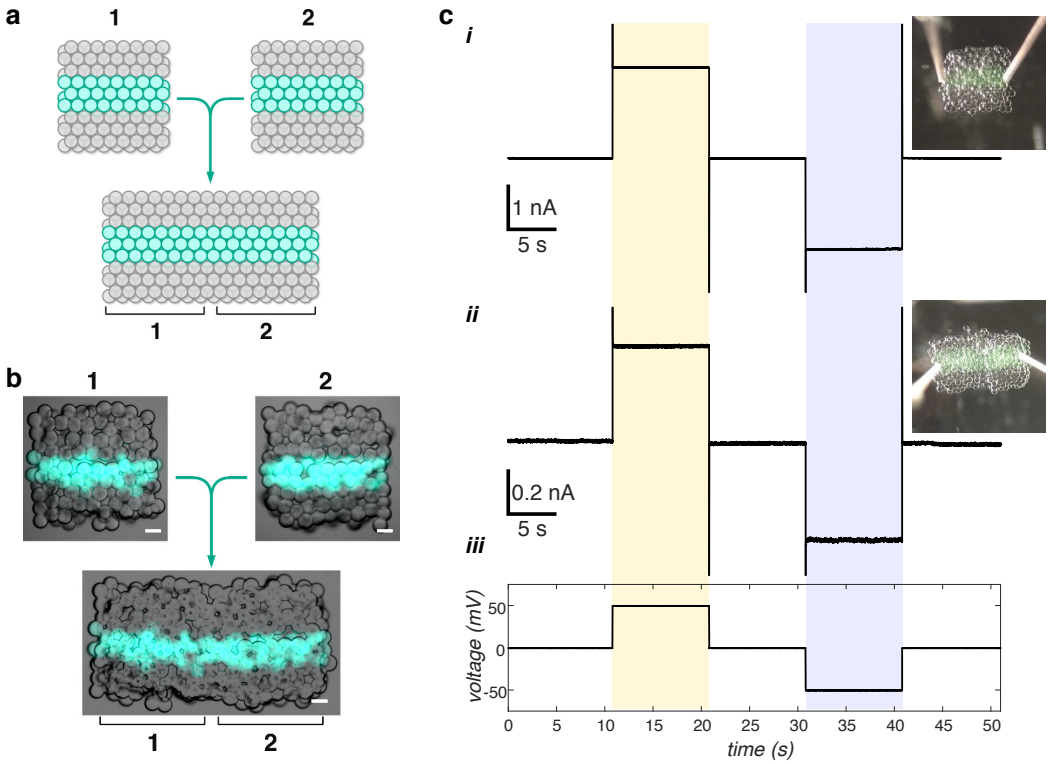

Fig. 3.1. Assembly of 3D-printed building blocks into functional constructs. **a**, Assembly diagram of a construct obtained by joining two identical 3D-printed building blocks with a conductive pathway (teal droplets). **b**, Composite bright-field and fluorescent images of the two building blocks before assembly (top) and of the final assembled construct (bottom). The 3D-printed building blocks consisted of identical $8 \times 9 \times 4$ droplet networks with a 3-droplet-wide conductive pathway (containing α-hemolysin, αHL, and Atto488 fluorescent dye for visualisation, coloured in teal) spanning the networks from left to right. **c**, Electrophysiological recording of the ionic current flowing through one 3D-printed building block (***i***) and the final assembled construct (***ii***), upon the application of the same voltage protocol of $\pm 50\,\mathrm{mV}$ (***iii***). Scale bars: $100\,\mu\mathrm{m}$.

droplets by applying a magnetic force (using a stack of $5\,\mathrm{mm}^3$ neodymium magnets, E-Magnets UK), we observed that some beads localised at the lipid bilayer interface, eventually rupturing the DIB and leading to coalescence (Fig. 7.9). We considered that using of a hydrogel (e.g. agarose) in the non-conductive droplets might increase the sedimentation time during printing, as a result of the higher density and viscosity of the melted agarose, as well as constraining the magnetic particles away from the lipid bilayer once the gel has been crosslinked. However, we decided to initially investigate the properties of higher-order assemblies of droplet networks using the simplest experimental setup: we 3D-printed building blocks composed of aqueous

droplets with conductive pathways (containing αHL) which we assembled manually using a metal spatula.

We first assembled a simple construct obtained by joining two identical $8\times9\times4$ droplet networks (in x, y and z directions, equivalent to linear dimensions of approximately $700\times700\times300\,\mu\mathrm{m}$) with a 3-droplet-wide conductive pathway (containing αHL) spanning the networks from left to right (see diagram in Fig. 3.1a). We added a water soluble fluorescent dye (Atto488, $10\,\mu\mathrm{M}$) in the αHL-containing droplets as a visual guide for manipulation and alignment. As seen in Fig. 3.1b, we successfully aligned the conductive droplet pathways patterned within the two building blocks, obtaining an assembled construct with an interconnected conductive pathway of double the length of the unit building blocks (approximately $1.4\,\mathrm{mm}$ in length).

We then assessed the ability of the assembled construct to selectively conduct an electrical signal within the αHL-containing droplet pathway through electrophysiological analysis. We first measured the ionic current flowing through the conductive pathway of an individual building block upon application of a potential of $\pm50\,\mathrm{mV}$ (Fig. 3.1c*iii*) and recorded a change in current of $+(2031\pm40)\,\mathrm{pA}$ and -$(2049\pm37)\,\mathrm{pA}$ at positive and negative potential, respectively (Fig. 3.1c*i*). After joining the two networks, we recorded an ionic current of $+(423\pm28)\,\mathrm{pA}$ and -$(442\pm26)\,\mathrm{pA}$, upon application of the same potential protocol of $\pm50\,\mathrm{mV}$ (Fig. 3.1c*ii*). Importantly, when we applied the potential outside the conductive droplet pathway (i.e. when one or both of the electrodes were in contact with non-conductive droplets) we did not detect any ionic current flowing through the network (Fig. 7.11).

With this experiment, we demonstrated the possibility of building functional synthetic tissues by assembling 3D-printed building blocks manufactured individually.

3.2 Assembly of larger functional constructs

Next, we wanted to assess the ability to assemble centimetre-sized functional constructs by joining multiple 3D-printed building blocks (Fig. 3.2a). We successfully assembled up to 7 networks ensuring the alignment of the conductive pathways (Fig. 3.2b). The resulting assembled construct measured approximately $6\,\mathrm{mm}$ in length and was composed of thousands of droplets (2016 droplets), with a conductive pathway approximately $200\,\mu\mathrm{m}$ wide. Networks that were manually moved over long distances showed increased signs of deformation and rearrangements of the droplets within them (see networks on the right in Fig. 3.2b). Although this deformation did not preclude the assembly of a functional construct, further optimisation of the manipulation process will be required to allow for the fabrication of more complex and larger structures.

We characterised the electrical properties of the 7-network-long construct. Upon application of a potential of $\pm 50\,\mathrm{mV}$, we recorded a change in ionic current of $+(84 \pm 20)\,\mathrm{pA}$ and -$(83 \pm 19)\,\mathrm{pA}$, respectively (Fig. 3.2c). By comparing the electrical recordings performed on constructs composed of 1, 2, 3 and 7 networks, we observed a rapid decay of the steady-state ionic current flowing through the conductive droplet pathways with increasing number of assembled networks (Fig. 3.2d). This result is in accordance with previous observations by Holden *et al.* for chains of nanolitre-sized droplets.[10]

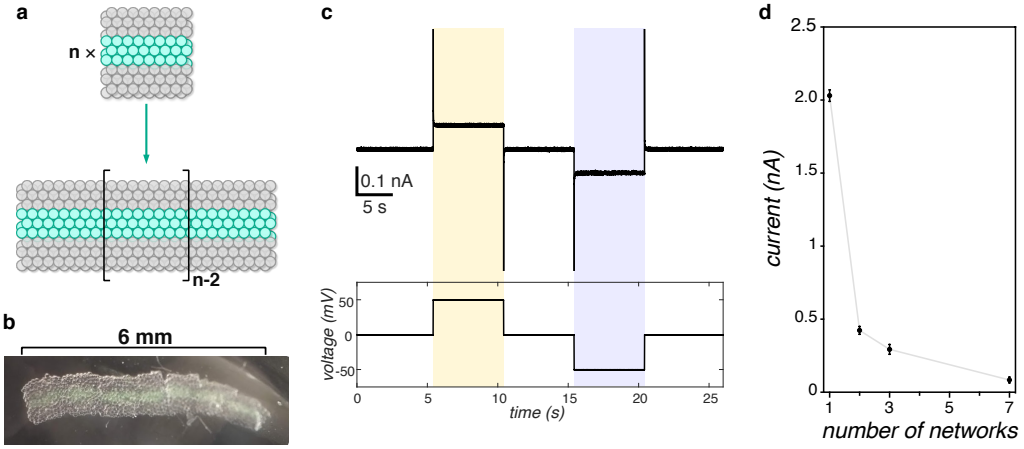

Fig. 3.2. Assembly of larger functional constructs to transmit electrical signals over long distances. **a**, Conceptual diagram of the formation of larger functional constructs by sequential addition of identical unit building blocks. **b**, Optical microscopy image of the 7-network-long assembled construct featuring an interconnected conductive pathway of approximately $6\,\mathrm{mm}$ in length and $200\,\mu\mathrm{m}$ in thickness. **c**, Electrophysiological recording of the ionic current flowing through the conductive pathway of the construct in **b**, demonstrating the transmission of an electrical signal over long distances by assembly of multiple sub-mm-sized 3D-printed networks with aligned conductive pathways. **d**, Dependency of the steady-state ionic current (positive change upon application of a potential of $+50\,\mathrm{mV}$) on the number of assembled building blocks. We observed a rapid decay with the number of interconnected networks, similar to previous observations on chains of nanolitre-sized droplets by Holden and collegues.[10]

3.3 Example of modular assembly

After demonstrating the validity of our suggested assembly method to fabricate larger functional constructs, we aimed to show a simple example of modular assembly of 3D-printed synthetic tissues. Modular engineered systems, like discrete components in electronic circuits, are composed of a limited number of standardised components (e.g. resistor, capacitor, transistor, diodes, etc.) that the designer of a specific device can assemble in different ways to obtain different outputs.[75,76] In our system, we could design various standardised building blocks with specific architectures and compositions, and therefore specific functions, that we could subsequently assemble in specific ways to obtain a desired output. The functionality of these building blocks does not have to be the conduction of ionic currents as in our

preliminary example presented here, but could also involve chemical[15–18] (chain of compartmentalised reactions), biochemical[19,20] (compartmentalised enzymes and other biological molecules) or biological[31] (interconnection of 3D-printed tissue models to build *in-vitro* organ models) components.

We exemplified the modular assembly of synthetic tissues by assembling groups of three building blocks (with the same design as in sections 3.1 and 3.2) in different ways to obtain different outputs. By assembling three building blocks in a way that aligned their conductive pathways, we could build a synthetic tissue that exhibited the behaviour of a closed electrical switch (Fig. 3.3a). Conversely, by assembling the same building blocks in a way that the conductive pathway of the central component was orthogonal to

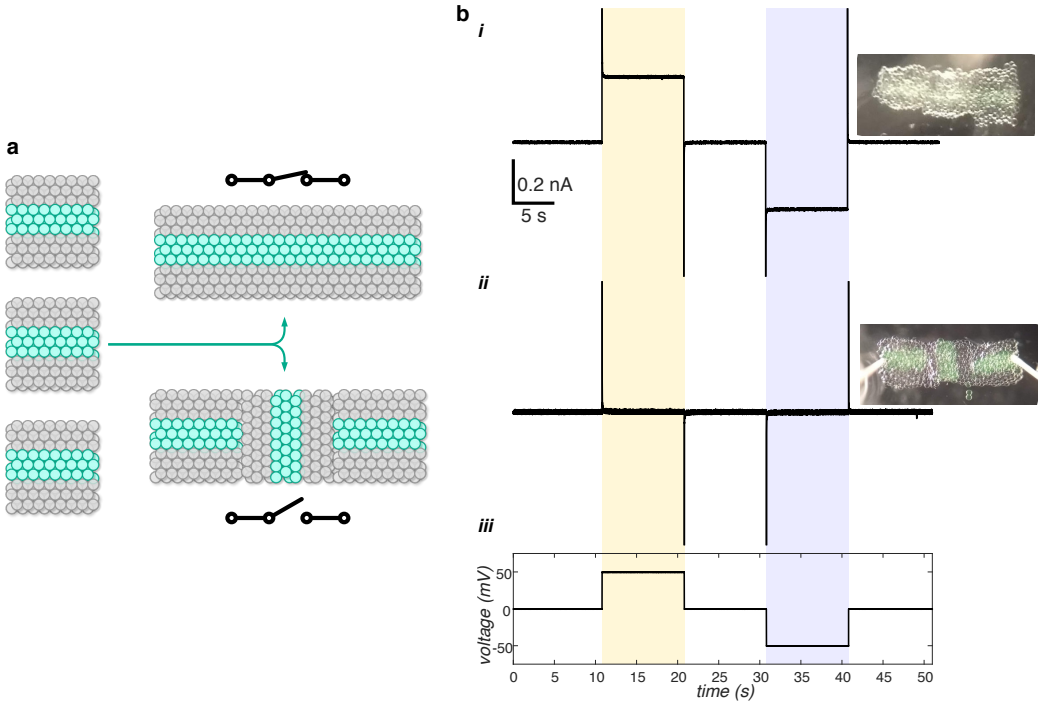

Fig. 3.3. Modularity of assembled constructs. **a**, Conceptual diagram of the modular assembly of two constructs composed of the same unit building blocks (left), but with different final electrical properties. By changing the orientation of the central building block during assembly, it is possible to obtain the electrical behaviour of a closed switch (top-right) or an open switch (bottom-right). **b**, Electrophysiological recordings of the ionic current flowing through the synthetic tissue designed as a closed switch (***i***), and as an open switch (***ii***), upon application of the same voltage protocol (***iii***).

the other two, we could obtain a synthetic tissue with the electrical behaviour of an open switch.

We investigated the electrical behaviour of the assembled synthetic tissues. By applying a potential protocol of $\pm 50\,\mathrm{mV}$ (Fig. 3.3b*iii*), we recorded an ionic current flowing through the construct assembled as a closed state switch ($+(293 \pm 34)\,\mathrm{pA}$ and $-(301 \pm 33)\,\mathrm{pA}$ current changes for positive and negative potential, respectively)(Fig. 3.3b*i*). Conversely, we detected no significant change of current when we applied the same potential protocol to the construct designed as a switch in its open state ($+(3 \pm 25)\,\mathrm{pA}$ and $-(2 \pm 24)\,\mathrm{pA}$ current changes for positive and negative potential, respectively)(Fig. 3.3b*ii*).

3.4 Assembled constructs show "healing" properties

The vast majority of biological tissues have the ability to heal, i.e. to fully or partially recover their original structure and physiological function after an injury. Healing represents a fundamental evolutionary step found in living organisms, which allows for increased longevity and adaptability to changes in the environment,[77] and which has attracted the attention of many in the field of smart and biomimetic materials.[78] In the design of synthetic tissues we aim to mimic specific functionalities of biological tissues and to take inspiration from the strategies that complex life has evolved to design devices with non-biomimetic functionalities. Consequently, we were interested in investigating the ability of assembled droplet networks and synthetic tissues to recover their initial functionality after an injury.

Similarly to the previous examples in this chapter, we exemplified the healing ability of assembled synthetic tissues containing a conductive droplet pathway. In particular, we assembled a construct composed of two 3D-printed networks, with aligned conductive pathways. Next, we caused an injury by cutting the assembled construct with the same flat spatula used for the manipulation of the building blocks. Lastly, we re-assembled the two parts of the fractured constructs (Fig. 3.4a). At each step of this process we assessed the electrical properties of the intact, fractured and "healed" synthetic tissue.

We applied a voltage protocol of $\pm 50\,\mathrm{mV}$ (Fig. 3.4b*iv*) to the ends of the conductive pathway in the intact assembled construct, and recorded an ionic

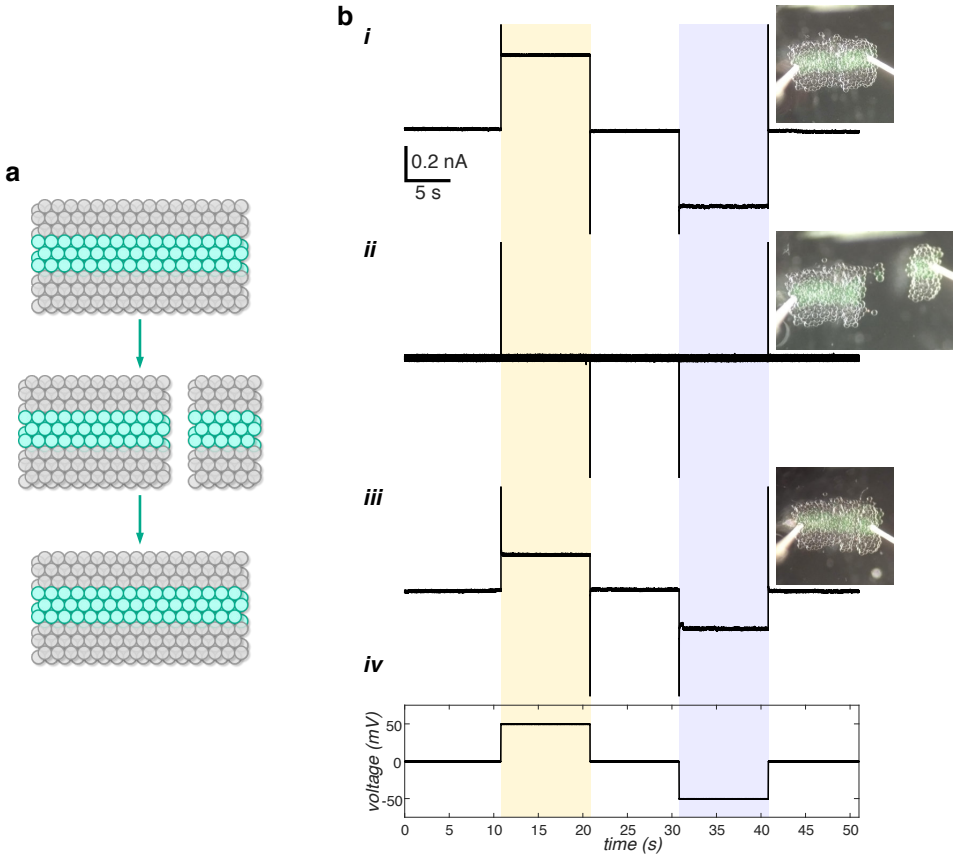

Fig. 3.4. "Healing" properties of assembled synthetic tissues. **a**, Conceptual diagram of the assembled (top), fractured (middle) and "healed" synthetic tissue. **b**, Electrophysiological recording of the ionic current flowing through the assembled construct before injury (***i***), after being severed with a metal spatula (***ii***), and after being re-assembled (***iii***), upon application of the same voltage protocol (***iv***). The re-assembled construct recovered the ability to conduct an ionic current, confirming the ability of synthetic tissues to "heal" after injury.

current of $+(423 \pm 28)\,\mathrm{pA}$ and $-(442 \pm 26)\,\mathrm{pA}$, at positive and negative potential respectively (Fig. 3.4b*i*). After fracture, no significant current flow was detected ($+(0.7 \pm 3.4)\,\mathrm{pA}$ and $-(0.6 \pm 3.4)\,\mathrm{pA}$ current changes for positive and negative potential, respectively)(Fig. 3.4b*ii*). When the fractured synthetic tissue was re-assembled, its ability to conduct a current was recovered. Specifically, upon application of the same potential protocol, we recorded changes in ionic currents of $+(207 \pm 24)\,\mathrm{pA}$ and $-(215 \pm 25)\,\mathrm{pA}$ for positive and negative potential, respectively. Notably, the ionic current flowing through the construct after re-assembly was lower than before the injury, indicating that the "healing" process was only partial, similar to several cases of biological healing.[77]

Since the conductivity of a droplet network is proportional to the available area through which charged species can flow, we attributed the observed drop in conductivity of the "healed" synthetic tissue to a decrease in the cross-sectional area of the conductive droplet pathway after re-assembly. This observation also highlights how, similarly to conventional electrical circuits, assembled networks are affected by a loss in conductivity once an electrical contact is introduced in the circuit (known as contact resistance).[79] In conventional electrical contacts, surface roughness, partial oxidation and absorption of water vapour and atmospheric contaminants usually lead to a reduced effective surface of contact at the interface between two conductive elements, which in turn causes a measurable drop in conductivity at the electrical joint.[79] In our system, contact resistance at the interface between two joined networks may arise from the lower number of conductive droplets at their interface, caused by rearrangement of droplets during manipulation and by printing defects at the edges of each 3D-printed building block (Chapter 2.6). As a consequence, we expect the conductance of an assembled construct to be lower compared to a single printed network of identical dimensions. However, additional experiments will be needed to fully characterise the electrical and mechanical properties of assembled constructs.

3.5 Conclusions

Through the presented experiments, we confirmed that larger functional synthetic tissues can be assembled from sub-mm-sized 3D-printed building blocks fabricated independently. The assembly of these components is modular, and the final functionality of the assembled construct depends on both the design of the individual building blocks, and their positioning with respect to each other. In addition, assembled synthetic tissues show "healing" properties, and recover their initial functionalities after injury.

Despite its simplified approach, this work opens the way to more complex applications of assembly, modularity and recovery after injury in synthetic tissues. In future experiments, we will aim to assemble cm-sized synthetic tissues that can transmit electrical signals over long distances. Additionally, we will explore the assembly of building blocks of various shapes and with more intricate conductive pathways (e.g. curved and branching).

Of great interest is the ability to not only assemble printed networks in 2D (i.e. on the plane of the printing substrate), but also to extend this method to 3D assembly (i.e. stacking of networks in the z direction). To this end, a more controlled, reliable and automatable method of manipulation and assembly has to be developed. A range of technologies compatible with handling of picolitre- and nanolitre-sized aqueous volumes will be tested, including magnetic handling,[24] acoustic tweezers,[80] and electro-wetting.[81]

As discussed earlier, we attempted to encapsulate magnetic particles within the aqueous droplets forming the non-conductive part of the 3D-printed building blocks. However, we could not achieve consistent distribution of particles within droplets throughout the printing process. The magnetic particles quickly sedimented towards the nozzle opening, which resulted in a high concentration of particles in the first few ejected droplets, and a rapid

drop in concentration in subsequent droplets ejected within minutes. During preliminary experiments performed on pairs of nanolitre-sized droplets, we observed localisation of magnetic particles at the bilayer interface. This event weakened the lipid bilayer and eventually led to coalescence of the droplet pair during prolonged sessions of manipulation.

We intend to improve both the uneven distribution of magnetic particles and droplet coalescence by encapsulating the particles within hydrogel droplets (e.g. agarose). We suggest that the higher density and viscosity of the melted agarose solution will slow down the sedimentation time, allowing for a more uniform distribution of particles throughout the printing session. Periodic re-suspension of the particles (e.g. by applying a magnetic field towards the top and side of the printing nozzle) could also be investigated. Once printed, the hydrogel within the droplets will be gelated, trapping the magnetic particles within it and preventing them from interacting with the lipid bilayers. This approach should ensure improved stability of the printed structures containing magnetic particles. Another possible strategy is to use large droplets or hydrogel blocks[82] loaded with magnetic particles as carriers: these carriers will be temporarily connected to a building block during manipulation, and then detached once the block has reached the intended final position.

After optimisation of the manipulation and assembly of 3D-printed synthetic tissues, we will further explore the ability to assemble constructs with modular parts. First, we will focus on developing a range of soft devices with interesting electrical properties, expanding from the examples found in literature using nanolitre-sized droplets and a range of membrane proteins, such as rectifiers,[13] bio-batteries,[10] light sensors,[10,83] and logic gates.[14] Next, we will explore the ability to assemble modular compartmentalised microreactors, in which complex multi-step chemical and biochemical reactions can be performed.[38,57] For example, we could design a modular system that

produces different outputs (i.e. final product) depending on the type of inputs (i.e. constructs containing reaction substrates) and processing units (i.e. architecture and sequence of compartmentalised enzymatic reactions) assembled in the specific construct. In addition, different modules could be assembled at specific time-points to achieve precise spatio-temporal control over the performed reactions.

We will also further investigate the "healing" properties of the assembled synthetic tissues from a range of mechanical stresses, such as compression, shear, flexion, and torque. Importantly, the ability of synthetic tissues to recover from mechanical stress could be exploited for controlled assembly and disassembly of constructs, as an additional way to control modular micro-reactors.

Acknowledgement of collaboration: the experiments presented in this chapter were performed in collaboration with Gabriella Kimmerly as part of her rotation project during Trinity term 2019.

4

Interfacing 3D-printed droplet networks with aqueous environments

Droplet networks represent a versatile platform that can be customised for several applications by compartmentalising a range of molecules and reactions and by functionalising the lipid membranes with membrane proteins. Some of the most exciting long-term applications involve interfacing these synthetic systems with living cells and tissues, in order to monitor, control or complement their biological activity. However, droplet networks are formed within a bulk oil phase (Fig. 4.1a), which is not readily compatible with physiological aqueous environments. Previous efforts in interfacing droplet networks with an external aqueous bulk phase have culminated in the development of multisomes[32,33] and multi-compartment liposomes.[34]

Multisomes consist of double emulsions (water in oil in water, w/o/w) where aqueous droplets are formed within an oil droplet containing lipids, which is in turn immersed in an aqueous bulk phase (Fig. 4.1b). The aqueous compartments within multisomes are separated from each other and from the bulk aqueous solution by lipid bilayers, and can be generated by hand[32] or by microfluidics.[33] Usually, these systems are composed of only a few (up to 4) nanolitre-sized droplets, with no ability to achieve precise patterning.

Only one example shows multisomes composed of hundreds to thousands of picolitre-sized internal compartments, fabricated using our droplet 3D-printer.[26] However, these constructs could only be formed by suspending the oil droplet on a metal or plastic loop, from which the multisomes could not be detached.

Multi-compartment liposomes are formed from w/o/w double emulsions, from which the oil phase is completely removed, obtaining nanolitre-sized compartments separated from each other and from the external aqueous solution by lipid bilayers[34,37] (Fig. 4.1c). These can be formed from DIBs by phase transfer through a water-oil interface in the presence of lipids,[37] or from microfluidic-generated multisomes through dewetting of the oil phase

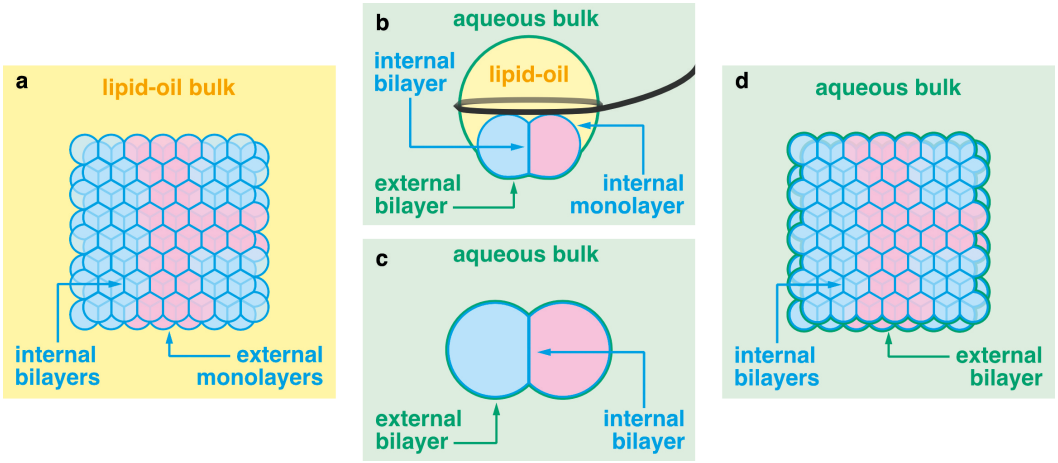

Fig. 4.1. Transfer of 3D-printed droplet networks to aqueous environment. **a**, Diagram of a 3D-printed droplet interface bilayer network in oil bulk phase. The patterned aqueous compartments are separated by lipid bilayers, while a lipid monolayer forms at the interface with the oil phase. **b**, Diagram of a multisome, consisting of a w/o/w double emulsion system in which aqueous droplets are formed within an oil droplet containing lipids, which is in turn immersed in an aqueous bulk phase. Lipid bilayers form at the droplet-droplet and droplet-aqueous bulk interfaces. These structures are usually supported by a metal wire loop, but can also be generated by microfluidics. **c**, Diagram of a multi-compartment liposome, consisting of aqueous compartments separated from each other and from the aqueous solution by lipid bilayers. These structures can be formed by phase transferring a droplet pair through an oil-water interface in the presence of lipids, or by dewetting the oil phase from a multisome. **d**, Diagram of a 3D-printed droplet interface bilayer network transferred to aqueous environment. Our strategy aims to form a lipid bilayer at the interface between the printed construct and the aqueous bulk, while retaining the patterning of droplets and the functionality of the lipid bilayers within the networks.

and formation of a lipid bilayer around the aqueous compartments.[34] The dewetting of the oil phase from these structures is driven by controlling the interfacial tension between the external aqueous phase and the oil ($W_{OUT}-O$) and between the internal and external aqueous phases ($W_{IN} - W_{OUT}$) by the addition of a surfactant (e.g. tri-block copolymer Pluronic F68). Using this technique, multi-compartment liposomes of up to 30 compartments have been generated.[34] However, multi-compartment liposomes fabricated using both techniques suffer from low yield (43% for the phase transfer method and 62% for the dewetting method), low reproducibility, low versatility (only specific combinations of materials can be used), and inability to precisely control the positioning of each compartment.[34,37]

In this chapter, we explore the transfer of 3D-printed droplet networks and synthetic tissues to aqueous phase, a fundamental step towards the application of these constructs in physiological environments. To achieve this goal, control over the interfacial energies is key to drive the formation of a lipid bilayer at the interface between the droplet network (W_{IN}) and the external aqueous solution (W_{OUT}) (Fig. 4.1d). Similarly to the formation of multi-compartment liposomes,[34] we lower the surface energy at the $W_{OUT}-O$ interface by the addition of small amounts of tri-block copolymer Pluronic F68. Importantly, our proposed method involves minimal changes to the upstream fabrication process of the droplet networks, and therefore ensures the highest versatility and applicability to the examples of droplet networks and synthetic tissues currently published in the field. Using this method, we demonstrate the transfer of droplet pairs and 3D-printed droplet networks to aqueous environment, by forming a functional lipid bilayer at the $W_{IN}-W_{OUT}$ interface and by retaining the architecture and the functionality of the internal lipid bilayers.

4.1 Transfer of droplet pairs to aqueous environment

We first tested the proposed phase transfer method on pairs of nanolitre-sized droplets (W_{IN}, $10-20$ wt % poly(ethylene glycol) mw 4000, PEG_{4k}, in PBS, $50-150$ nL volume) made by hand using the standard DIB formation protocol (chapter 6.3.3) in a lipid-oil mixture with $\varphi_{SIL} = 0.65$ and $x_{POPC} = 0.33$. After formation, we transferred the droplet pairs by sinking them through a lipid monolayer at an oil-water interface ($O-W_{OUT}$) with low surface energy ($0.5-2$ wt % F68 in PBS) (Fig. 4.2a). We encapsulated PEG_{4k} molecules within the droplets in order to provide enough weight to overcome the tension of the oil-water interface, similarly to previous examples in literature where multi-compartment liposomes were formed by phase transferring droplet pairs through an oil-water interface under gravity.[37] The dewetting of the oil from the structure is driven by addition of the block copolymer F68 (Fig. 4.2b) in the W_{OUT} phase: the amphiphilic nature of the molecule and the short length of the hydrophobic core lowers the surface tension of the external leaflet of the external lipid bilayer, while preventing the formation of non-specific polymeric pores.[84]

During our early experiments, we observed that droplet pairs during phase transfer to aqueous media were particularly sensitive to osmotic stress, and that balancing osmolarity was key in achieving successful transfer. For example, when we attempted to transfer droplet pairs composed of an aqueous solution with a high concentration of solutes (20 wt % PEG_{4k} in PBS) to an external aqueous phase at a lower solute concentration (5 wt % F68 in PBS), we observed swelling of the droplets, usually resulting in the rupture of one or both of the transferred droplets (Fig. 7.10). Even though we did not achieve transfer of intact droplet pairs at this condition, the swelling of droplets indicated the formation of a semi-permeable membrane at the

W_{IN}-W_{OUT} interface, with behaviour comparable to a lipid bilayer. We attempted to balance the osmolarities of the two aqueous phases by simply using equal monomer concentrations of PEG_{4k} in W_{IN} and F68 in W_{OUT}. For example, we tested aqueous droplet pairs composed of $20\,\mathrm{wt}\,\%$ PEG_{4k} in PBS (W_{IN}) in combination with a W_{OUT} phase composed of $10\,\mathrm{wt}\,\%$ F68 in PBS (Fig. 4.2c). Although the tri-block copolymer F68 is composed of both PEG and poly(propylene glycol) (PPG) monomers (Fig. 4.2b), we observed that balancing the total monomer concentrations of PEG_{4k} and F68 was indeed sufficient to balance the osmolarities of the two solutions: no swelling was

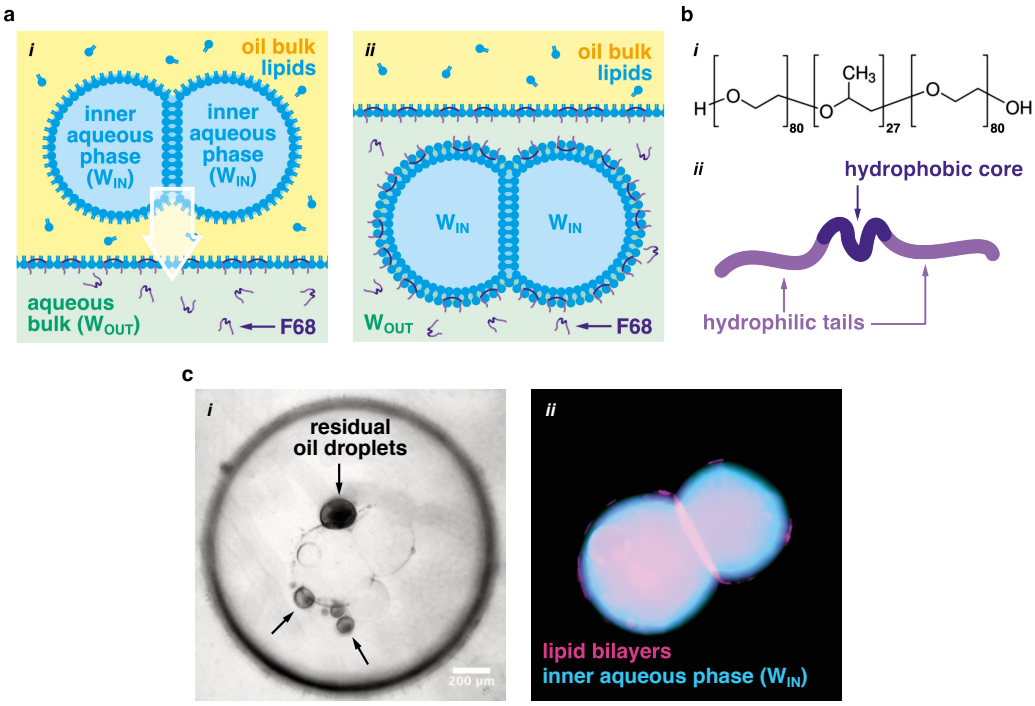

Fig. 4.2. Formation of multi-compartment liposomes by transfer of droplet pairs to aqueous environment. **a**, A droplet pair is formed in a lipid-oil solution (*i*) and allowed to sink through an oil-lipid-water interface under gravity (*ii*). The formation of the external lipid bilayer is driven by the tri-block copolymer Pluronic F68, which lowers the surface tension of the oil-water interface. **b**, Structure (*i*) and cartoon representation (*ii*) of the block copolymer Pluronic F68. The amphiphilic nature of the molecule and the short length of the hydrophobic core lowers the surface tension of the external leaflet of the external lipid bilayer, while preventing the formation of non-specific polymeric pores.[84] **c**, Brightfield (*i*) and fluorescent (*ii*) images of a multi-compartment liposome. Residual oil at the liposome interface collects over time into small oil droplets visible in (*i*). The aqueous compartments of the multi-compartment liposome are labelled with a water soluble dye ($10\,\mu\mathrm{M}$ calcein, in cyan), while lipid bilayers are labelled with a dye with high affinity for lipid bilayers ($10\,\mu\mathrm{M}$ sulforhodamine 101, in magenta) (*ii*).

observed and complete transfer of the hand-made droplet pairs was achieved (Fig. 4.2c).

In successfully transferred droplet pairs, we observed that the residual oil present on the surface slowly collected into small droplets within 1 hour (Fig. 4.2c*i*). Depending on the conditions used, these droplets would eventually detach from the multi-compartment liposomes and float towards the surface due to the lower density of the oil compared to the W_{OUT} solution. Similar mechanisms of residual oil removal have been reported in literature for comparable transfer methods.[34,37,85] We confirmed that our transfer method preserved the compartmentalisation of the aqueous compartments by observing that a water-soluble fluorescent dye (calcein) was successfully retained within the aqueous compartments after transfer (Fig. 4.2c*ii*). By encapsulating a water-soluble dye with high affinity for amphiphilic interfaces[68] (sulforhodamine-101) in the W_{IN} solution, we also observed the presence of a lipid bilayers at the interface between the internal aqueous compartments, as well as at the interface with the external aqueous phase (Fig. 4.2c*ii*).

With these experiments, we validated the feasibility of the proposed transfer method in droplet pairs. We achieved results similar to those reported in literature on the formation of multi-compartment liposomes with nanolitre-sized internal aqueous compartments.[34,37] To apply this method to the formation of structurally defined synthetic tissues that can function in aqueous environment, we focused our attention to the transfer of 3D-printed constructs.

4.2 Transfer of 3D-printed droplet networks to aqueous environment

3D-printed droplet networks are fabricated on a solid (typically glass or acrylic plastic) surface.[9,20,26,31] During fabrication, picolitre-sized droplets are ejected one by one and deposited line-by-line and layer-by-layer, to form three dimensional compartmentalised structures stabilised by droplet interface bilayers. As discussed in chapter 6.3.4 (Fig. 7.7), the printing surface plays a key role in the stabilisation of the growing printed structure, allowing the fabrication of precisely patterned droplet networks and synthetic tissues. Additionally, as discussed at the beginning of this chapter, we aim to minimise changes to the upstream fabrication process of the printed networks, in order to ensure the maximal flexibility and applicability of our phase transfer method to examples previously reported in the field.

We consequently 3D-printed networks of picolitre-sized droplets composed of W_{IN} solution ($10.5\,\mathrm{wt}\,\%$ PEG_{4k} in PBS), following the standard methodology developed in our group (see chapter 6.3.4). After printing, we pipetted four microlitre-sized droplets (usually $1\,\mu\mathrm{L}$ each) of W_{OUT} solution ($5\,\mathrm{wt}\,\%$ F68 in PBS) and positioned them in contact with the four sides of the square printed network (see Fig. 4.3a*i* for diagram and Fig. 4.3b*i* for microscopy images). Within minutes, the large W_{OUT} droplets started to adhere to the printed aqueous network, dewetting the oil from its surface (Fig. 4.3a*ii* and Fig. 4.3b*ii-iv*), until the oil phase was completely displaced (Fig. 4.3a*iii* and Fig. 4.3b*v*). Depending on the lipid-oil mixture used and particularly on the concentration of copolymer F68 in the external aqueous phase, this process took from 1-$2\,\mathrm{h}$ down to 20-$30\,\mathrm{min}$. As seen in Fig. 4.3b, the large W_{OUT} droplets also formed bilayers between each other. However, both leaflets of these bilayers contained F68, which made them weak and prone to coalescence. This effect facilitated the transfer of 3D-printed droplet networks

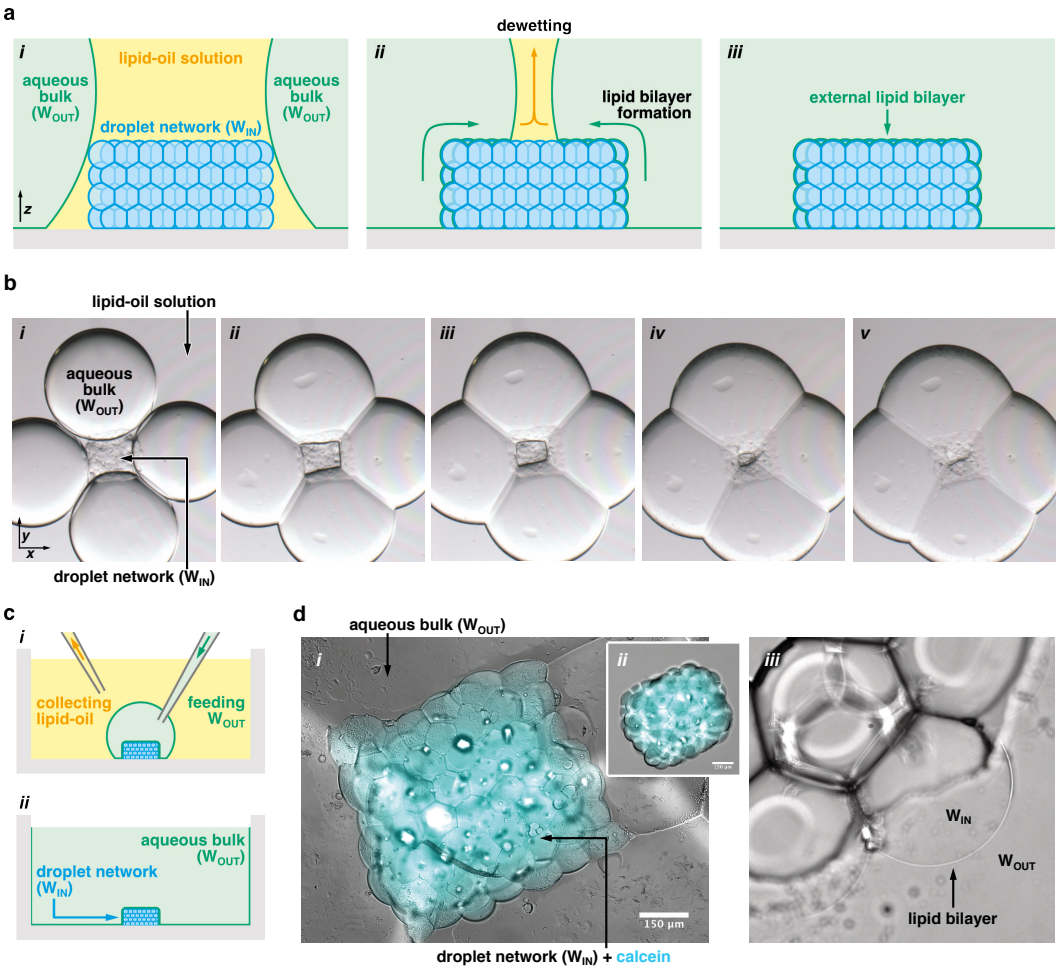

Fig. 4.3. Surfactant-assisted transfer of 3D-printed droplet networks to aqueous environment. **a**, Diagram of the surfactant-assisted transfer of 3D-printed droplet networks. After a droplet network is 3D-printed in a lipid-oil bath according to the usual protocol, large aqueous droplets, containing F68, are put in contact with the network (*i*). A lipid bilayer is formed at the interface between the droplet network (composed of the inner aqueous phase W_{IN}) and the external aqueous phase (W_{OUT}), while the oil phase is pushed away through a dewetting process (*ii*). After complete dewetting of the oil phase, the network is immersed into the external aqueous bulk phase W_{OUT}, with a functional lipid bilayer at the interface between W_{IN} and W_{OUT} (*iii*). **b**, Brightfield microscopy images of a 3D-printed droplet network during the phase transfer process. Four large aqueous droplets are put in contact with the network (*i*) and slowly wet the 3D-printed network (*ii-iv*), expelling completely the oil phase within 30 minutes (*v*). **c**, After transfer, the printed network is encapsulated in a large aqueous droplet composed of W_{OUT} solution (*i*). If needed, additional W_{OUT} solution can be fed into the encapsulating droplet to fill the printing cuvette, while the bulk oil can be removed (*ii*). **d**, Brightfield and fluorescent microscopy image of a networks transferred to aqueous environment. A water soluble fluorophore (calcein, in cyan) can be encapsulated within the printed network (*i*), demonstrating that the transfer process from the oil bulk phase (*ii*) ensures compartmentalisation of the inner aqueous phase W_{IN} from the external aqueous solutions W_{OUT}. The interface between W_{IN} and W_{OUT} has similar optical properties compared to large and giant unilamellar vescicles[86] (LUVs and GUVs) (*iii*).

to a bulk aqueous environment: after complete dewetting of the oil, the W_{OUT} droplets coalesced with each other, but importantly not with the W_{IN} droplets, resulting in a 3D-printed network encapsulated in one much larger aqueous droplet (Fig. 4.3c*i*). Once transfer was complete, the volume of the W_{OUT} droplet was adjusted to fit the application. When large bulk volumes of W_{OUT} solution were needed, additional W_{OUT} solution could be fed inside the external droplet, while collecting the excess lipid-oil solution from the top of the printing container, until the printing container was completely filled with W_{OUT} solution (typically $600\,\mu$L) (Fig. 4.3c*ii*). Alternatively, when reduced volumes of external aqueous solution were preferable (e.g. when using expensive reagents and purified proteins), smaller volumes (typically 10-$20\,\mu$L) of W_{OUT} solution could be fed into the W_{OUT} droplet, and experiments were performed with this setup, as in Fig. 4.3c*i*.

We assessed the ability of our transfer method to preserve compartmentalisation of solutes within the network. Similarly to our assessment with droplet pairs, we encapsulated a water-soluble dye ($10\,\mu$M calcein) within a droplet network (W_{IN}, $10.5\,\mathrm{wt}\,\%$ PEG_{4k} in PBS), which was then transferred to an external aqueous phase (W_{OUT}, $5\,\mathrm{wt}\,\%$ F68 in PBS). We successfully transferred the 3D-printed network maintaining the compartmentalisation of the fluorescent dye (Fig. 4.3d*i*), providing additional evidence that our method does not form unspecific pores at the interface between the internal (W_{IN}) and external(W_{OUT}) aqueous phases. Moreover, we observed that the interface between the internal and external aqueous phases resembled the appearance of lipid bilayers compartmentalising large and giant unilamellar vesicles[86] (LUVs and GUVs) (Fig. 4.3d*iii*).

4.3 Chemical sensing of ions in solution

After laying the foundation of our proposed transfer method and confirming its feasibility, we tested the functionality of the lipid bilayer at the $W_{IN}-W_{OUT}$ interface. To this end, we designed a synthetic tissue that could sense the presence of calcium ions (Ca^{2+}) in the surrounding aqueous environment.

As shown in Fig. 4.4a, we encapsulated a calcium indicator dye (high affinity rhod-dextran, mw 10,000, ThermoFisher) within a droplet network (W_{IN}, $25\,\mathrm{mM}$ Tris-HCl buffer pH 7.6, $10.5\,\mathrm{wt}\,\%$ PEG_{4k}, $150\,\mathrm{mM}$ NaCl, $10\,\mathrm{mM}$ EDTA and $30\,\mu\mathrm{g\,mL^{-1}}$ α-hemolysin, αHL). We then transferred the resulting synthetic tissue to an aqueous bulk solution containing the block copolymer F68 and without the calcium indicator dye (W_{OUT}, $25\,\mathrm{mM}$ Tris-HCl buffer pH 7.6, $8.4\,\mathrm{wt}\,\%$ PEG_{4k}, $1\,\mathrm{wt}\,\%$ F68, $150\,\mathrm{mM}$ NaCl, $10\,\mathrm{mM}$ EDTA and $30\,\mu\mathrm{g\,mL^{-1}}$ αHL). After transfer, calcium chloride ($CaCl_2$) was added to the external solution at a final concentration of $75\,\mathrm{mM}$. Within minutes, the calcium diffused through the protein pores inserted in the external and internal lipid bilayers of the synthetic tissue, increasing the fluorescence of the indicator dye (Fig. 4.4b). We could track the diffusion of calcium from the edges towards the centre of the synthetic tissue in real time (Fig. 4.4b*i-iv*). Notably, the droplets positioned closer to the source of calcium (i.e. the position at which calcium chloride was pipetted, bottom left corner in Fig. 4.4b*i*) detected the presence of calcium earlier than the droplets located at the opposite side (Fig. 4.4b*ii,iii*). This observation highlights that synthetic tissues in aqueous environment can not only detect the presence or absence of an analyte in solution, but also sense directionality and analyte gradients at short length-scales (in the example shown in Fig. 4.4b, the linear dimensions of the printed construct are approximately $600 \times 600 \times 300\,\mu\mathrm{m}$ in *x*, *y* and *z* directions).

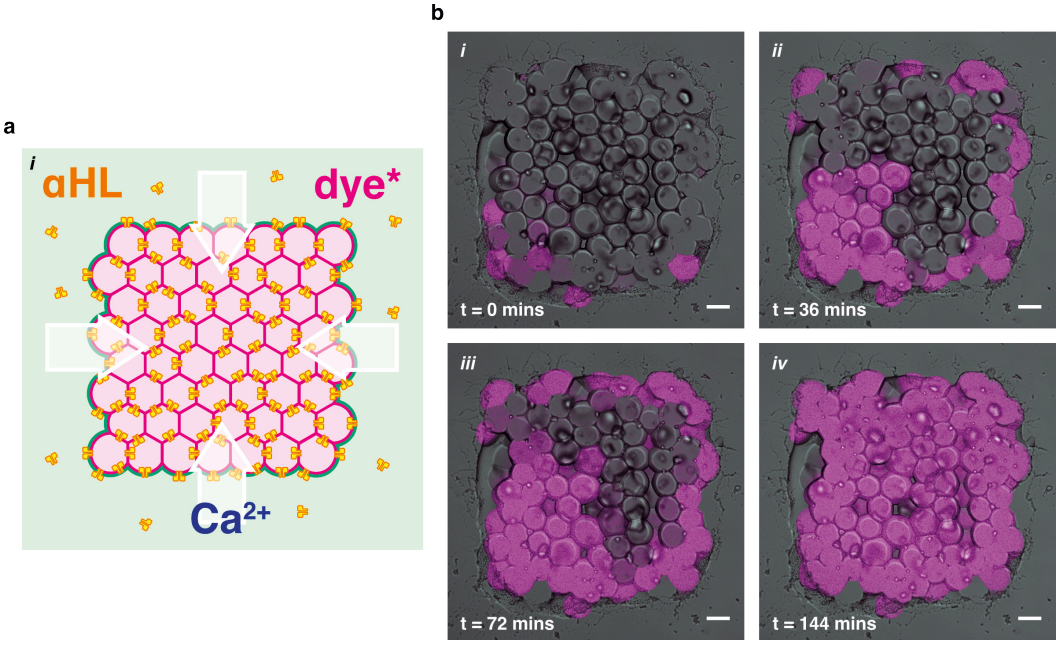

Fig. 4.4. Communication of transferred droplet networks with the surrounding aqueous environment. **a**, Diagram of a transferred 3D-printed synthetic tissue containing αHL (in yellow) and a calcium indicator dye (in pink). In the presence of αHL, calcium added to the external aqueous solution can diffuse into the construct, activating the calcium indicator dye. **b**, Brightfield and fluorescent composite microscopy images showing the diffusion of calcium from the external aqueous solution into the synthetic tissue over time. Calcium was added in proximity of the bottom-left corner of the construct (*i*), and diffused into the synthetic tissue through the αHL pores inserted at its interface with the aqueous bulk and between the internal aqueous compartments (*ii-iv*), confirming the presence of functional lipid bilayers. Scale bars: $100\,\mu$m.

4.4 Conclusions

The results presented in this chapter show that we can now fabricate 3D-printed droplet networks and synthetic tissues functioning in aqueous environment. This represents a crucial step towards functional constructs that could mimic the complexity of biological systems and that could be directly interfaced with living tissues in the future. Compared to multisomes and multi-compartment liposomes, our approach allows precise patterning of hundreds of picolitre-sized aqueous compartments, and their interfacing with an external aqueous environment. Additionally, since our approach does not rely on gravity as a driving force, we could phase transfer droplet networks into an aqueous solution of almost identical composition, except

the addition of small amounts of surfactant (1 wt % block copolymer F68). Phase transferred droplet networks preserved their compartmentalisation (Fig. 4.3d), which allowed us to fabricate synthetic tissues that interact with their surrounding aqueous environment (Fig. 4.4).

Following on from the presented initial results, we aim to further increase the complexity and levels of compartmentalisation of synthetic tissues by including organelle-like compartments within the 3D-printed aqueous droplets. 3D-printed networks and synthetic tissues, composed of aqueous compartments interfaced by lipid bilayers, mimic the membrane-mediated compartmentalisation of cells within living tissues. However, Nature evolved compartmentalisation at a range of different scales:[87] living cells not only confine much of their metabolic activity within the plasma membrane,[88] but many metabolic pathways are also compartmentalised within a complex architecture of sub-cellular organelles.[89]

Recently there has been an active interest in sub-cellular compartments, particularly membraneless organelles, both to understand their role and

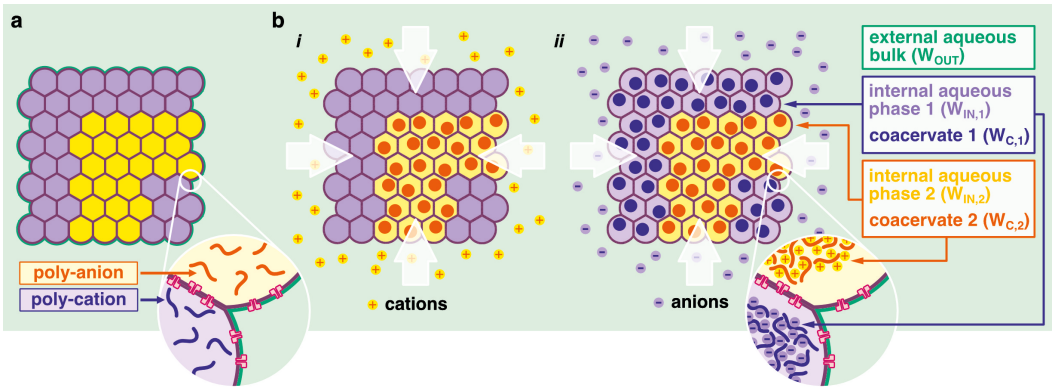

Fig. 4.5. Future directions of transferred droplet networks. Synthetic tissues with multiple levels of compartmentalisation could be fabricated by 3D-printing and phase transferring droplet networks with patterns compartmentalising two oppositely charged poly-electrolytes (**a**). **b**, After transfer, two different coacervate phases can be formed within the 3D-printed compartments by the sequential addition of a small molecule cation, which will form a coacervate phase with the encapsulated poly-anion (*i*), and of a small molecule anion, which will form a coacervate phase with the patterned poly-cation (*ii*). This will lead to the formation of a system in which multiple aqueous phases can be controlled and patterned in precise architectures.

functions in cellular metabolism,[90,91] and to take inspiration from this type of organisation to design novel synthetic systems.[42,51,52] Membraneless organelles are based on liquid-liquid phase separation of charged polymers[90,91] compartmentalise many vital metabolic processes within cells, such as the ribosome biogenesis within the nucleoli,[92] the nucleation of microtubules within centrosomes,[93] and sensing of stress conditions by stress granules.[94,95] Coacervate droplets have shown several interesting properties, including enhancement of enzyme catalysis,[96–98] partitioning of biomolecules,[99] and formation of molecularly crowded environments.[98,100]

Building on recent achievements in incorporating complex coacervates within synthetic cell platforms,[51,52] we aim to fabricate complex and precisely patterned 3D-printed synthetic tissues that can operate in aqueous environment, and contain synthetic organelles providing further organisation for specific metabolic processes (Fig. 4.5). Compared to dispersed synthetic cells with embedded synthetic organelles, our approach will also allow precise control of the spatial positioning of the cell-like compartments, and further enhance the overall functionality of synthetic tissues by collaborative emergent behaviour of hundreds of compartments and sub-compartments.

5 Conclusions and Outlook

In conclusion, the work presented in this thesis represents a fundamental study on the properties of 3D-printed droplet networks and synthetic tissues. In chapter 2 we dissected the parameters that affect the geometry of DIB systems, and demonstrated their effect on the arrangement of hundreds of 3D-printed picolitre-sized droplets. We found that we can easily modulate the equilibrium contact angle θ_{DIB} in droplet pairs by varying the lipid and oil composition, and that, at a critical contact angle θ_c of $35.3°$, we could achieve regular hcp packing of droplets in 3D-printed networks. As a result, we fabricated highly regular droplet networks and synthetic tissues patterned with single-droplet precision. Our improved understanding of the architecture and surface energy in 3D-printed droplet networks and synthetic tissues opens the way to a vast range of applications, some of which we discussed in chapters 3 and 4, and some of which still remain to be investigated.

In chapter 3, we demonstrated the fabrication of larger synthetic tissues by assembling building blocks 3D-printed independently. This represents a fundamental step towards scaling up the fabrication of synthetic tissues, in terms of both production turnover (reduction of production time by assembly of pre-fabricated building blocks), and size of the final manufactured constructs (up to cm-scales). We demonstrated the versatility of assembled synthetic

tissues through modular design: depending on the desired application, standard building blocks with simple functionalities can be assembled in different architectures to achieve specific overall outputs. Additionally, we showed that assembled droplet networks can *heal* after damage, demonstrating their potential for the fabrication of soft devices with long-term survival.

While assembling larger synthetic tissues is of great interest for biomedical applications, the fabrication of functional constructs with cell-sized compartments would provide valuable insight into the functionality of synthetic tissues patterned with increasingly high specific surface area. Towards this goal, we found that by using a combination of lighter oil mixtures ($\varphi_{SIL} = 0.05 - 0.15$) and mixtures of natural lipids ($1:1$ mole ratio of POPC to cholesterol), we could eject and 3D-print droplets of size comparable to human osteoblasts[101] ($20\,\mu\mathrm{m}$ diameter, $\sim 4\,\mathrm{pL}$ volume) and fibroblasts[102] ($15\,\mu\mathrm{m}$ diameter, $\sim 2\,\mathrm{pL}$ volume) (Fig. 5.1c). Following on from our preliminary observations, we aim to further study the properties of synthetic tissues printed at this resolution. In particular, we will investigate how increasing specific surface area impacts the mechanical properties of networks printed at this scale, due to the high adhesive energy provided by the large extension of lipid bilayer surface area. Large specific surface area may also enhance the effect of any membrane-dependent phenomena, such as trans-membrane transport and membrane protein activity.

One of the main limitations of 3D-printed synthetic tissues towards biomedical applications is that droplet networks currently exist and function in oil environments. In chapter 4, we demonstrated how 3D-printed droplet networks can be transferred to an aqueous environment by controlling the interfacial energies in the system. Using this method, we fabricated a simple synthetic tissue that could sense and report the presence of an analyte in the external aqueous solution. We now aim to expand the capabilities of synthetic tissues in aqueous environment by incorporating mechanisms to

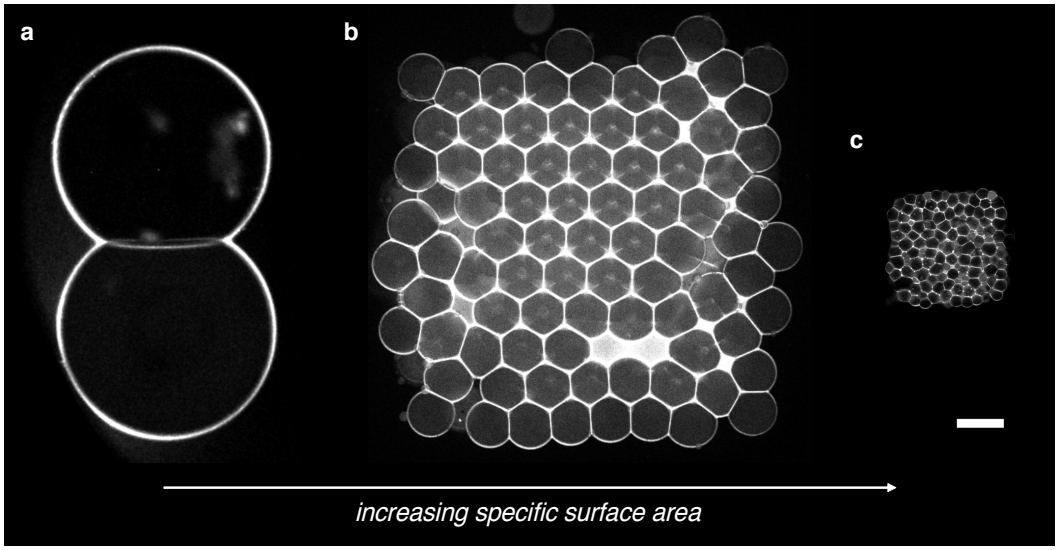

Fig. 5.1. Towards synthetic tissues with cell-sized compartments. **a**, Confocal fluorescent microscopy of a hand-made pair of $50\,\mathrm{nL}$ droplets. **b**, Confocal fluorescent microscopy of a 3D-printed network, consisting of hundreds of droplets of $\sim 524\,\mathrm{pL}$ volume. **c**, Confocal fluorescent microscopy of a 3D-printed network composed of hundreds of compartments of volume $\sim 4\,\mathrm{pL}$ ($20\,\mu\mathrm{m}$ diameter), comparable to the volume of a mature human osteoblast[101] and diameter comparable to a human fibroblast.[102] Scale bar: $100\,\mu\mathrm{m}$.

release molecules into the aqueous environment and then by coupling the sensing and releasing of molecules, resulting in synthetic tissues that can respond and adapt to changes in environmental conditions.

We ultimately aim to interface synthetic tissues with living cells, in order to monitor, control or complement their biological activity. In preliminary experiments towards this goal, we selectively stained living cells in close proximity of a droplet delivering a membrane-permeable fluorescent dye for nucleic acids (Fig. 5.2). In this setup, we immobilised RFP-expressing *Escherichia coli* (*E. coli*, K12 derivative BZB1011) cells within a thin layer of agarose (ultra-low gelling temperature, concentration $1.5\,\mathrm{wt}\,\%$ in LB media) at a starting concentration of $10^8\,\mathrm{cells/mL}$, and allowed them to proliferate at $37\,^{\circ}\mathrm{C}$ overnight to achieve high cell density. We then added a droplet containing the membrane-permeable nucleic acid stain SYTO 9 (at a concentration of $7\,\mu\mathrm{M}$ in LB media) on top of the hydrogel layer, forming a droplet-hydrogel bilayer[103] (DHB, Fig. 5.2a*i* and b*i*). Within minutes, the nucleic acid dye permeated through the lipid bilayer (Fig. 5.2a*ii* and b*ii*) and selectively

stained cells positioned in close proximity, while more distant cells appeared unaffected (Fig. 5.2a*iii* and b*iii*).

Following from our preliminary experiments, we will investigate the chemical communication between living cells and 3D-printed synthetic tissues. First, we will expand the range of chemical signals that can be delivered to

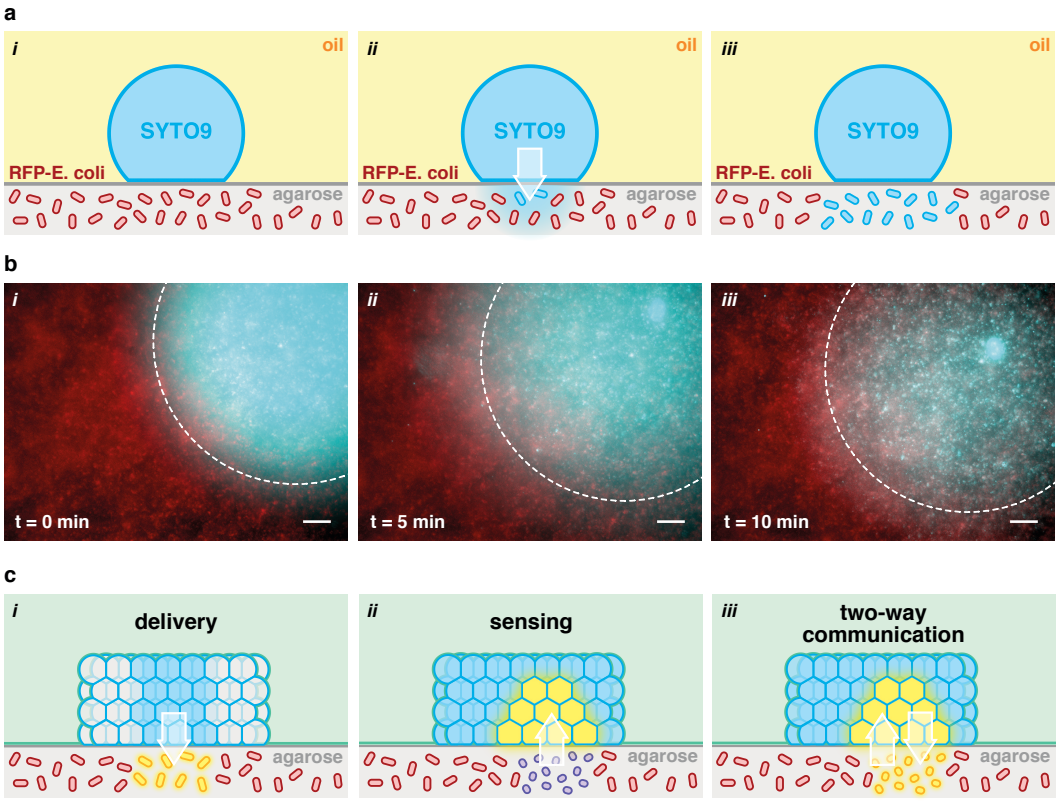

Fig. 5.2. Communication between synthetic tissues and living cells. **a**, Diagram of an aqueous droplet, containing a membrane-permeable fluorescent dye for nucleic acids (SYTO 9), generated in a lipid-oil solution, and put in contact with a thin layer of agarose containing RFP-tagged *E. coli* cells, to form a droplet-hydrogel bilayer (DHB) (*i*). The nucleic acid stain permeates through the lipid bilayer (*ii*) and selectively stains the cells in close proximity to the droplet (*iii*). **b**, Overlaid epi-fluorescent images of an aqueous droplet containing SYTO 9 nucleic acid stain (cyan channel) on top of a thin layer of hydrogel containing encapsulated RFP-tagged *E. coli* cells (red channel), to form a DHB (*i*). Within minutes, the dye permeated through the lipid bilayer (*ii*) and selectively stained cells positioned below the droplet, while distant cells remained unaffected (*iii*). **c**, Diagrams of synthetic tissues that can: *i*) deliver inducer molecules to a hydrogel-embedded cell culture, activating the expression of fluorescent proteins within the modified cells; *ii*) sense and report (through the local *in-vitro* expression of a fluorescent protein) quorum molecules from a heterogeneous culture of bacterial cells; and *iii*) engage in two-way communication with living cells, by sensing the local presence of a bacterial strain and respond by locally secreting molecules (e.g. anti-microbial agents).

living cells. For instance, we will design synthetic tissues to deliver inducer molecules in a spatially-controlled manner to modified bacteria containing synthetic plasmids designed to respond with the expression of proteins and fluorescent reporters (Fig. 5.2c*i*). By using networks transferred to aqueous environment, we will also couple the release of the inducer to an external trigger: for example, by adding a bilayer-permeable inducer molecule (e.g. isopropyl β-d-1-thiogalactopyranoside, IPTG), we can trigger the expression of α-HL pores in synthetic tissues loaded with an *in-vitro* transcription and translation mix[20] (IVTT), which will in turn allow a membrane-impermeable inducer (e.g. arabinose) to reach the underlying cells.

Next, we will design synthetic tissues that can sense the presence of living cells. To show this, we will encapsulate genetic constructs in synthetic tissues encoding for the expression of a fluorescent reporter in response to quorum molecules secreted by the underlying bacteria[47] (Fig. 5.2c*ii*). We will investigate the ability of 3D-printed constructs to detect the presence of colonies of specific strains in mixtures of immobilised bacteria.

Lastly, we will combine the sensing and delivery abilities of synthetic tissues to engineer two-way communication with living cells (Fig. 5.2c*iii*). We will design synthetic tissues containing genetic constructs encoding for the expression of α-HL in response to quorum molecules secreted by bacterial cells. The consequent local permeabilisation of lipid bilayers will allow the spatially- and temporally-controlled secretion of molecules in response to the received quorum signal. For instance, an inducer could be released to trigger expression of a fluorescent reporter within the bacteria. A possible application of this setup would be the control or prevention of growth of specific bacteria populations based on the local detection of strain-specific quorum molecules, triggering the localised release of anti-microbial agents.

In the future, we aim to design increasingly complex systems in which synthetic tissues can interact with living cells and tissues to monitor, control or complement their metabolic activity and development. For example, by designing synthetic tissues capable of secreting specific growth factors and inducer molecules in specific areas of a mammalian stem cell culture, we could control the growth of complex cultures with desired architectures. We could also achieve improved temporal control by regulating the release of molecules as a response to specific metabolic markers sensed by the synthetic tissue. Interfacing synthetic tissues with living cells could allow us to control and program cell and tissue behaviour eliminating the need for genetic engineering. While progress in the development of prosthetic gene networks encapsulated within genetically modified cells is showing promising results,[104–108] purpose-built synthetic tissues may represent a safe and flexible tool to encapsulate external genetic circuitry that could control or aid cellular metabolism both *in-vitro*, and in the future *in-vivo*.

6 Experimental details

6.1 Materials

Reagent	Supplier
1-palmitoyl-2-oleoyl-sn-glycero-3-phosphocholine (POPC)	Avanti Polar Lipids
1,2-dimyristoyl-sn-glycero-3-phosphocholine (DMPC)	Avanti Polar Lipids
1,2-dioleoyl-sn-glycero-3-phosphocholine (DOPC)	Avanti Polar Lipids
1,2-diphytanoyl-sn-glycero-3-phosphocholine (DPhPC)	Avanti Polar Lipids
Agarose, ultra-low gelling temperature	Sigma-Aldrich
Atto488	Sigma-Aldrich
Atto550M	Sigma-Aldrich
Calcium Chloride	Sigma-Aldrich
Chloroform	Sigma-Aldrich
Dimethyl sulfoxide (DMSO)	Sigma-Aldrich
Dulbecco's Phosphate Buffered Saline	Sigma-Aldrich
(Ethylenedinitrilo)tetraacetic acid (EDTA)	Sigma-Aldrich
Ethidium bromide-*N,N'*-bis(acrylemide)	Sigma-Aldrich

(Continues on next page)

(Continued from previous page)

Reagent	Supplier
Irgacure 2959	Sigma-Aldrich
MagneHis™ Ni-particles	Sigma-Aldrich
Poloxamer F68	Sigma-Aldrich
Poly(ethylene glycol) diacrylate mw 700	Sigma-Aldrich
Poly(ethylene glycol) mw 4000	Sigma-Aldrich
Rhod dextran, potassium salt, mw 10,000	ThermoFisher Scientific
Silicone oil AR20	Sigma-Aldrich
Sodium Chloride	Sigma-Aldrich
Tris-HCl pH 7.6	Sigma-Aldrich
Ultrapure MilliQ water	Merck Millipore
Undecane	Sigma-Aldrich

Tab. 6.1. List of materials used throughout the presented work.

6.2 Instruments

Instrument	Manufacturer
Axopatch 200B patch clamp amplifier	Axon Instruments, USA
DMi8 inverted epifluorescent microscope	Leica, Germany
EZ4 stereo microscope	Leica, Germany
Fluoview FV3000 confocal microscope	Olympus, Japan
Hamilton microliter syringes	Hamilton, USA
monoFAB SRM-20 milling machine	Roland, Japan
PC-10 dual stage glass capillary puller	Narishige, Japan
SP5 Confocal Microscope	Leica, Germany

(Continues on next page)

(Continued from previous page)

Instrument	Manufacturer
SZX10 upright stereo microscope	Olympus, Japan
Tokai Hit™ TPX (type HF) Thermo Plate	Leica, Germany

Tab. 6.2. List of instruments used throughout the presented work.

6.3 Methods

6.3.1 Lipid-oil solutions

Lipids were purchased from Avanti Polar Lipids in powder form, solubilised in chloroform at a concentration of $25\,\mathrm{mg\,mL^{-1}}$, and stored at $-20\,^{\circ}\mathrm{C}$ in PTFE-capped glass vials (Supelco). Undecane and silicone oil AR20 were purchased from Sigma-Aldrich and filtered through $0.22\,\mu\mathrm{m}$ vacuum filters (Corning).

To prepare a lipid-oil solution, a lipid film was first formed in a glass vial by dispensing desired volumes of lipid stock solutions in chloroform using glass syringes (Hamilton, US), and by subsequently evaporating the chloroform under a gentle stream of nitrogen, while slowly rotating the vial by hand. The lipid film was fully dried in a desiccator for at least $1\,\mathrm{h}$. The oil mixture was prepared by dispensing desired volumes of filtered undecane and silicone oil AR20 in a glass vial, using Gilson pipettes and Ultra-low retention pipette tips (Brand), and by thoroughly mixing by vortexing. The pre-mixed oil mixture was added to the vial containing the desiccated film, and the lipid-oil solution

was mixed by sonication for $30\,\mathrm{min}$. Before each experiment, the lipid-oil solutions were re-dispersed by sonication for $30\,\mathrm{min}$.

6.3.2 Aqueous solutions

Phosphate buffered saline (PBS) was filtered through $0.22\,\mu\mathrm{m}$ vacuum filters (Corning) before use. Tris-HCl buffer solutions were prepared by directly diluting the purchased stock solution ($1\,\mathrm{M}$ concentration) to a final concentration of $25\,\mathrm{mM}$. Stock aqueous solutions at high concentration of salts ($2\,\mathrm{M}$ NaCl, $0.5\,\mathrm{M}$ $CaCl_2$) and water soluble polymers ($30\,\mathrm{wt}\,\%$ PEG, $30\,\mathrm{wt}\,\%$ PEGDA, $5\,\mathrm{wt}\,\%$ F68) were prepared by directly dissolving purchased reagents in solid form in desired buffer (PBS or $25\,\mathrm{mM}$ Tris-HCl).

Stock solutions of fluorescent dyes (Atto488, Atto550M, ethidium bromide bisacrylemide) were prepared by dissolving the fluorophores in powder form in DMSO at high concentration ($>1\,\mathrm{mM}$). Photoinitiator stock solutions were prepared by dissolving Irgacure 2959 in powder form in DMSO at a concentration of $1\,\mathrm{mg}\,\mu\mathrm{L}^{-1}$. Stock solutions in DMSO were then directly dissolved in aqueous buffer at desired concentration.

6.3.3 Formation of hand-made droplet interface bilayers

Pairs, triplets and quartets of nanolitre-sized droplets were formed in custom-made poly(methyl methacrylate) (PMMA) containers. The PMMA containers were designed in AutoCAD (Autodesk) and manufactured using a desktop milling machine (monoFAB SRM-20, Roland). Typically, the design of the PMMA containers consisted of an array of 3×3 cylindrical wells, with diameter and depth of $2\,\mathrm{mm}$ and $1.5\,\mathrm{mm}$, respectively (Fig. 6.1a).

A volume of $200\,\mu\mathrm{L}$ of lipid-oil solution was first added to the well array, after which aqueous droplets of volume $50 - 75\ \mathrm{nL}$ were dispensed in each well by manual injection (using a $0.5\,\mu\mathrm{L}$ Hamilton syringe). Before formation of DIBs, the droplets were incubated in the oil lipid solution for at least $15\,\mathrm{min}$ to allow formation of a well-packed lipid monolayer at the water-oil interface. Following incubation, the droplets were brought into contact using gravity (by tilting the well array) or by manual manipulation with a thin plastic wire. For experiments in which the equilibrium contact angle θ_{DIB} was measured, the well arrays containing formed DIBs were incubated for $1\,\mathrm{h}$ at room temperature in a humidified environment before imaging. For relevant experiments, temperature was controlled using a Tokai Hit™ Leica TPX Thermo Plate (type HF).

For experiments investigating the kinetics of DIB formation, an altered design of the well array was used. In this design, wells were "L" shaped, with the ends consisting of two flat supports at different heights, and the middle consisting of a slope that connected the two (Fig. 6.1b). Droplets were formed and incubated at the two flat ends of the track and then brought together by pushing the droplet at the top towards the slope. This design allowed us to monitor and quantify the increase in contact angle over time

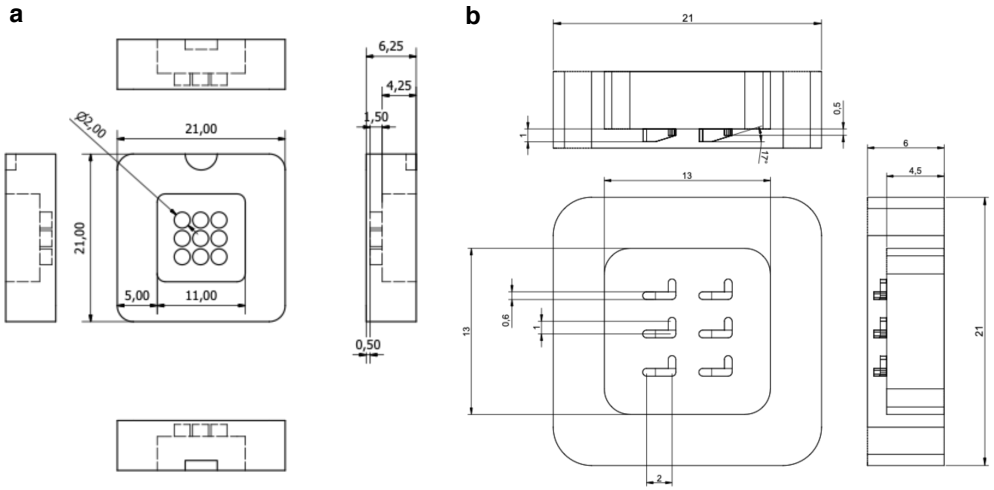

Fig. 6.1. Technical drawings of PMMA well arrays. **a**, Diagram for a 3×3 well array used for contact angle measurements. **b**, Diagram of a well array used to investigate the kinetics of DIB formation.

by time-lapse imaging the two droplets during and after collision (acquired on a Leica DM8i inverted microscope in brightfield mode at $10\,\mathrm{fps}$, using HCX PL FLUOTAR 10x/0.30na dry objective).

6.3.4 3D-printing droplet networks

To 3D-print droplet networks we used the custom-built 3D-printer extensively described in previous work[26] (Fig. 6.2). This system consisted of a piezo-actuated droplet-on-demand ejection system synchronised to a moving stage. In brief, a piezoelectric actuator generated controlled pressure waves within a chamber filled with water (Milli-Q). Glass nozzles were fabricated using a capillary puller (PC-10 dual stage glass capillary puller, Narishige) to form a nozzle opening diameter of approximately $100 - 150\,\mu\mathrm{m}$, and subsequently bent by heating with a standard Bunsen burner to obtain the shape portrayed in Fig. 6.2. Before each print, glass nozzles were treated to increase hydrophilicity (by O_2 plasma cleaning) and inserted in the aqueous chamber, so that pressure waves generated in the chamber could travel through the aqueous solution through the glass nozzle, reaching the nozzle tip at the other end. A small volume of oil (usually $\sim 3\,\mu\mathrm{L}$ undecane) was loaded at the nozzle tip to separate the aqueous printing solution from the water within the piezo chamber. Lastly, a small volume of aqueous printing solution (usually $\sim 5\,\mu\mathrm{L}$) was added at the nozzle tip, which was then immersed in the bulk lipid-oil solution contained in a custom-built glass cuvette (internal size $2 \times 1 \times 1\ \mathrm{cm}$, Starna Scientific LTD, UK).

Once a pressure wave was generated by the piezo actuator, a picolitre-sized droplet (usually $100\,\mu\mathrm{m}$ in diameter, corresponding to $\sim 524\,\mathrm{pL}$ volume) was generated at the tip of the nozzle tip within the lipid-oil solution. The patterning of picolitre-sized droplets was imposed by the synchronised movement of the motorised micromanipulator stage (PatchStar 7000, Scientifica, $20\,\mathrm{nm}$

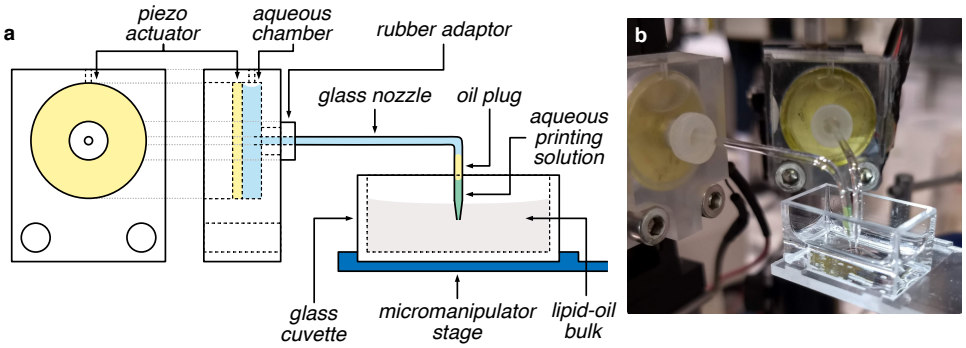

Fig. 6.2. Custom-built droplet 3D-printer. **a**, Diagram of the printing head, glass cuvette and motorised micromanipulator stage of the custom-made droplet 3D-printer. **b**, Photo of the droplet 3D-printer during simultaneous printing with two nozzles.

movement resolution) holding the printing cuvette. The synchronisation of droplet ejection and motorised stage movement was controlled by a custom-made software developed in LabView (National Instruments). Except for the experiments described in chapter 3, the custom-made glass cuvette used as a printing container was treated with O_2 plasma to increase the hydrophilicity of the surface. This treatment would cause the printed droplets to interact more strongly with the glass surface (likely due to the formation of a lipid bilayer with the glass[12]), limiting their movement and therefore resulting in more regular printed structures (Fig. 7.7).

The printing process was monitored using a stereomicroscope (Nikon SMZ-745T) mounted on the side of the printer, and pictures and videos were acquired during printing using a digital camera (Thorlabs DCC1645C).

6.3.5 Imaging droplet networks

Hand-made droplet pairs and small droplet clusters (triplets and quartets) were imaged using an inverted epifluorescence microscope (Leica DMi8, HCX PL FUOTAR 20X/0.40 dry objective) in brighfield mode (chapter 2.1 and 2.2).

Droplet pairs and 3D-printed networks transferred to aqueous bulk were imaged also through epifluorescence microscopy, to visualise encapsulated water soluble dyes and fluorescently tagged lipid bilayers and monolayers (excitation wavelength $450 - 490$ nm with emission cutoff at $550\,\mathrm{nm}$ for Atto488, and excitation wavelength $540 - 552$ nm with emission cutoff at $643\,\mathrm{nm}$ for Atto550M, chapter 4.1 and 4.2).

3D-printed networks were imaged using a laser scanning confocal microscope (Leica SP5, using a HC PL Fluotar 10X/0.30 objective 0.3na dry objective), at the following excitation and emission wavelengths:

Fluorophore	Excitation	Emission
Atto488	$488\,\mathrm{nm}$	$500 - 540$ nm
Atto550M	$546\,\mathrm{nm}$	$560 - 620$ nm
Rhod dextran	$546\,\mathrm{nm}$	$560 - 630$ nm

Tab. 6.3. Excitation and emission wavelengths used in confocal imaging.

The total volume of printed networks was usually imaged in "z-stack" mode, with step-size of $8\,\mu\mathrm{m}$. We acknowledge this is above the Nyquist limit,[72] however this step-size was chosen to allow for fast image acquisition and not aimed at reconstructing the 3D geometry of the network.

6.3.6 Droplet geometry reconstruction

As described in chapter 2.7, we both imaged and reconstructed the (apparent) geometry of individual fluorescent droplets within a printed network in oil environment, and the geometry of hydrogel replicas in aqueous environment. In both cases, networks and hydrogel replicas were imaged by laser scanning confocal microscopy (Olympus Fluoview FV3000 inverted microscope, UPlanSApo 20X/0.75 dry objective) with an x, y and z resolutions chosen according to Nyquist criterion.[72] Fluorescent hydrogel replicas, containing the cross-linked fluorophore ethidium bromide-*N,N'*-bisacrylemide, were imaged using an excitation wavelength of $405\,\mathrm{nm}$ and emission cutoff between 420

and $520\,\mathrm{nm}$. The reconstruction of the 3D geometry from confocal slices was performed using Arivis Vision4D® image analysis software.

6.3.7 Contact angle measurement in droplet pairs

To measure the equilibrium contact angle θ_{DIB} in droplet pairs, DIBs were formed following the protocol outlined in section 6.3.3. θ_{DIB} was calculated based on the radii R_1 and R_2 of the two droplets in the DIB pair and on their centre-to-centre distance L (see Fig. 2.1), following Eq. 2.1:

$$\theta_{DIB} = \frac{1}{2} cos^{-1}\left(\frac{L^2 - R_1^2 - R_2^2}{2R_1R_2}\right)$$

To minimise error, only pairs of droplets of similar radius were considered. The script to automatically measure θ_{DIB} from brightfield images was developed in MATLAB® (Mathworks) can be found in Supplemental Information 7.3.

In order to understand how experimental variations in the measured parameters L, R_1 and R_2 would affect the calculated θ_{DIB}, we can consider the propagation of error for Eq. 2.1. By applying the variance formula,[109] we can estimate the sample standard deviation of θ_{DIB} ($s_{\theta_{DIB}}$) as:

$$s_{\theta_{DIB}} = \sqrt{\left(\frac{\partial\theta_{DIB}}{\partial L}s_L\right)^2 + \left(\frac{\partial\theta_{DIB}}{\partial R_1}s_{R_1}\right)^2 + \left(\frac{\partial\theta_{DIB}}{\partial R_2}s_{R_2}\right)^2} \tag{6.1}$$

where s_L, s_{R_2} and s_{R_2} are the sample standard deviations for L, R_1 and R_2, respectively. To simplify the calculations, we can define a new function y as:

$$y = \frac{L^2 - R_1^2 - R_2^2}{2R_1R_2} \tag{6.2}$$

The partial derivatives of θ_{DIB} with respect to L, R_1 and R_2 will be:

$$\frac{\partial \theta_{DIB}}{\partial L} = \frac{\partial \theta_{DIB}}{\partial y} \cdot \frac{\partial y}{\partial L} = -\frac{1}{2\sqrt{1-y^2}} \cdot \frac{L}{R_1 R_2} \tag{6.3}$$

$$\begin{aligned} \frac{\partial \theta_{DIB}}{\partial R_1} &= \frac{\partial \theta_{DIB}}{\partial y} \cdot \frac{\partial y}{\partial R_1} = \\ &= -\frac{1}{2\sqrt{1-y^2}} \cdot \left[\frac{L^2 - R_2}{2R_2} \cdot \left(-\frac{1}{R_1^2} \right) - \frac{1}{2R_2} \right] = \\ &= \frac{1}{2\sqrt{1-y^2}} \cdot \left[\frac{L^2 - R_2}{2R_1^2 R_2} + \frac{1}{2R_2} \right] = \\ &= \frac{1}{2\sqrt{1-y^2}} \cdot \frac{L^2 + R_1^2 - R_2}{2R_1^2 R_2} \end{aligned} \tag{6.4}$$

$$\frac{\partial \theta_{DIB}}{\partial R_2} = \frac{\partial \theta_{DIB}}{\partial y} \cdot \frac{\partial y}{\partial R_2} = \frac{1}{2\sqrt{1-y^2}} \cdot \frac{L^2 + R_2^2 - R_1}{2R_2^2 R_1} \tag{6.5}$$

We can now estimate the variation on the calculated θ_{DIB} due to variations in the measured droplet radii R_1 and R_2 and on the centre-to-centre distance L. In pairs of $50\,\mathrm{nL}$ droplets, the droplet radii will measure approximately $230\,\mu\mathrm{m}$. If we consider a centre-to-centre distance $L = 400\,\mu\mathrm{m}$, we obtain $\theta_{DIB} \simeq 30°$ from Eq. 2.1. Let us consider a case of large variability in R_1, R_2 and L, in which the coefficient of variation in the measurement of these parameters is equal to 0.1. In this extreme case, we will have:

$$L = 400 \pm 40\mu m \qquad R_1 = 230 \pm 23\mu m \qquad R_2 = 230 \pm 23\mu m \tag{6.6}$$

We can substitute these values in Eq. 6.2, 6.3, 6.4 and 6.5 to obtain:

$$y = \frac{400^2 - 230^2 - 230^2}{2 \cdot 230 \cdot 230} \simeq 0.5 \tag{6.7}$$

$$\frac{\partial \theta_{DIB}}{\partial L} = -\frac{1}{2\sqrt{1-0.5^2}} \cdot \frac{400}{230 \cdot 230} \simeq -4.4 \times 10^{-3} \tag{6.8}$$

$$\frac{\partial \theta_{DIB}}{\partial R_1} = \frac{1}{2\sqrt{1-0.5^2}} \cdot \frac{400^2 + 230^2 - 230}{2 \cdot 230^2 \cdot 230} \simeq 8.7 \times 10^{-3} \tag{6.9}$$

$$\frac{\partial \theta_{DIB}}{\partial R_2} = \frac{\partial \theta_{DIB}}{\partial R_1} \simeq 8.7 \times 10^{-3} \tag{6.10}$$

Lastly, we can substitute these values and the standard deviations in Eq. 6.6 in the variance formula (Eq. 6.1) to obtain:

$$s_{\theta_{DIB}} = \sqrt{(4.4 \times 10^{-3} \cdot 40)^2 + (8.7 \times 10^{-3} \cdot 23)^2 + (8.7 \times 10^{-3} \cdot 23)^2} = \\ \simeq 0.33 \tag{6.11}$$

The calculated standard deviation corresponds to a coefficient of variation of 0.01 (for $\theta_{DIB} = 30°$) and is one order of magnitude smaller than the respective coefficients of variation chosen for L, R_1 and R_2 in this example. This result highlights the robustness of the indirect measurement of θ_{DIB} using Eq. 2.1, even in cases of large variations in the parameters from which it is calculated.

By analysing the sizes of droplet in 3D-printed networks printed at low θ_{DIB} ($\varphi = 0.35$, $x_{POPC} = 0.00$, $\theta_{DIB} = 9.9°$), we could estimate the average radius in printed droplets as $R_{drop} = 51.3 \pm 2.7\,\mu\mathrm{m}$, which corresponds to a coefficient of variation of 0.05. Through similar calculations as described above, we could find an expected standard deviation for θ_{DIB} of $0.12\,°$ (coefficient of variation of 4×10^{-4}). This demonstrates how, in typical printing conditions, variation in droplet size has minimal impact on the equilibrium contact angle in 3D-printed networks.

6.3.8 Droplet packing analysis in printed networks

Acknowledgement of collaboration: the development of the analysis software presented in this section was performed by our collaborator Oliver J. Meacock (Kevin Foster Group, Department of Zoology, University of Oxford) and can be found at:
https://github.com/Pseudomoaner/NetPack.
Bias was avoided by performing the classification and analysis blind to the experimental conditions used.

Fluorescent confocal images of droplet networks, in which lipid bilayers and monolayers were tagged with Atto500M, were acquired following the protocol outlined in section 6.3.5. For each printed network, we chose the confocal slice within the acquired z-stack in which the fluorescent signal from the lipid bilayers and monolayers at the first droplet layer appeared with maximum contrast compared to the background.

The fluorescent signal was used to segment the image into areas by application of a ridge detection algorithm,[69] followed by visual verification and eventual manual correction. The identified regions were classified as "droplets" or "oil inclusions" based on their morphology: droplet areas had to be between 0.4 and 10 times the median area of the identified regions, and at the same time they had to be largely convex (face area to convex hull ratio greater than 0.9). Other regions were classified as oil inclusions.

Based on this simple first step of image analysis, we could quantify several morphological properties of the networks. For instance, we quantified the area fraction occupied by oil inclusions (AF_{oil}, see plot in Fig. 2.7a) as:

$$AF_{oil} = \frac{\sum A_{oil}}{\sum A_{drop} + \sum A_{oil}}$$

in which A_{oil} and A_{drop} represent the pixel areas occupied by oil inclusions and droplets, respectively.

We could also quantify the number of excess droplets in the first layer due to falling or rolling from the upper layers (see plot in Fig. 2.7b). The droplet excess (DE) was quantified as:

$$DE = \frac{N - N_e}{N_e}$$

in which N represents the number of counted droplets in the first layer, and N_e represents the number of expected droplets according to the printing map. For a printed network of dimensions $7 \times 8 \times 4$ droplets, the expected value of droplets was $N_e = 8 \times 9 = 72$: this was due to the offset of the second layer on top of the first, which caused some droplets to systematically fall (see Fig. 7.3).

Lastly, we quantified the variability in droplet size as the coefficient of variation of the cross-sectional area (CV_A, see plot in Fig. 2.7c) of the segmented droplets, as:

$$CV_A = \frac{\sigma(A_{drop})}{\overline{A}_{drop}}$$

in which $\sigma(A_{drop})$ and $\overline{A}_{drop}$ represent the standard deviation and average value of the droplet areas, respectively. This parameter gave us a cumulative indication of both the variation of droplet size during ejection and of droplet geometry within the network, which would result in different cross-sectional areas.

We used the segmented images of the first layer of droplets in printed networks to classify their packing arrangements based on Delaunay triangulation.[70] To perform this triangulation, we generated a mesh over the segmented image by connecting the centres of the regions classified as droplets. Each triangle in this mesh described the spatial arrangement of a triplet of droplets

within the network, and based on the geometry of this triangle we classified the packing arrangement of the underlying droplet triplet.

By plotting the bivariate distribution of the largest internal angle of each triangle (α_{max}) against the triangle area ($\hat{A}_t$, normalised over the average droplet area) for the whole data-set of printed networks (129 prints), we could identify two clusters of triangles, which corresponded to triplets packed according to a regular hexagonal lattice ($\alpha_{max} \simeq 60°$) and to a regular square lattice ($\alpha_{max} \simeq 90°$), respectively (Fig. 2.3e). Based on α_{max} and $\hat{A}_t$, we defined four classes of packing of droplet triplets:

- *hexagonal* – droplets are close-packed ($0.25 < \hat{A}_t < 0.75$), with $60° \leq \alpha_{max} < 67°$)
- *square* – droplets are close-packed ($0.25 < \hat{A}_t < 0.75$), with $83° \leq \alpha_{max} < 97°$)
- *amorphous* – droplets are close-packed ($0.25 < \hat{A}_t < 0.75$), with $67° \leq \alpha_{max} < 83°$)
- *no-packing* – droplet arrangements not included in the above ranges

Based on this classification, we quantified the area fraction occupied by each packing arrangement in networks printed at different conditions (Fig. 2.6c and 2.9c-d).

6.3.9 Localisation of packing arrangements

We considered the set of printed networks formed at the condition $\varphi_{SIL} = 0.55$ and $x_{POPC} = 0.13$, which was characterised by the largest fraction of hexagonally packed droplets (0.50 ± 0.07 area fraction, $n = 5$, see Fig. 2.9c-e). We registered the confocal images of the bilayer networks in the first layer manually using ImageJ (Interactive Rigid Transform, Fig. 2.10a). We analysed the packing structure of each of the registered confocal images as

described in section 6.3.8, and we use the analysed images to generate a heatmap describing the localisation of each packing regime. Specifically, we overlaid an idealised map of the printed network on the registered confocal images, and for each region in the map (which represented a single droplet in the network), we calculated the relative occurrence of each packing arrangement. This analysis allowed us to generate the heatmaps that describe the localisation of hexagonal, square, amorphous and no-packing in printed networks shown in Fig. 2.10b.

6.3.10 Electrical recordings

For all electrical recordings presented in chapters 2.8 and 3, we 3D-printed aqueous droplets composed of $25\,\mathrm{mM}$ Tris-HCl pH 7.6, $1\,\mathrm{M}$ NaCl, $0.1\,\mathrm{wt}\,\%$ Pluronic F68, with the addition of α-hemolysin (purified from *Staphylococcus Aureus*, at final concentration $60\,\mu\mathrm{g\,mL^{-1}}$) and $10\,\mu\mathrm{M}$ Atto488 fluorescent dye for droplets composing the conductive pathways.

The electrodes used for the recordings consisted of silver wires ($100\,\mu\mathrm{m}$ diameter, Sigma-Aldrich) soldered to male crimp connectors. Before each experiment, the tips of the electrodes were incubated for a minimum of $10\,\mathrm{min}$ in sodium hypochlorite solution (Sigma-Aldrich) and subsequently coated with a thin layer of hot agarose ($1.5\,\mathrm{wt}\,\%$ ultra-low gelling temperature agarose, in the same solution as that of the aqueous droplets).

Electrical recordings were performed in a Faraday cage (custom built, Mechanical Workshop, Department of Chemistry, University of Oxford) containing the headstage of a patchclamp amplifier (Axopatch 200B, Axon Instruments). The recording electrodes were connected to two female connectors, which were fixed on two manual micromanipulators (Narishige, NMN-1) and electrically connected to the amplifier's headstage. The micromanipulators

allowed us to position the tips of the Ag/AgCl wires in precise locations of the printed networks. The electrical current traces were recorded using pClamp 10 software (Molecular Devices) and analysed with MATLAB®.

7 Supplemental Material

7.1 Supplementary Figures

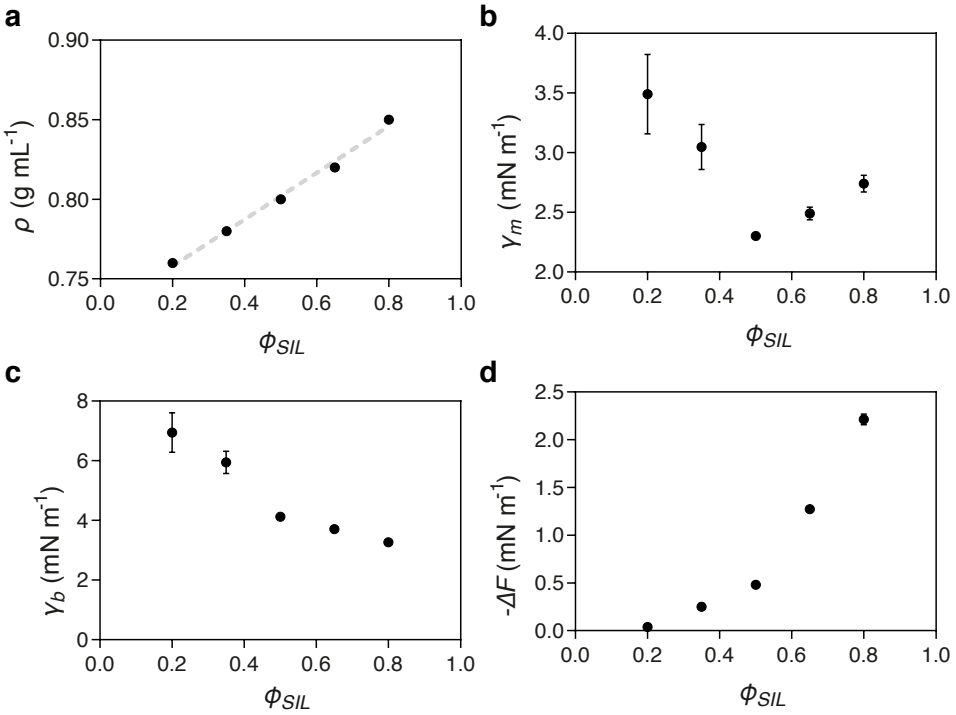

Fig. 7.1. Interfacial energies in DIBs. **a**, Plot showing the linear relationship of the density of the undecane-silicone oil mixture at increasing φ_{SIL}. **b**, Plot of the variation in lipid monolayer surface energy γ_m with respect to φ_{SIL}, measured through pendant drop analysis. **c**, Plot of the variation in lipid bilayer surface energy γ_b in droplet pairs with respect to φ_{SIL}, calculated from Eq. 2.3 by substituting the measured γ_m and θ_{DIB}. **d**, Plot of the change in adhesive energy per unit area ΔF with respect to φ_{SIL}, calculated from Eq. 2.4, by substituting the measured γ_m and θ_{DIB}.

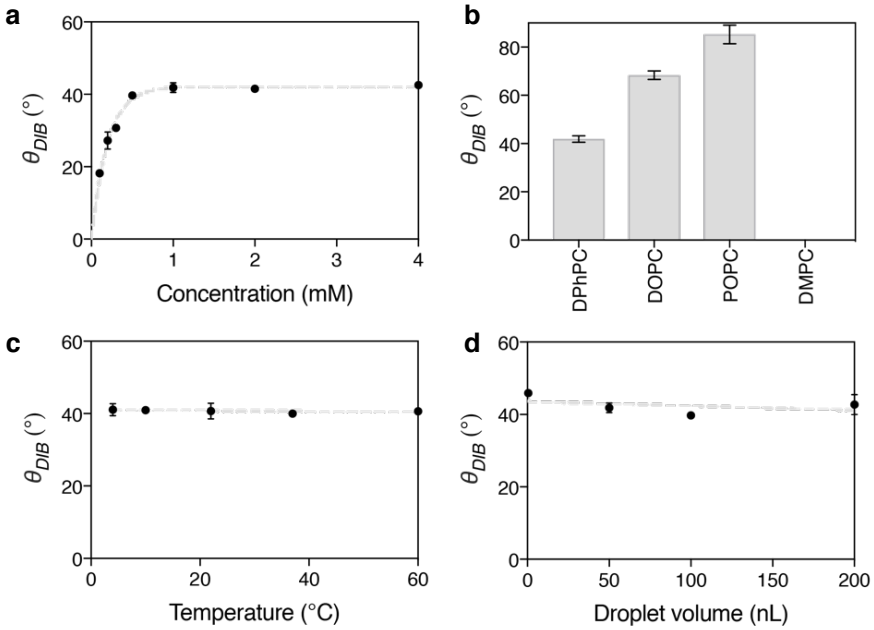

Fig. 7.2. Additional parameters affecting θ_{DIB}. **a**, Plot of the variation in θ_{DIB} with respect to the DPhPC concentration, at constant oil composition of $\varphi_{SIL} = 0.65$, showing saturation behaviour above $0.91\,\mathrm{mM}$ (Tab. 7.5). **b**, Dependence of θ_{DIB} on lipid type, at constant $\varphi_{SIL} = 0.65$. All $n = 6$ pairs formed using DMPC lipids coalesced. **c**, Plot showing the non-significant effect of temperature on θ_{DIB} in the range $4 - 60\,^{\circ}\mathrm{C}$ (Tab. 7.3 and 7.4). **d**, Plot showing the non-significant effect of droplet size on θ_{DIB} in the range $0.52 - 200\,\mathrm{nL}$ (Tab. 7.6).

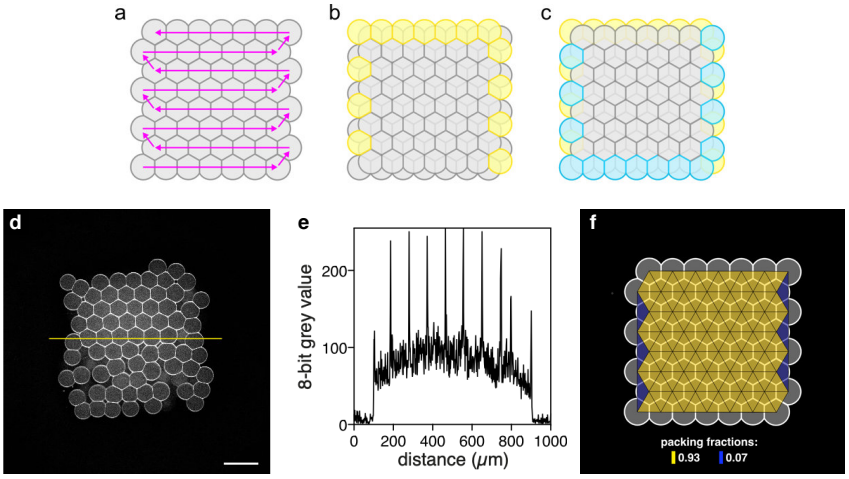

Fig. 7.3. Ideal droplet packing and bilayer dye localisation. **a-c**, Idealised diagram of the first (**a**), second (**b**) and third (**c**) layers of a $7 \times 8 \times 4$ printed network. Magenta arrows indicate the droplet printing path (**a**). Droplets in the second and third layer with high chance of falling to the bottom layer (due to lack of support) are marked in yellow (**b**) and cyan (**c**), respectively. **d-e** Fluorescent confocal microscopy image (**d**) and correspondent line intensity profile (**e**) demonstrating the localisation of the fluorescent dye Atto550 at the lipid monolayers and bilayers. **f**, Packing analysis of an ideal map of a $7 \times 8 \times 4$ network, showing the theoretical maximum fraction of hexagonal packing.

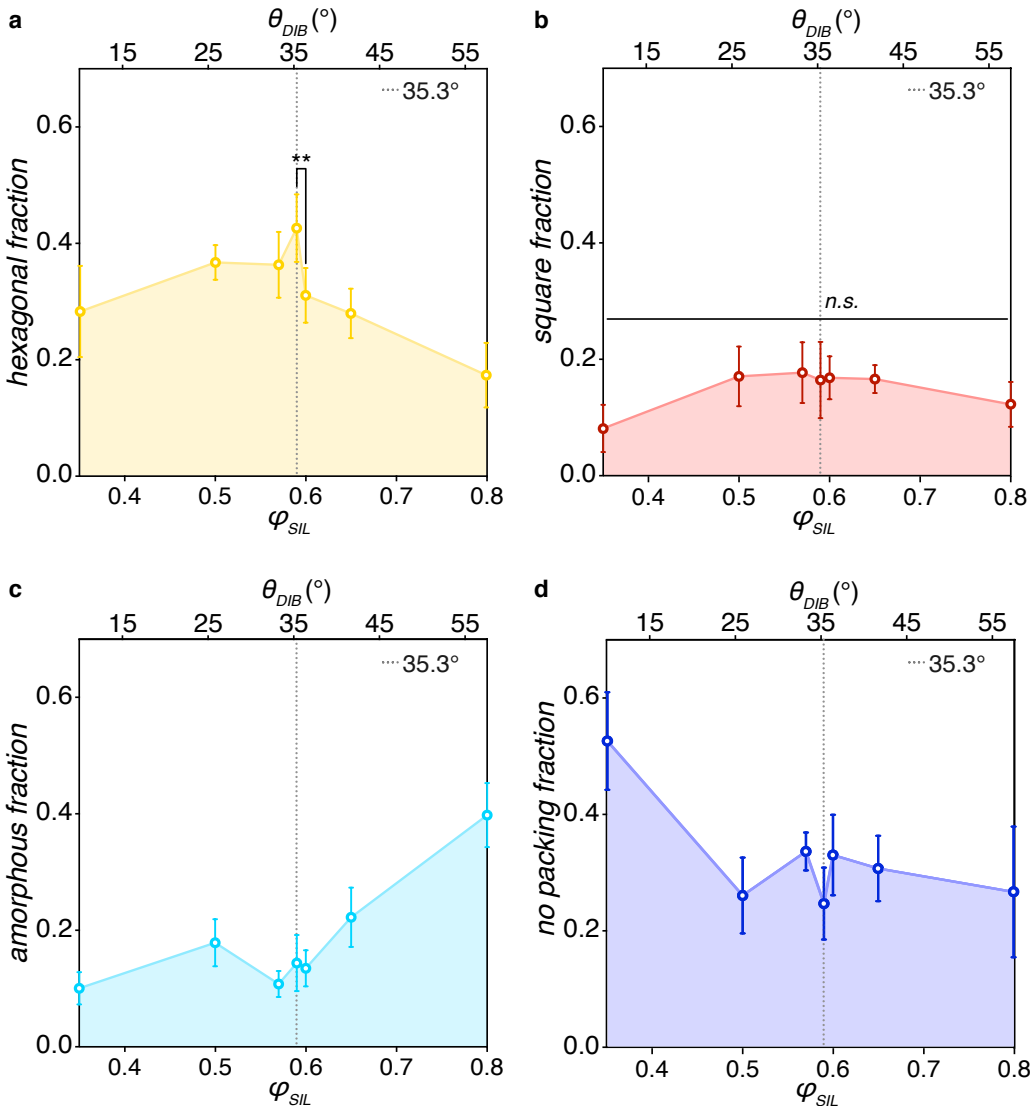

Fig. 7.4. Effect of θ_{DIB} on the packing arrangement of droplets. **a-d**, Plots of the hexagonal (**a**), square (**b**), amorphous (**c**) and no packing (**d**) fraction with respect to θ_{DIB} (Tab. 7.12, 7.13, 7.14 and 7.15 for statistical analysis).

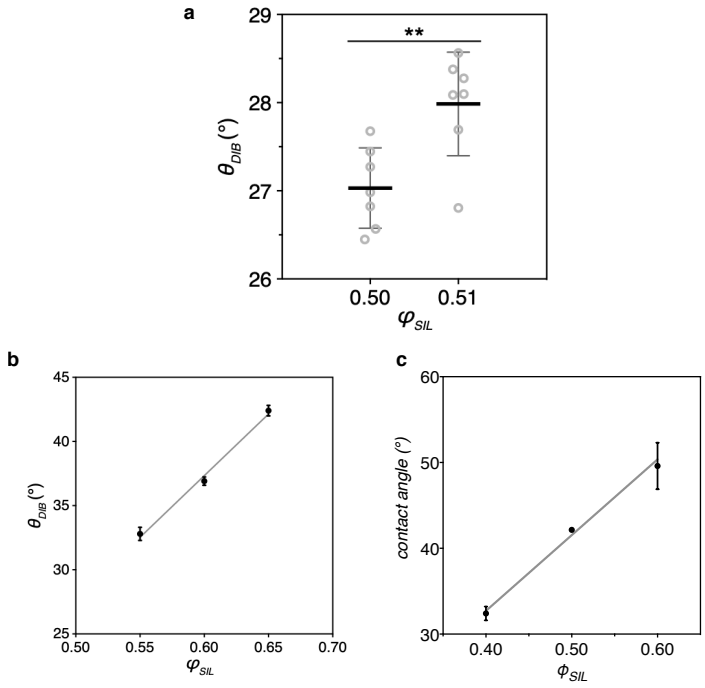

Fig. 7.5. Precision in θ_{DIB} and additional linear regressions. **a**, Comparison of measurements of θ_{DIB} in droplet pairs formed at $\varphi_{SIL} = 0.50$ and $\varphi_{SIL} = 0.51$, demonstrating the fine precision with which θ_{DIB} can be modulated (Tab. 7.30). **b-c**, Linear increase of θ_{DIB} with respect to φ_{SIL} for droplet pairs composed of $20\,\mathrm{wt}\,\%$ PEG diacrylate mw 700 and $0.5\,\mathrm{wt}\,\%$ Irgacure 2959 in PBS (**b**, chapter 2.7, Tab. 7.11), and $25\,\mathrm{mM}$ Tris-HCl pH 7.6, $1\,\mathrm{M}$ NaCl and $0.1\,\mathrm{wt}\,\%$ Pluronic F68 (**c**, chapter 2.8, Tab. 7.35).

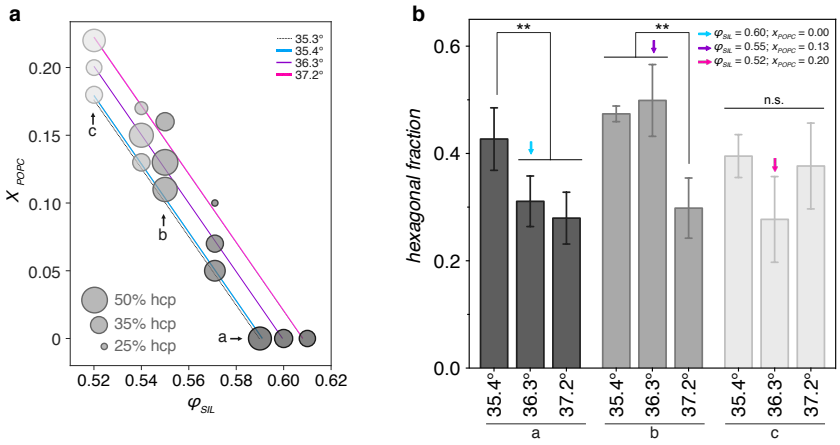

Fig. 7.6. Effect of lipid composition effects the hexagonal packing of 3D-printed droplet networks. **a**, Variation in hexagonal packing fraction in droplet networks printed at the equal θ_{DIB} (cyan line: $35.4°$, purple line: $36.3°$ and magenta line: $37.2°$), but obtained with different combinations of φ_{SIL} and x_{POPC} (from Eq. 2.5). Size of the circle indicates amount of hexagonal packing. **b**, Detailed bar chart referring to groups a, b and c in panel **a**. See Tab. 7.24 to 7.29 for statistical analysis, Tab. 7.10 for conditions used.

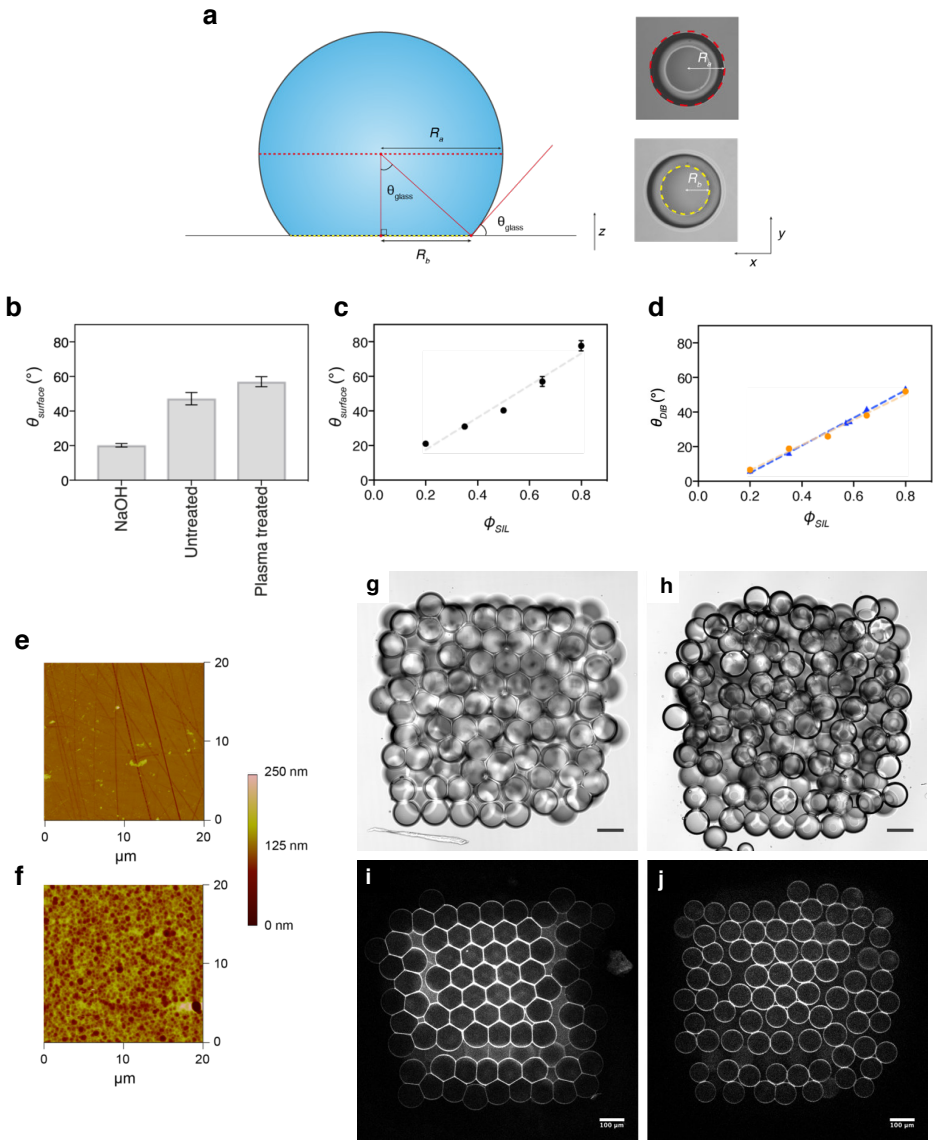

Fig. 7.7. Effect of surface in droplet networks. **a**, Diagram defining the contact angle with the glass substrate θ_{glass} showing how it was measured based on brightfield images. **b**, Comparison of θ_{glass} formed on roughened glass (NaOH), untreated glass and plasma treated glass. **c**, Linear relationship of θ_{glass} formed on plasma treated glass with φ_{SIL} (Tab. 7.8). **d**, Comparison of θ_{DIB} measurements performed on plastic (PMMA) substrate (blue) and plasma treated glass (orange) at various φ_{SIL}, showing no significant difference (Tab. 7.7). **g-h**, Brightfield images demonstrating the increased regularity of packing in 3D-printed droplet networks when formed on plasma cleaned glass (**g**) compared to roughened glass (**h**). **i-j**, Fluorescent confocal images demonstrating a decrease in contact angle and regularity of packing in 3D-printed networks formed at 32% (**j**) compared to 45% (**i**) relative environmental humidity. For all network in **g-j**, $\varphi_{SIL} = 0.59$ and $x_{POPC} = 0$. Scale bars: $100\,\mu$m.

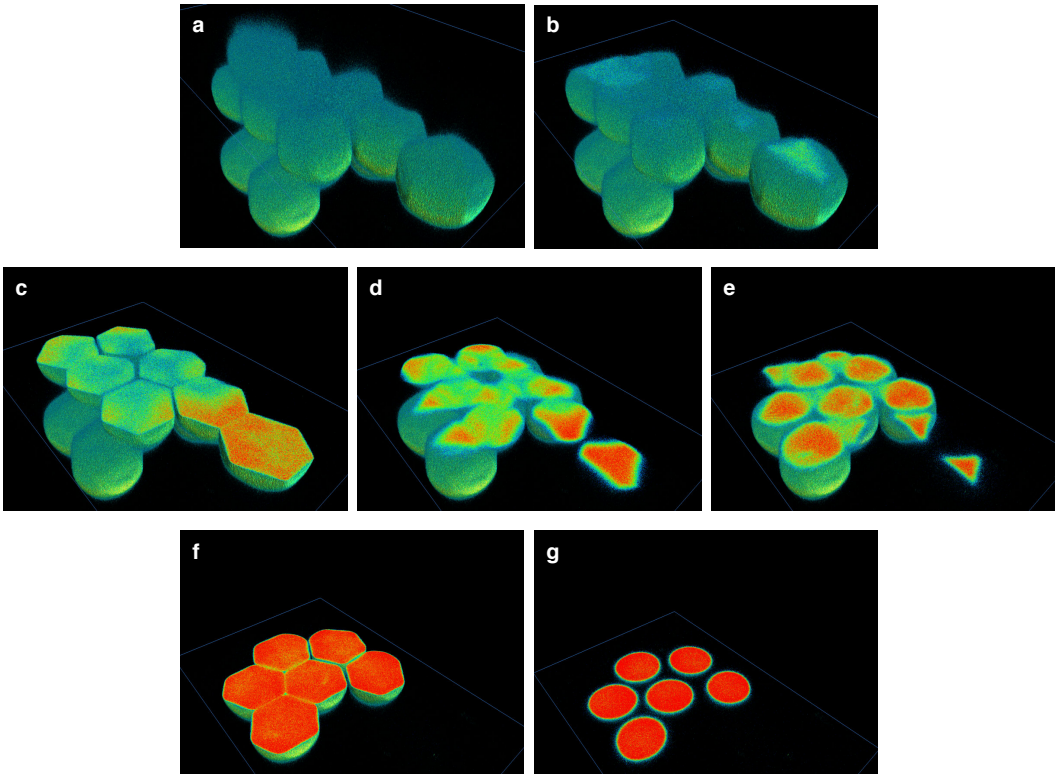

Fig. 7.8. 3D reconstruction of a hydrogel droplet replica cluster. **a-g**, Horizontal cross-sections of a 3D reconstruction of a droplet replica cluster obtained by processing z-stack confocal images using Arivis imaging software.

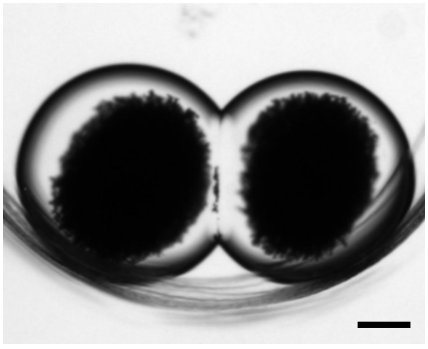

Fig. 7.9. Encapsulation of paramagnetic particles in droplet pairs. Brightfield image of a DIB containing MagneHis™ Ni precharged paramagnetic particles. After manipulation using a magnet, some beads can be seen localised at the lipid bilayer interface, which often caused coalescence of the droplet pair. Scale bar: $150\,\mu\mathrm{m}$.

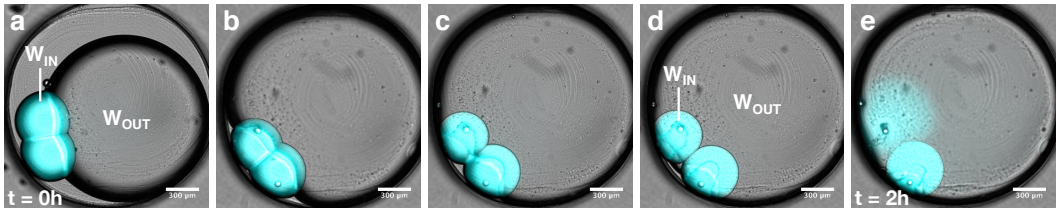

Fig. 7.10. Osmotic stress in phase tranferred droplet pairs. **a-e**, Brightfield and fluorescent microscopy time-lapse images of a droplet pair composed of an aqueous solution with a high concentration of solutes ($20\,\mathrm{wt}\,\%$ PEG_{4k} in PBS) to an external aqueous solution at a lower solute concentration ($5\,\mathrm{wt}\,\%$ F68 in PBS) Scale bar: $300\,\mu\mathrm{m}$. The osmotic stress due to the flux of water molecules from the external (W_{OUT}) to the internal (W_{IN}) aqueous solutions caused the droplets to swell and eventually rupture (**e**).

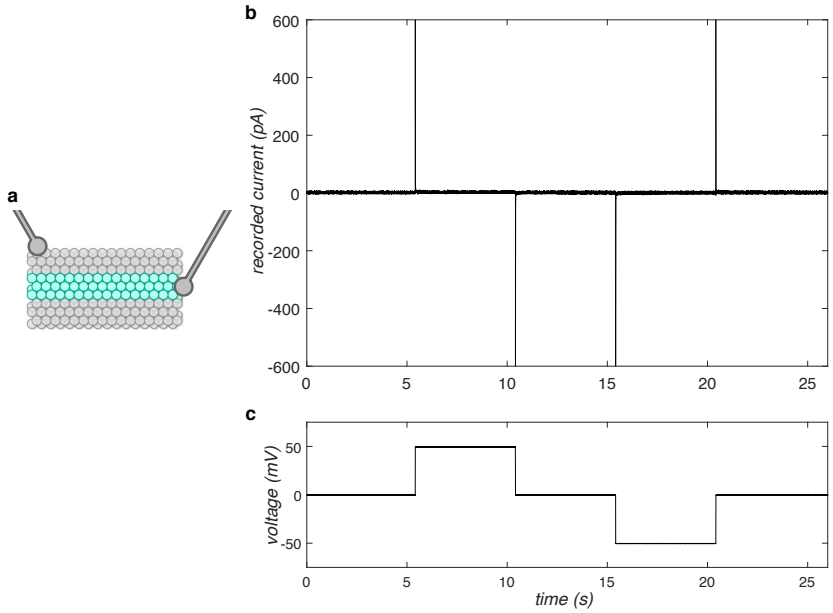

Fig. 7.11. Off-pathway ionic current in printed networks. **a**, Diagram demonstrating the positioning of the electrodes during recording. One of the two electrodes is positioned outside of the conductive droplet pathway (containing αHL, in teal), in contact with the non conductive droplets (in grey). **b-c**, Current trace (**b**) demonstrating a non-significant change in ionic current upon application of a potential of $\pm 50\,\mathrm{mV}$ (**c**).

7.2 Supplementary Tables

Linear Regression	
Slope	86.26 ± 5.704
Y-intercept when X=0.0	-13.70 ± 3.139
X-intercept when Y=0.0	0.1589
1/slope	0.01159
95% Confidence Intervals	
Slope	70.43 to 102.1
Y-intercept when X=0.0	-22.42 to -4.989
X-intercept when Y=0.0	0.06967 to 0.2233
Goodness of Fit	
R squared	0.9828
Sy.x	2.742
Is slope significantly non-zero?	
F	228.7
DFn, DFd	1.000, 4.000
P value	<0.0001
Deviation from zero?	Significant
Data	
Number of X values	6
Maximum number of Y replicates	1
Total number of values	6
Number of missing values	0
Equation	Y = 86.26*X - 13.70

Tab. 7.1. Dependence of θ_{DIB} on φ_{SIL}: Linear regression.

Linear Regression	
Slope	45.61 ± 1.773
Y-intercept when X=0.0	39.56 ± 1.041
X-intercept when Y=0.0	-0.8674
1/slope	0.02193
95% Confidence Intervals	
Slope	41.41 to 49.80
Y-intercept when X=0.0	37.10 to 42.02
X-intercept when Y=0.0	-1.009 to -0.7492
Goodness of Fit	
R squared	0.9895
Sy.x	1.644
Is slope significantly non-zero?	
F	661.4
DFn, DFd	1.000, 7.000
P value	<0.0001
Deviation from zero?	Significant
Data	
Number of X values	9
Maximum number of Y replicates	1
Total number of values	9
Number of missing values	0
Equation	Y = 45.61*X + 39.56

Tab. 7.2. Dependence of θ_{DIB} on x_{POPC}: Linear regression.

ANOVA table	**SS**	**DF**	**MS**	**F** (DFn, DFd)	**P value**
Treatment (between columns)	3.937	4	0.9841	F (4, 18) = 0.7648	P = 0.5618
Residual (within columns)	23.16	18	1.287		
Total	27.1	22			

Tab. 7.3. Dependence of θ_{DIB} on temperature: ANOVA table.

Tukey's multiple comparisons test	Mean Diff.	95% CI of diff.	Significant?	Summary
4.00 vs. 10.00	0.1259	-2.044 to 2.295	No	ns
4.00 vs. 22.00	0.391	-2.114 to 2.896	No	ns
4.00 vs. 37.00	1.081	-0.9958 to 3.158	No	ns
4.00 vs. 60.00	0.4236	-1.877 to 2.725	No	ns
10.00 vs. 22.00	0.2651	-2.240 to 2.770	No	ns
10.00 vs. 37.00	0.9554	-1.122 to 3.033	No	ns
10.00 vs. 60.00	0.2976	-2.003 to 2.599	No	ns
22.00 vs. 37.00	0.6903	-1.735 to 3.116	No	ns
22.00 vs. 60.00	0.03252	-2.587 to 2.652	No	ns
37.00 vs. 60.00	-0.6578	-2.872 to 1.556	No	ns

Tab. 7.4. Dependence of θ_{DIB} on temperature: Tukey's multiple comparisons test.

One phase decay - Best-fit values	
Y0	0
Plateau	42.04
K	5.037
Half Life	0.1376
Tau	0.1985
Span	-42.04
Std. Error	
Plateau	0.3978
K	0.1927
95% Confidence Intervals	
Plateau	41.22 to 42.86
K	4.640 to 5.434
Half Life	0.1276 to 0.1494
Tau	0.1840 to 0.2155
Goodness of Fit	
Degrees of Freedom	25
R squared	0.97
Absolute Sum of Squares	55.7
Sy.x	1.493
Constraints	
Y0	Y0 = 0.0
K	K >0.0
Number of points analysed	27

Tab. 7.5. Dependence of θ_{DIB} on lipid concentration: Non-linear regression.

Linear Regression	
Slope	-0.01174 ± 0.005849
Y-intercept when X=0.0	41.70 ± 0.6701
X-intercept when Y=0.0	3553
1/slope	-85.22
95% Confidence Intervals	
Slope	-0.03690 to 0.01343
Y-intercept when X=0.0	38.82 to 44.58
X-intercept when Y=0.0	1188 to +infinity
Goodness of Fit	
R squared	0.668
Sy.x	0.862
Is slope significantly non-zero?	
F	4.025
DFn, DFd	1.000, 2.000
P value	0.1827
Deviation from zero?	Not Significant
Data	
Number of X values	4
Maximum number of Y replicates	1
Total number of values	4
Number of missing values	0
Equation	Y = -0.01174*X + 41.70

Tab. 7.6. Dependence of θ_{DIB} on droplet volume: Linear regression.

Linear Regression	θ_{DIB} (on PMMA)	θ_{DIB} (on GLASS)
Slope	79.88 ± 3.169	73.27 ± 4.318
Y-intercept when X=0.0	-11.28 ± 1.744	-8.395 ± 2.345
X-intercept when Y=0.0	0.1412	0.1146
1/slope	0.01252	0.01365
95% Confidence Intervals		
Slope	71.08 to 88.67	59.53 to 87.01
Goodness of Fit		
R squared	0.9937	0.9897
Sy.x	1.523	2.048
Is slope significantly non-zero?		
F	635.4	287.9
DFn, DFd	1.000, 4.000	1.000, 3.000
P value	<0.0001	0.0004
Deviation from zero?	Significant	Significant
Data		
Number of X values	6	5
Maximum number of Y replicates	1	1
Total number of values	6	5
Number of missing values	0	1
Equation	Y = 79.88*X - 11.28	Y = 73.27*X - 8.395
Comparison of Slopes		
F	1.59061	
DFn, DFd	1, 7	
P value	0.2476	
Significant (alpha=0.05)?	No	
Pooled slope	76.618	
Comparison of intercepts		
F	0.172938	
DFn, DFd	1, 8	
P value	0.6884	
Significant (alpha=0.05)?	No	
Pooled intercept	-9.81533	

Tab. 7.7. Comparison between θ_{DIB} formed on plastic and on hydrophilic glass.

Linear Regression	θ_{DIB} (on GLASS)	θ_{glass}
Slope	73.27 ± 4.318	92.88 ± 9.672
Y-intercept when X=0.0	-8.395 ± 2.345	-1.052 ± 5.253
X-intercept when Y=0.0	0.1146	0.01133
1/slope	0.01365	0.01077
95% Confidence Intervals		
Slope	59.53 to 87.01	62.10 to 123.7
Goodness of Fit		
R squared	0.9897	0.9685
Sy.x	2.048	4.588
Is slope significantly non-zero?		
F	287.9	92.21
DFn, DFd	1.000, 3.000	1.000, 3.000
P value	0.0004	0.0024
Deviation from zero?	Significant	Significant
Data		
Number of X values	5	5
Maximum number of Y replicates	1	1
Total number of values	5	5
Number of missing values	1	1
Equation	Y = 73.27*X - 8.395	Y = 92.88*X - 1.052
Comparison of Slopes		
F	3.42628	
DFn, DFd	1, 6	
P value	0.1136	
Significant (alpha=0.05)?	No	
Pooled slope	83.0767	
Comparison of intercepts		
F	43.2398	
DFn, DFd	1, 7	
P value	0.0003	
Significant (alpha=0.05)?	Yes	

Tab. 7.8. Comparison between θ_{DIB} and θ_{glass}.

2D Linear Regression	
Equation	Z = (a*X + b*Y + c) / d
a	0.93
b	0.368
c	-0.236
d	0.009
R squared	0.9897

Tab. 7.9. Dependence of θ_{DIB} on φ_{SIL} and x_{POPC}: 2D-linear regression.

	φ_{SIL}	x_{POPC}	θ_{DIB} (calculated)
	0.52	0.18	35.43
c	0.52	0.2	36.26
	0.52	0.22	37.1
	0.54	0.13	35.45
	0.54	0.15	36.28
	0.54	0.17	37.12
	0.55	0.11	35.67
b	0.55	0.13	36.5
	0.55	0.16	37.76
	0.57	0.05	35.42
	0.57	0.07	36.26
	0.57	0.10	37.51
	0.59	0.00	35.29
a	0.6	0.00	36.35
	0.61	0.00	37.41

Tab. 7.10. Lipid and oil conditions used in Fig. 2.9a-c and 7.6.

Linear Regression	
Slope	96.08 ± 3.817
Y-intercept when X=0.0	-20.31 ± 2.295
X-intercept when Y=0.0	0.2114
1/slope	0.01041
95% Confidence Intervals	
Slope	87.67 to 104.5
Y-intercept when X=0.0	-25.36 to -15.26
X-intercept when Y=0.0	0.1740 to 0.2428
Goodness of Fit	
R squared	0.9829
Sy.x	0.5397
Is slope significantly non-zero?	
F	633.7
DFn, DFd	1.000, 11.00
P value	< 0.0001
Deviation from zero?	Significant
Data	
Number of X values	3
Maximum number of Y replicates	5
Total number of values	13
Number of missing values	2
Equation	Y = 96.08*X - 20.31

Tab. 7.11. Dependence of θ_{DIB} on φ_{SIL} for PEGDA droplet pairs: Linear regression.

ANOVA table	**SS**	**DF**	**MS**	**F** (DFn, DFd)	**P value**
Treatment (between columns)	0.1965	6	0.03276	F (6, 28) = 9.615	$P < 0.0001$
Residual (within columns)	0.09539	28	0.003407		
Total	0.2919	34			

Tab. 7.12. Hexagonal packing fraction in 3D-printed droplet networks: ANOVA table.

Tukey's multiple comparisons test	Mean Diff.	95% CI of diff.	Significant?	Summary
0.35 vs. 0.50	-0.07464	-0.2099 to 0.06058	No	ns
0.35 vs. 0.57	-0.06895	-0.2042 to 0.06626	No	ns
0.35 vs. 0.59	-0.127	-0.2580 to 0.003887	No	ns
0.35 vs. 0.60	0.02453	-0.1107 to 0.1597	No	ns
0.35 vs. 0.65	0.005412	-0.1298 to 0.1406	No	ns
0.35 vs. 0.80	0.1001	-0.03080 to 0.2310	No	ns
0.50 vs. 0.57	0.005688	-0.1114 to 0.1228	No	ns
0.50 vs. 0.59	-0.05239	-0.1645 to 0.05972	No	ns
0.50 vs. 0.60	0.09917	-0.01793 to 0.2163	No	ns
0.50 vs. 0.65	0.08005	-0.03705 to 0.1972	No	ns
0.50 vs. 0.80	0.1748	0.06265 to 0.2869	Yes	***
0.57 vs. 0.59	-0.05808	-0.1702 to 0.05403	No	ns
0.57 vs. 0.60	0.09348	-0.02362 to 0.2106	No	ns
0.57 vs. 0.65	0.07436	-0.04274 to 0.1915	No	ns
0.57 vs. 0.80	0.1691	0.05696 to 0.2812	Yes	***
0.59 vs. 0.60	0.1516	0.03945 to 0.2637	Yes	**
0.59 vs. 0.65	0.1324	0.02033 to 0.2446	Yes	*
0.59 vs. 0.80	0.2272	0.1203 to 0.3341	Yes	****
0.60 vs. 0.65	-0.01912	-0.1362 to 0.09798	No	ns
0.60 vs. 0.80	0.07559	-0.03652 to 0.1877	No	ns
0.65 vs. 0.80	0.09471	-0.01740 to 0.2068	No	ns

Tab. 7.13. Hexagonal packing fraction in 3D-printed droplet networks: Tukey's multiple comparisons test.

ANOVA table	SS	DF	MS	F (DFn, DFd)	P value
Treatment (between columns)	0.02826	6	0.00471	F (6, 28) = 2.149	P = 0.0789
Residual (within columns)	0.06136	28	0.002192		
Total	0.08962	34			

Tab. 7.14. Square packing fraction in 3D-printed droplet networks: ANOVA table.

Tukey's multiple comparisons test	Mean Diff.	95% CI of diff.	Significant?	Summary
0.35 vs. 0.50	-0.08942	-0.1979 to 0.01903	No	ns
0.35 vs. 0.57	-0.09579	-0.2042 to 0.01266	No	ns
0.35 vs. 0.59	-0.08307	-0.1881 to 0.02194	No	ns
0.35 vs. 0.60	-0.08702	-0.1955 to 0.02143	No	ns
0.35 vs. 0.65	-0.08486	-0.1933 to 0.02359	No	ns
0.35 vs. 0.80	-0.04125	-0.1463 to 0.06376	No	ns
0.50 vs. 0.57	-0.006374	-0.1003 to 0.08755	No	ns
0.50 vs. 0.59	0.006345	-0.08358 to 0.09627	No	ns
0.50 vs. 0.60	0.002394	-0.09153 to 0.09631	No	ns
0.50 vs. 0.65	0.004553	-0.08937 to 0.09847	No	ns
0.50 vs. 0.80	0.04817	-0.04175 to 0.1381	No	ns
0.57 vs. 0.59	0.01272	-0.07720 to 0.1026	No	ns
0.57 vs. 0.60	0.008768	-0.08515 to 0.1027	No	ns
0.57 vs. 0.65	0.01093	-0.08299 to 0.1048	No	ns
0.57 vs. 0.80	0.05454	-0.03538 to 0.1445	No	ns
0.59 vs. 0.60	-0.003952	-0.09387 to 0.08597	No	ns
0.59 vs. 0.65	-0.001793	-0.09171 to 0.08813	No	ns
0.59 vs. 0.80	0.04182	-0.04392 to 0.1276	No	ns
0.60 vs. 0.65	0.002159	-0.09176 to 0.09608	No	ns
0.60 vs. 0.80	0.04577	-0.04415 to 0.1357	No	ns
0.65 vs. 0.80	0.04361	-0.04631 to 0.1335	No	ns

Tab. 7.15. Square packing fraction in 3D-printed droplet networks: Tukey's multiple comparisons test.

ANOVA table	SS	DF	MS	F (DFn, DFd)	P value
Treatment (between columns)	0.2054	6	0.03424	F (6, 28) = 6.594	P = 0.0002
Residual (within columns)	0.1454	28	0.005192		
Total	0.3508	34			

Tab. 7.16. No packing fraction in 3D-printed droplet networks: ANOVA table.

Tukey's multiple comparisons test	Mean Diff.	95% CI of diff.	Significant?	Summary
0.35 vs. 0.50	0.2422	0.07529 to 0.4091	Yes	**
0.35 vs. 0.57	0.1721	0.005219 to 0.3391	Yes	*
0.35 vs. 0.59	0.2535	0.09189 to 0.4151	Yes	***
0.35 vs. 0.60	0.09672	-0.07021 to 0.2636	No	ns
0.35 vs. 0.65	0.2014	0.03446 to 0.3683	Yes	*
0.35 vs. 0.80	0.2384	0.07681 to 0.4001	Yes	**
0.50 vs. 0.57	-0.07007	-0.2146 to 0.07449	No	ns
0.50 vs. 0.59	0.0113	-0.1271 to 0.1497	No	ns
0.50 vs. 0.60	-0.1455	-0.2901 to -0.0009405	Yes	*
0.50 vs. 0.65	-0.04083	-0.1854 to 0.1037	No	ns
0.50 vs. 0.80	-0.003788	-0.1422 to 0.1346	No	ns
0.57 vs. 0.59	0.08137	-0.05704 to 0.2198	No	ns
0.57 vs. 0.60	-0.07543	-0.2200 to 0.06913	No	ns
0.57 vs. 0.65	0.02924	-0.1153 to 0.1738	No	ns
0.57 vs. 0.80	0.06629	-0.07212 to 0.2047	No	ns
0.59 vs. 0.60	-0.1568	-0.2952 to -0.01839	Yes	*
0.59 vs. 0.65	-0.05213	-0.1905 to 0.08628	No	ns
0.59 vs. 0.80	-0.01508	-0.1471 to 0.1169	No	ns
0.60 vs. 0.65	0.1047	-0.03989 to 0.2492	No	ns
0.60 vs. 0.80	0.1417	0.003307 to 0.2801	Yes	*
0.65 vs. 0.80	0.03705	-0.1014 to 0.1755	No	ns

Tab. 7.17. No packing fraction in 3D-printed droplet networks: Tukey's multiple comparisons test.

ANOVA table	SS	DF	MS	F (DFn, DFd)	P value
Treatment (between columns)	0.05593	6	0.009321	F (6, 28) = 30.86	P <0.0001
Residual (within columns)	0.008457	28	0.000302		
Total	0.06438	34			

Tab. 7.18. Oil inclusions in 3D-printed droplet networks: ANOVA table.

Tukey's multiple comparisons test	Mean Diff.	95% CI of diff.	Significant?	Summary
0.35 vs. 0.50	0.08539	0.04513 to 0.1257	Yes	****
0.35 vs. 0.57	0.1334	0.09312 to 0.1736	Yes	****
0.35 vs. 0.59	0.1236	0.08463 to 0.1626	Yes	****
0.35 vs. 0.60	0.07034	0.03008 to 0.1106	Yes	***
0.35 vs. 0.65	0.0948	0.05454 to 0.1351	Yes	****
0.35 vs. 0.80	0.1436	0.1047 to 0.1826	Yes	****
0.50 vs. 0.57	0.04799	0.01312 to 0.08285	Yes	**
0.50 vs. 0.59	0.03823	0.004846 to 0.07161	Yes	*
0.50 vs. 0.60	-0.01505	-0.04991 to 0.01982	No	ns
0.50 vs. 0.65	0.009409	-0.02546 to 0.04428	No	ns
0.50 vs. 0.80	0.05825	0.02487 to 0.09163	Yes	***
0.57 vs. 0.59	-0.009759	-0.04314 to 0.02362	No	ns
0.57 vs. 0.60	-0.06303	-0.09790 to -0.02817	Yes	****
0.57 vs. 0.65	-0.03858	-0.07345 to -0.003711	Yes	*
0.57 vs. 0.80	0.01026	-0.02312 to 0.04364	No	ns
0.59 vs. 0.60	-0.05327	-0.08666 to -0.01989	Yes	***
0.59 vs. 0.65	-0.02882	-0.06220 to 0.004563	No	ns
0.59 vs. 0.80	0.02002	-0.01181 to 0.05185	No	ns
0.60 vs. 0.65	0.02445	-0.01041 to 0.05932	No	ns
0.60 vs. 0.80	0.07329	0.03991 to 0.1067	Yes	****
0.65 vs. 0.80	0.04884	0.01546 to 0.08222	Yes	**

Tab. 7.19. Oil inclusions in 3D-printed droplet networks: Tukey's multiple comparisons test.

ANOVA table	SS	DF	MS	F (DFn, DFd)	P value
Treatment (between columns)	0.117	2	0.0585	F (2, 10) = 15.74	P = 0.0008
Residual (within columns)	0.03716	10	0.003716		
Total	0.1542	12			

Tab. 7.20. Effect of DIB formation kinetics on the hexagonal packing fraction: ANOVA table.

Tukey's multiple comparisons test	Mean Diff.	95% CI of diff.	Significant?	Summary
cyan vs. purple	-0.1683	-0.2740 to -0.06258	Yes	**
cyan vs. magenta	0.05737	-0.06467 to 0.1794	No	ns
purple vs. magenta	0.2256	0.1036 to 0.3477	Yes	**

Tab. 7.21. Effect of DIB formation kinetics on the hexagonal packing fraction: Tukey's multiple comparisons test.

ANOVA table	SS	DF	MS	F (DFn, DFd)	P value
Treatment (between columns)	0.09743	2	0.04872	F (2, 9) = 15.04	P = 0.0013
Residual (within columns)	0.02915	9	0.003239		
Total	0.1266	11			

Tab. 7.22. Effect of printing speed on the hexagonal packing fraction: ANOVA table.

Tukey's multiple comparisons test	Mean Diff.	95% CI of diff.	Significant?	Summary
0.25 vs. 0.5	-0.1564	-0.2724 to -0.04033	Yes	*
0.25 vs. 2	0.04136	-0.08000 to 0.1627	No	ns
0.5 vs. 2	0.1977	0.09114 to 0.3043	Yes	**

Tab. 7.23. Effect of printing speed on the hexagonal packing fraction: Tukey's multiple comparisons test.

ANOVA table	SS	DF	MS	F (DFn, DFd)	P value
Treatment (between columns)	0.06295	2	0.03148	F (2, 12) = 11.50	P = 0.0016
Residual (within columns)	0.03283	12	0.002736		
Total	0.09579	14			

Tab. 7.24. Effect of DIB formation kinetics on the hexagonal packing fraction (Fig. 7.6a): ANOVA table.

Tukey's multiple comparisons test	Mean Diff.	95% CI of diff.	Significant?	Summary
35.4° vs. 36.3°	0.116	0.03147 to 0.2005	Yes	**
35.4° vs. 37.4°	0.1474	0.05727 to 0.2374	Yes	**
36.3° vs. 37.4°	0.03138	-0.06224 to 0.1250	No	ns

Tab. 7.25. Effect of DIB formation kinetics on the hexagonal packing fraction (Fig. 7.6a): Tukey's multiple comparisons test.

ANOVA table	SS	DF	MS	F (DFn, DFd)	P value
Treatment (between columns)	0.1137	2	0.05685	F (2, 10) = 18.40	P = 0.0004
Residual (within columns)	0.03089	10	0.003089		
Total	0.1446	12			

Tab. 7.26. Effect of DIB formation kinetics on the hexagonal packing fraction (Fig. 7.6b): ANOVA table.

Tukey's multiple comparisons test	Mean Diff.	95% CI of diff.	Significant?	Summary
35.4° vs. 36.3°	-0.02494	-0.1362 to 0.08633	No	ns
35.4° vs. 37.4°	0.1757	0.06438 to 0.2869	Yes	**
36.3° vs. 37.4°	0.2006	0.1042 to 0.2970	Yes	***

Tab. 7.27. Effect of DIB formation kinetics on the hexagonal packing fraction (Fig. 7.6b): Tukey's multiple comparisons test.

ANOVA table	SS	DF	MS	F (DFn, DFd)	P value
Treatment (between columns)	0.04258	2	0.02129	F (2, 12) = 4.097	P = 0.0440
Residual (within columns)	0.06235	12	0.005196		
Total	0.1049	14			

Tab. 7.28. Effect of DIB formation kinetics on the hexagonal packing fraction (Fig. 7.6c): ANOVA table.

Tukey's multiple comparisons test	Mean Diff.	95% CI of diff.	Significant?	Summary
35.4° vs. 36.3°	0.118	-0.006102 to 0.2422	No	ns
35.4° vs. 37.4°	0.01845	-0.1106 to 0.1475	No	ns
36.3° vs. 37.4°	-0.09958	-0.2160 to 0.01687	No	ns

Tab. 7.29. Effect of DIB formation kinetics on the hexagonal packing fraction (Fig. 7.6c): Tukey's multiple comparisons test.

Unpaired t test with Welch's correction	
P value	0.0057
P value summary	**
Significantly different? (P <0.05)	Yes
One- or two-tailed P value?	Two-tailed
Welch-corrected t, df	t=3.397 df=11.30
How big is the difference?	
Mean ± SEM of column A	27.03 ± 0.1722 N=7
Mean ± SEM of column B	27.99 ± 0.2221 N=7
Difference between means	0.9549 ± 0.2811
95% confidence interval	0.3382 to 1.571
R squared	0.5053
F test to compare variances	
F,DFn, Dfd	1.663, 6, 6
P value	0.5522
P value summary	ns
Significantly different? (P < 0.05)	No

Tab. 7.30. Precision in θ_{DIB} over small increments in φ_{SIL}.

			Hexagonal		Square		Amorphous		No Packing	
φ_{SIL}	θ_{DIB}	n	average	st. dev.	average	st. dev.	average	st. dev.	average	st. dev.
0.35	9.9	3	0.28	0.08	0.08	0.03	0.10	0.02	0.53	0.08
0.50	25.8	5	0.37	0.03	0.17	0.05	0.18	0.04	0.26	0.07
0.57	33.2	5	0.36	0.06	0.17	0.05	0.10	0.02	0.34	0.03
0.59	35.3	6	0.43	0.06	0.16	0.06	0.14	0.04	0.25	0.06
0.60	36.3	5	0.31	0.05	0.17	0.04	0.16	0.04	0.33	0.07
0.65	41.6	5	0.28	0.04	0.16	0.02	0.22	0.05	0.31	0.06
0.80	57.5	6	0.17	0.06	0.12	0.04	0.40	0.05	0.27	0.11

Tab. 7.31. Packing fractions in 3D-printed droplet networks - effect of φ_{SIL}.

			Hexagonal		Square		Amorphous		No Packing	
φ_{SIL}	θ_{DIB}	n	average	st. dev.	average	st. dev.	average	st. dev.	average	st. dev.
0.59	0.00	6	0.43	0.06	0.16	0.06	0.14	0.04	0.25	0.06
0.60	0.00	5	0.31	0.05	0.17	0.04	0.16	0.04	0.33	0.07
0.61	0.00	4	0.28	0.05	0.15	0.07	0.19	0.03	0.36	0.03
0.55	0.11	3	0.47	0.01	0.14	0.04	0.17	0.03	0.20	0.02
0.55	0.13	5	0.50	0.07	0.11	0.03	0.12	0.04	0.25	0.07
0.55	0.16	5	0.30	0.06	0.16	0.05	0.14	0.04	0.38	0.07
0.52	0.18	4	0.40	0.04	0.10	0.03	0.15	0.02	0.33	0.03
0.52	0.20	6	0.28	0.08	0.12	0.03	0.17	0.02	0.40	0.09
0.52	0.23	5	0.38	0.08	0.14	0.03	0.14	0.04	0.32	0.05

Tab. 7.32. Packing fractions in 3D-printed droplet networks - effect of DIB formation kinetics.

				Hexagonal		Square		Amorphous		No Packing	
φ_{SIL}	θ_{DIB}	f_{drop}	n	av.	st. dev.	av.	st. dev.	av.	st. dev.	av.	st. dev.
0.60	0.00	2.00	4	0.28	0.05	0.15	0.03	0.19	0.04	0.36	0.03
0.60	0.00	0.50	5	0.31	0.05	0.17	0.04	0.16	0.04	0.33	0.07
0.60	0.00	0.25	3	0.33	0.08	0.11	0.04	0.17	0.05	0.37	0.02
0.55	0.13	2.00	3	0.22	0.03	0.08	0.01	0.28	0.06	0.40	0.09
0.55	0.13	0.50	5	0.50	0.07	0.11	0.03	0.12	0.04	0.25	0.07
0.55	0.13	0.25	4	0.17	0.05	0.11	0.02	0.26	0.09	0.43	0.14
0.52	0.20	2.00	3	0.29	0.06	0.16	0.02	0.25	0.04	0.27	0.02
0.52	0.20	0.50	6	0.28	0.08	0.12	0.03	0.17	0.02	0.40	0.09
0.52	0.20	0.25	5	0.16	0.04	0.16	0.04	0.21	0.04	0.43	0.09

Tab. 7.33. Packing fractions in 3D-printed droplet networks - effect of printing speed.

			θ_{DIB}	
φ_{SIL}	x_{POPC}	n	average	st. dev.
0.20	0.00	3	6.03	0.75
0.35	0.00	4	16.32	0.34
0.50	0.00	6	26.52	1.68
0.57	0.00	3	34.61	0.93
0.65	0.00	6	41.86	1.34
0.80	0.00	4	58.56	1.81
0.65	0.20	6	48.42	0.46
0.65	0.25	4	49.57	0.94
0.65	0.33	5	53.77	3.76
0.65	0.50	5	61.42	3.17
0.65	0.66	4	68.17	0.99
0.65	0.75	3	73.54	0.59
0.65	0.80	4	78.82	0.98
0.65	1.00	1	85.25	-

Tab. 7.34. List of conditions and measured θ_{DIB} in droplet pairs (Fig. 2.2f-g).

Linear Regression	
Slope	88.27 ± 4.722
Y-intercept when X=0.0	-2.602 ± 2.269
X-intercept when Y=0.0	0.02948
1/slope	0.01133
95% Confidence Intervals	
Slope	77.75 to 98.79
Y-intercept when X=0.0	-7.657 to 2.453
X-intercept when Y=0.0	-0.03150 to 0.07762
Goodness of Fit	
R squared	0.9722
Sy.x	1.181
Is slope significantly non-zero?	
F	349.4
DFn, DFd	1.000, 10.00
P value	<0.0001
Deviation from zero?	Significant
Data	
Number of X values	3
Maximum number of Y replicates	5
Total number of values	12
Number of missing values	3
Equation	Y = 88.27*X - 2.602

Tab. 7.35. Dependence of θ_{DIB} on φ_{SIL} for droplets containing 1 M NaCl in Tris-HCl buffer: Linear regression.

7.3 Supplementary Code

7.3.1 MATLAB code for contact angle measurement

```
inFile = 'filename.tif';
verbose = true;

img = imread(inFile);

[centres,radii,metric] = imfindcircles(max(img(:))-img,
                         [250,560],'Sensitivity',0.97);

if size(centres,1) == 2
    L = pdist(centres);
    R1 = radii(1);
    R2 = radii(2);
    contactAngle = acos(((L*L) - (R1*R1) - (R2*R2))/(2*R1*R1));

elseif size(centres,1) > 2
    warning('Number of droplets detected is greater than 2.
             Using closest pair...');
    dists = pdist2(centres,centres);

    for i = 1:size(dists,1)
        dists(i,i) = NaN;
    end

    [L,minInd] = min(dists(:));
    [circle1,circle2] = ind2sub(size(dists),minInd);
    R1 = radii(circle1);
    R2 = radii(circle2);
    contactAngle = acos(((L*L) - (R1*R1) - (R2*R2))/(2*R1*R1));

elseif size(centres,1) < 2
```

```
    warning('Number of droplets detected is less than 2. Skipping...');

    contactAngle = NaN;
end

if verbose
    imshow(img,[]);
    viscircles(centres,radii,'EdgeColor','r');
end

contactAngleDeg = rad2deg(contactAngle)/2;
```

Bibliography

1. Bell, G. & Mooers, A. O. Size and complexity among multicellular organisms. *Biol. J. Linn. Soc.* **60,** 345–363 (1997).

2. Grosberg, R. K. & Strathmann, R. R. The Evolution of Multicellularity: A Minor Major Transition? *Annu. Rev. Ecol. Evol. Syst.* **38,** 621–654 (2007).

3. Szathmáry, E. & Smith, J. M. The major evolutionary transitions. *Nature* **374,** 227–232 (1995).

4. Noireaux, V., Maeda, Y. T. & Libchaber, A. Development of an artificial cell, from self-organization to computation and self-reproduction. *Proc. Natl. Acad. Sci. U. S. A.* **108,** 3473–3480 (2011).

5. Blain, J. C. & Szostak, J. W. Progress Toward Synthetic Cells. *Annu. Rev. Biochem.* (2014).

6. Spoelstra, W. K., Deshpande, S. & Dekker, C. Tailoring the appearance: what will synthetic cells look like? *Curr. Opin. Biotechnol.* **51,** 47–56 (2018).

7. Yeh Martín, N., Valer, L. & Mansy, S. S. Toward long-lasting artificial cells that better mimic natural living cells. *Emerg. Top. Life Sci.* (2019).

8. Mantri, S. & Tanuj Sapra, K. Evolving protocells to prototissues: Rational design of a missing link. *Biochem. Soc. Trans.* **41,** 1159–1165 (2013).

9. Booth, M. J., Restrepo Schild, V., Downs, F. G. & Bayley, H. Functional aqueous droplet networks. *Mol. Biosyst.* **13,** 1658–1691 (2017).

10. Holden, M. A., Needham, D. & Bayley, H. Functional Bionetworks from Nanoliter Water Droplets. *J. Am. Chem. Soc.* **129,** 8650–8655 (2007).

11. Hwang, W. L., Chen, M., Cronin, B., Holden, M. A. & Bayley, H. Asymmetric droplet interface bilayers. *J. Am. Chem. Soc.* **130,** 5878–5879 (2008).

12. Bayley, H., Cronin, B., Heron, A., *et al.* Droplet interface bilayers. *Mol. Biosyst.* **4,** 1191 (2008).

13.Maglia, G., Heron, A. J., Hwang, W. L., *et al.* Droplet networks with incorporated protein diodes show collective properties. *Nat. Nanotechnol.* **4,** 437–440 (2009).

14.Yasuga, H., Kawano, R., Takinoue, M., *et al.* Logic Gate Operation by DNA Translocation through Biological Nanopores. *PLoS One* **11,** e0149667 (2016).

15.Bai, Y., He, X., Liu, D., *et al.* A double droplet trap system for studying mass transport across a droplet-droplet interface. *Lab Chip* **10,** 1281–1285 (2010).

16.Carreras, P., Elani, Y., Law, R. V., *et al.* A microfluidic platform for size-dependent generation of droplet interface bilayer networks on rails. *Biomicrofluidics* **9,** 064121 (2015).

17.Thutupalli, S. & Herminghaus, S. Tuning active emulsion dynamics via surfactants and topology. *Eur. Phys. J. E* **36,** 91 (2013).

18.Jones, G., King, P. H., Morgan, H., De Planque, M. R. & Zauner, K. P. Autonomous droplet architectures. *Artif. Life* **21,** 195–204 (2015).

19.Syeda, R., Holden, M. A., Hwang, W. L. & Bayley, H. Screening blockers against a potassium channel with a droplet interface bilayer array. *J. Am. Chem. Soc.* **130,** 15543–15548 (2008).

20.Booth, M. J., Schild, V. R., Graham, A. D., Olof, S. N. & Bayley, H. Light-activated communication in synthetic tissues. *Sci. Adv.* **2,** e1600056 (2016).

21.Sarles, S. A. & Leo, D. J. Regulated attachment method for reconstituting lipid bilayers of prescribed size within flexible substrates. *Anal. Chem.* **82,** 959–966 (2010).

22.Sarles, S. A. & Leo, D. J. Physical encapsulation of droplet interface bilayers for durable, portable biomolecular networks. *Lab Chip* **10,** 710–717 (2010).

23.Elani, Y., DeMello, A. J., Niu, X. & Ces, O. Novel technologies for the formation of 2-D and 3-D droplet interface bilayer networks. *Lab Chip* **12,** 3514 (2012).

24.Wauer, T., Gerlach, H., Mantri, S., *et al.* Construction and Manipulation of Functional Three-Dimensional Droplet Networks. *ACS Nano* **8,** 771–779 (2014).

25.Friddin, M. S., Bolognesi, G., Elani, Y., *et al.* Optically assembled droplet interface bilayer (OptiDIB) networks from cell-sized microdroplets. *Soft Matter* **12,** 7731–7734 (2016).

26.Villar, G., Graham, A. D. & Bayley, H. A tissue-like printed material. *Science* **340,** 48–52 (2013).

27.Stanley, C. E., Elvira, K. S., Niu, X. Z., *et al.* A microfluidic approach for high-throughput droplet interface bilayer (DIB) formation. *Chem. Commun.* **46,** 1620–1622 (2010).

28.Zagnoni, M. & Cooper, J. M. A microdroplet-based shift register. *Lab Chip* **10,** 3069–3073 (2010).

29.Schlicht, B. & Zagnoni, M. Droplet-interface-bilayer assays in microfluidic passive networks. *Sci. Rep.* **5,** 9951 (2015).

30.Czekalska, M. A., Kaminski, T. S., Jakiela, S., *et al.* A droplet microfluidic system for sequential generation of lipid bilayers and transmembrane electrical recordings. *Lab Chip* **15,** 541–548 (2015).

31.Graham, A. D., Olof, S. N., Burke, M. J., *et al.* High-Resolution Patterned Cellular Constructs by Droplet-Based 3D Printing. *Sci. Rep.* **7,** 7004 (2017).

32.Villar, G., Heron, A. J. & Bayley, H. Formation of droplet networks that function in aqueous environments. *Nat. Nanotechnol.* **6,** 803–808 (2011).

33.Elani, Y., Solvas, X. C. I., Edel, J. B., Law, R. V. & Ces, O. Microfluidic generation of encapsulated droplet interface bilayer networks (multisomes) and their use as cell-like reactors. *Chem. Commun.* **52,** 5961–5964 (2016).

34.Deng, N.-N., Yelleswarapu, M. & Huck, W. T. S. Monodisperse Uni- and Multicompartment Liposomes. *J. Am. Chem. Soc.* **138,** 7584–7591 (2016).

35.Baxani, D. K., Morgan, A. J., Jamieson, W. D., *et al.* Bilayer Networks within a Hydrogel Shell: A Robust Chassis for Artificial Cells and a Platform for Membrane Studies. *Angew. Chemie - Int. Ed.* **55,** 14240–14245 (2016).

36.Bayoumi, M., Bayley, H., Maglia, G. & Sapra, K. T. Multi-compartment encapsulation of communicating droplets and droplet networks in hydrogel as a model for artificial cells. *Sci. Rep.* **7,** 45167 (2017).

37.Elani, Y., Gee, A., Law, R. V. & Ces, O. Engineering multi-compartment vesicle networks. *Chem. Sci.* **4,** 3332 (2013).

38.Elani, Y., Law, R. V. & Ces, O. Vesicle-based artificial cells as chemical microreactors with spatially segregated reaction pathways. *Nat. Commun.* **5,** 5305 (2014).

39.Elani, Y., Law, R. V. & Ces, O. Protein synthesis in artificial cells: Using compartmentalisation for spatial organisation in vesicle bioreactors. *Phys. Chem. Chem. Phys.* **17,** 15534–15537 (2015).

40.Walde, P., Wick, R., Fresta, M., Mangone, A. & Luisi, P. L. Autopoietic Self-Reproduction of Fatty Acid Vesicles. *J. Am. Chem. Soc.* **116,** 11649–11654 (1994).

41.Vriezema, D. M., Garcia, P. M., Sancho Oltra, N., *et al.* Positional assembly of enzymes in polymersome nanoreactors for cascade reactions. *Angew. Chemie - Int. Ed.* **46,** 7378–7382 (2007).

42.Mason, A. F., Buddingh, B. C., Williams, D. S. & Van Hest, J. C. Hierarchical Self-Assembly of a Copolymer-Stabilized Coacervate Protocell. *J. Am. Chem. Soc.* **139,** 17309–17312 (2017).

43.Van Nies, P., Westerlaken, I., Blanken, D., *et al.* Self-replication of DNA by its encoded proteins in liposome-based synthetic cells. *Nat. Commun.* **9,** 1–12 (2018).

44.Oberholzer, T., Nierhaus, K. H. & Luisi, P. L. Protein expression in liposomes. *Biochem. Biophys. Res. Commun.* **261,** 238–241 (1999).

45.Murtas, G., Kuruma, Y., Bianchini, P., Diaspro, A. & Luisi, P. L. Protein synthesis in liposomes with a minimal set of enzymes. *Biochem. Biophys. Res. Commun.* **363,** 12–17 (2007).

46.Steinkühler, J., Knorr, R. L., Zhao, Z., *et al.* Controlled division of cell-sized vesicles by low densities of membrane-bound proteins. *Nat. Commun.* **11,** 905 (2020).

47.Lentini, R., Martín, N. Y., Forlin, M., *et al.* Two-Way Chemical Communication between Artificial and Natural Cells. *ACS Cent. Sci.* **3,** 117–123 (2017).

48.Rampioni, G., D'Angelo, F., Messina, M., *et al.* Synthetic cells produce a quorum sensing chemical signal perceived by: Pseudomonas aeruginosa. *Chem. Commun.* **54,** 2090–2093 (2018).

49.Tang, T.-Y. Y., Cecchi, D., Fracasso, G., *et al.* Gene-Mediated Chemical Communication in Synthetic Protocell Communities. *ACS Synth. Biol.* **7,** 339–346 (2018).

50.Peters, R. J. R. W., Marguet, M., Marais, S., *et al.* Cascade Reactions in Multicompartmentalized Polymersomes. *Angew. Chemie* **126,** 150–154 (2014).

51.Deng, N.-N. & Huck, W. T. Microfluidic Formation of Monodisperse Coacervate Organelles in Liposomes. *Angew. Chemie - Int. Ed.* (2017).

52.Deshpande, S., Brandenburg, F., Lau, A., *et al.* Spatiotemporal control of coacervate formation within liposomes. *Nat. Commun.* **10** (2019).

53.Niederholtmeyer, H., Chaggan, C. & Devaraj, N. K. Communication and quorum sensing in non-living mimics of eukaryotic cells. *Nat. Commun.* **9,** 1–8 (2018).

54.Adamala, K. P., Martin-Alarcon, D. A., Guthrie-Honea, K. R. & Boyden, E. S. Engineering genetic circuit interactions within and between synthetic minimal cells. *Nat. Chem.* **9,** 431–439 (2017).

55.Gobbo, P., Patil, A. J., Li, M., *et al.* Programmed assembly of synthetic protocells into thermoresponsive prototissues. *Nat. Mater.* **17,** 1145–1153 (2018).

56.Thiam, A. R., Bremond, N. & Bibette, J. From Stability to Permeability of Adhesive Emulsion Bilayers. *Langmuir* **28,** 6291–6298 (2012).

57.Dupin, A. & Simmel, F. C. Signalling and differentiation in emulsion-based multi-compartmentalized in vitro gene circuits. *Nat. Chem.* **11,** 32–39 (2019).

58.Booth, M. J., Restrepo Schild, V., Box, S. J. & Bayley, H. Light-patterning of synthetic tissues with single droplet resolution. *Sci. Rep.* **7,** 9315 (2017).

59.Motta, P. M. The Three-Dimensional Microanatomy of the Liver. *Arch. Histol. Cytol.* **47,** 1–30 (1984).

60.Princen, H., Aronson, M. & Moser, J. Highly concentrated emulsions. II. Real systems. The effect of film thickness and contact angle on the volume fraction in creamed emulsions. *J. Colloid Interface Sci.* **75,** 246–270 (1980).

61.Aronson, M. P. & Princen, H. M. Contact angles associated with thin liquid films in emulsions. *Nature* **286,** 370–372 (1980).

62.Princen, H. Geometry of clusters of strongly coagulated fluid drops and the occurrence of collapsed Plateau borders. *Colloids and Surfaces* **9,** 47–66 (1984).

63.Schrader, M. E. Young-Dupre Revisited. *Langmuir* **11,** 3585–3589 (1995).

64.Dupré, A. Théorie mécanique de la chaleur, *Gauthier Villars* (1869).

65.Young, T. III. An essay on the cohesion of fluids. *Philos. Trans. R. Soc. London* **95,** 65–87 (1805).

66.Yanagisawa, M., Yoshida, T.-A., Furuta, M., Nakata, S. & Tokita, M. Adhesive force between paired microdroplets coated with lipid monolayers. *Soft Matter* **9,** 5891 (2013).

67.Poulin, P. & Bibette, J. Adhesion of Water Droplets in Organic Solvent. *Langmuir* **14,** 6341–6343 (1998).

68.Hughes, L. D., Rawle, R. J. & Boxer, S. G. Choose your label wisely: Water-soluble fluorophores often interact with lipid bilayers. *PLoS One* **9** (2014).

69.Lindeberg, T. Edge Detection and Ridge Detection with Automatic Scale Selection. *Int. J. Comput. Vis.* **30,** 117–154 (1998).

70.Lee, D. T. & Schachter, B. J. Two algorithms for constructing a Delaunay triangulation. *Int. J. Comput. Inf. Sci.* **9,** 219–242 (1980).

71.Steinhaus, H. Mathematical snapshots. *Dover Publications* (1999).

72.Wilson, T. & Tan, J. B. Three dimensional image reconstruction in conventional and confocal microscopy. *Bioimaging* **1,** 176–184 (1993).

73.Fan, J., Kim, S. H., Chen, Z., *et al.* Creation of Faceted Polyhedral Microgels from Compressed Emulsions. *Small* **13,** 1701256 (2017).

74.Campbell, I., Bourell, D. & Gibson, I. Additive manufacturing: rapid prototyping comes of age. *Rapid Prototyp. J.* **18,** 255–258 (2012).

75.Schilling, M. A. Toward a general modular systems theory and its application to interfirm product modularity. *Acad. Manag. Rev.* **25,** 312–334 (2000).

76.Carliss Y. B. and Kim B. C. Design Rules, Volume 1: The Power of Modularity. *MIT Press* (2000).

77.Birnbaum, K. D. & Alvarado, A. S. Slicing across Kingdoms: Regeneration in Plants and Animals. *Cell* **132,** 697–710 (2008).

78.Diesendruck, C. E., Sottos, N. R., Moore, J. S. & White, S. R. Biomimetic Self-Healing. *Angew. Chemie Int. Ed.* **54,** 10428–10447 (2015).

79.Slade, P. G. Electrical contacts: Principles and applications, second edition. *CRC Press* (2017).

80.Ozcelik, A., Rufo, J., Guo, F., *et al.* Acoustic tweezers for the life sciences. *Nat. Methods* **15,** 1021–1028 (2018).

81.Mugele, F. & Baret, J.-C. Electrowetting: from basics to applications. *J. Phys. Condens. Matter* **17,** R705–R774 (2005).

82.Sapra, K. T. & Bayley, H. Lipid-coated hydrogel shapes as components of electrical circuits and mechanical devices. *Sci. Rep.* **2,** 848 (2012).

83.Schild, V. R., Booth, M. J., Box, S. J., *et al.* Light-Patterned Current Generation in a Droplet Bilayer Array. *Sci. Rep.* (2017).

84.Schulz, M., Olubummo, A. & Binder, W. H. Beyond the lipid-bilayer: Interaction of polymers and nanoparticles with membranes. *Soft Matter* **8,** 4849–4864 (2012).

85.Deshpande, S., Caspi, Y., Meijering, A. E. C. & Dekker, C. Octanol-assisted liposome assembly on chip. *Nat. Commun.* **7,** 10447 (2016).

86.Dimova, R., Aranda, S., Bezlyepkina, N., *et al.* A practical guide to giant vesicles. Probing the membrane nanoregime via optical microscopy. *J. Phys. Condens. Matter* **18,** S1151–S1176 (2006).

87.Alberts, B., Johnson, A., Lewis, J., *et al.* Molecular Biology of the Cell. *Garland Science* (2017).

88.Krapf, D. Compartmentalization of the plasma membrane. *Curr. Opin. Cell Biol.* **53,** 15–21 (2018).

89.Gabaldón, T. & Pittis, A. A. Origin and evolution of metabolic sub-cellular compartmentalization in eukaryotes. *Biochimie* **119,** 262–268 (2015).

90.Hyman, A. A., Weber, C. A. & Jülicher, F. Liquid-Liquid Phase Separation in Biology. *Annu. Rev. Cell Dev. Biol.* **30,** 39–58 (2014).

91.Banani, S. F., Lee, H. O., Hyman, A. A. & Rosen, M. K. Biomolecular condensates: Organizers of cellular biochemistry. *Nat. Rev. Mol. Cell Biol.* **18,** 285–298 (2017).

92.Boisvert, F. M., Van Koningsbruggen, S., Navascués, J. & Lamond, A. I. The multifunctional nucleolus. *Nat. Rev. Mol. Cell Biol.* **8,** 574–585 (2007).

93.Mahen, R. & Venkitaraman, A. R. Pattern formation in centrosome assembly. *Curr. Opin. Cell Biol.* **24,** 14–23 (2012).

94.Buchan, J. R. & Parker, R. Eukaryotic Stress Granules: The Ins and Outs of Translation. *Mol. Cell* **36,** 932–941 (2009).

95.Decker, C. J. & Parker, R. P-bodies and stress granules: Possible roles in the control of translation and mRNA degradation. *Cold Spring Harb. Perspect. Biol.* **4** (2012).

96.Crosby, J., Treadwell, T., Hammerton, M., *et al.* Stabilization and enhanced reactivity of actinorhodin polyketide synthase minimal complex in polymer-nucleotide coacervate droplets. *Chem. Commun.* **48,** 11832–11834 (2012).

97.Strulson, C. A., Molden, R. C., Keating, C. D. & Bevilacqua, P. C. RNA catalysis through compartmentalization. *Nat. Chem.* **4,** 941–946 (2012).

98.Sokolova, E., Spruijt, E., Hansen, M. M. K., *et al.* Enhanced transcription rates in membrane-free protocells formed by coacervation of cell lysate. *Proc. Natl. Acad. Sci. U. S. A.* **110,** 11692–11697 (2013).

99.Nott, T. J., Craggs, T. D. & Baldwin, A. J. Membraneless organelles can melt nucleic acid duplexes and act as biomolecular filters. *Nat. Chem.* **8,** 569–575 (2016).

100.Tang, T. Y. D., Antognozzi, M., Vicary, J. A., Perriman, A. W. & Mann, S. Small-molecule uptake in membrane-free peptide/nucleotide protocells. *Soft Matter* **9,** 7647–7656 (2013).

101.Beck, M., Schmidt, A., Malmstroem, J., *et al.* The quantitative proteome of a human cell line. *Mol. Syst. Biol.* **7,** 549 (2011).

102.Mitsui, Y. & Schneider, E. L. Relationship between cell replication and volume in senescent human diploid fibroblasts. *Mech. Ageing Dev.* **5,** 45–56 (1976).

103.Heron, A. J., Thompson, J. R., Mason, A. E. & Wallace, M. I. Direct detection of membrane channels from gels using water-in-oil droplet bilayers. *J. Am. Chem. Soc.* **129,** 16042–16047 (2007).

104.Heng, B. C., Aubel, D. & Fussenegger, M. Prosthetic gene networks as an alternative to standard pharmacotherapies for metabolic disorders. *Curr. Opin. Biotechnol.* **35,** 37–45 (2015).

105.Rössger, K., Hamri, G. C. E. & Fussenegger, M. Reward-based hypertension control by a synthetic brain-dopamine interface. *Proc. Natl. Acad. Sci. U. S. A.* **110,** 18150–18155 (2013).

106.Kemmer, C., Gitzinger, M., Daoud-El Baba, M., *et al.* Self-sufficient control of urate homeostasis in mice by a synthetic circuit. *Nat. Biotechnol.* **28,** 355–360 (2010).

107.Rössger, K., Charpin-El-Hamri, G. & Fussenegger, M. A closed-loop synthetic gene circuit for the treatment of diet-induced obesity in mice. *Nat. Commun.* **4** (2013).

108.Ausländer, D., Ausländer, S., Charpin-El Hamri, G., *et al.* A synthetic multifunctional mammalian pH sensor and CO2 transgene-control device. *Mol. Cell* **55,** 397–408 (2014).

109.Ku, H. Notes on the use of propagation of error formulas. *J. Res. Natl. Bur. Stand. Sect. C Eng. Instrum.* **70C,** 263 (1966).

List of Figures

List of Tables

Declaration

This thesis, and the work presented in it, is the result of my own original research. Wherever contributions from others were involved, this has been clearly stated through references to the literature and acknowledgements of collaborative research.

Oxford, October 11th, 2019

Alessandro Alcinesio